The US/UK
World Magnetic Model
for 2025-2030

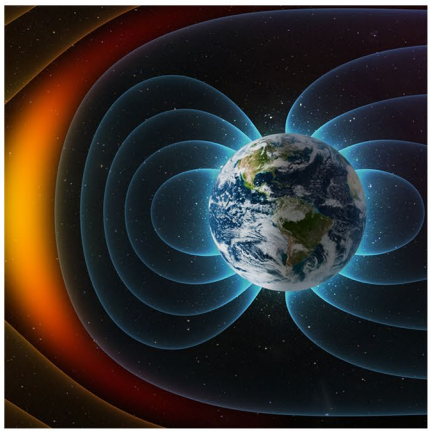

British Geological Survey

Defence Geographic Centre

Arnaud Chulliat
Manoj Nair
Li-Yin Young
Nir Boneh
Brian Meyer
Michael Paniccia (NGA)

NOAA National Centers for Environmental Information
325 Broadway
NOAA E/NE42
Boulder, CO 80305
USA

William Brown
Natalia Gómez Pérez
Callum Watson
Ciarán Beggan

British Geological Survey Geomagnetism Team
The Lyell Centre
Research Avenue South
Edinburgh, EH14 4AP
UK

Bibliographic Reference:

Chulliat, A., W. Brown, M. Nair, N. Gomez Perez, L.-Y. Young, C. Watson, N. Boneh, C. Beggan, B. Meyer and M. Paniccia, 2025. The US/UK World Magnetic Model for 2025-2030: Technical Report, National Centers for Environmental Information, NOAA. https://doi.org/10.25923/prbc-s316

Approved for public release, NGA-U-2025-01497

Abstract

This report provides a comprehensive description of the World Magnetic Model (WMM) 2025 and its higher-resolution version, the World Magnetic Model – High Resolution (WMMHR) 2025. Section 1 contains information that users of WMM2025 and WMMHR2025 require to implement the model and software in navigation and heading systems, and to understand magnetic charts, poles and geomagnetic coordinate systems. Section 2 presents a detailed summary of the data used and the modeling techniques employed. Section 3 assesses model uncertainties and describes the error models associated with WMM2025 and WMMHR2025. Section 4 provides charts of all the magnetic elements at 2025.0 and their projected annual rates of change between 2025.0 and 2030.0 based on WMM2025. These predictions are derived from the best knowledge of the geomagnetic main field evolution at the time the WMM was released.

Sponsored by the U.S. National Geospatial-Intelligence Agency (NGA) and the U.K. Defence Geographic Centre (DGC), the World Magnetic Model (WMM) and the World Magnetic Model – High Resolution (WMMHR) are produced by the U.S. National Oceanic and Atmospheric Administration's National Centers for Environmental Information (NOAA NCEI) and the British Geological Survey (BGS). The WMM is the standard model used by the U.S. Department of Defense (DoD), the U.K. Ministry of Defence, the North Atlantic Treaty Organization (NATO) and the International Hydrographic Organization (IHO), for navigation, attitude and heading referencing systems using the geomagnetic field. It is also used widely in civilian navigation and heading systems.

The WMM2025 and WMMHR2025 product release includes downloadable software tools and online calculators that enable the computation of both models and/or the integration of their subroutines into larger DoD systems. The provided software is designed to support various aspects of DoD systems procurement and development. All users are encouraged to use WMMHR in systems able to support the additional coefficients. WMMHR is expected to outperform WMM in most practical applications, and WMM should be implemented only in legacy systems unable to ingest the additional coefficients. See Section 3.3 for more details.

Contacts

The model, associated software, digital charts and documentation are available on line and by contacting NCEI, BGS, or NGA.

Please cite using these identifiers. Recommended usage and additional information available at:
Technical Report: https://doi.org/10.25923/prbc-s316
Dataset: https://doi.org/10.25921/aqfd-sd83

Model and Software Support

National Centers for Environmental Information
NOAA E/NE42
325 Broadway
Boulder, CO, 80305
U.S.

Attention: Arnaud Chulliat or Manoj Nair

Phone: (720) 457-4295 or (720) 446-9621

Email: geomag.models@noaa.gov

Web: https://www.ncei.noaa.gov/products/world-magnetic-model

British Geological Survey
The Lyell Centre
Research Avenue South
Edinburgh, EH14 4AP
U.K.

Attention: William Brown or Ciarán Beggan

Phone: (+44) 0131 667 1000

Email: geomag@bgs.ac.uk

Web: https://geomag.bgs.ac.uk/research/modelling/WorldMagneticModel.html

Applicability within the U.S. Department of Defense

National Geospatial-Intelligence Agency
Geomatics Office
NGA-SN, Mail Stop L-41
3838 Vogel Road
Arnold, MO 63010-6238
U.S.

Email: geomatics@nga.mil

Applicability within the U.K. Ministry of Defence

Defence Geographic Centre
Elmwood Avenue
Feltham
Middlesex, TW13 7AH
U.K.

Email: UKStratCom-DI-NCGI-DGC-Feedback@mod.gov.uk

The NATO and military specifications for magnetic models are STANAG 7172 (NATO Standardization Agency, 2011) and MIL-PRF-89500B (Department of Defense, 2019). Magnetic model requirements that are more stringent than those set forth in these specifications should be addressed to NCEI and BGS (e.g., those that must include magnetic effects of the Earth's crust, ionosphere, or magnetosphere and/or require greater spatial or temporal resolution on a regional or local basis).

Acknowledgements

This work was carried out under the sponsorship of the U.S. National Geospatial-Intelligence Agency (NGA) and the U.K. Ministry of Defence, Defence Geographic Centre (DGC). The maps of the geomagnetic elements were designed by Jesse Varner and Jordan Schweizer (Cooperative Institute for Research in the Environmental Sciences, CIRES, University of Colorado Boulder and NOAA/NCEI). Collin Kadlecek (CIRES and NOAA/NCEI) contributed to the calculation of high-precision test values and the determination of pole positions. Annette Balmes (CIRES and NOAA/NCEI) contributed to software testing and validation. Patrick Alken (CIRES and NOAA/NCEI) created the retrospective WMMHR models used to estimate the crustal field contribution to the model uncertainty. Thank you to Barbara Ambrose, Bridgette Haley, Jessicca Allen, and Sara Veasey on the NCEI Content Team for helping format the document, figures, and tables, and ensuring this document is accessible by people with disabilities. Thank you to Laura Ohlmann and Lauren Carroll on the NCEI Communications Team for assisting with copyediting and communications. Dr. Laurel Rachmeler (NOAA/NCEI) is the Federal manager for the WMM project, which is funded by NGA. Dr. Ross Burrows at NGA supported the WMM development and contributed to the software testing. Special thanks to Chris Vasko (Peraton), Mike Wenkel (Peraton), and Will Bossio (NGA) for their ongoing support of the WMM mission and management. Data from the Swarm satellite mission were provided by the European Space Agency (ESA), supported by ESA member states. Many institutes and agencies are involved in the operation of geomagnetic observatories around the world. In particular we would like to thank: Centre de Recherche en Astronomie, Astrophysique et Geophysique, ALGERIA; Servicio Meteorológico Nacional, ARGENTINA; Universidad Nacional de la Plata, ARGENTINA; Geoscience Australia, AUSTRALIA; Zentralanstalt fur Meteorologie und Geodynamik, AUSTRIA; Royal Meterological Institute of Belgium, BELGIUM; Observatorio Nacional, BRAZIL; Geological Survey of Canada, CANADA; China Earthquake Administration, CHINA; Chinese Academy of Sciences, Institute of Geophysics, CHINA; Department of Geophysics, Faculty of Science, University of Zagreb, CROATIA; Geophysical Institute, Academy of Sciences of the Czech Republic, CZECH REPUBLIC; DTU Space, National Space Institute, Technical University of Denmark, DENMARK; Finnish Meteorological Institute, FINLAND; Sodankyla Geophysical Observatory, University of Oulu, FINLAND; Ecole et Observatoire des Sciences de la Terre, FRANCE; Institut de Physique du Globe de Paris, FRANCE; Alfred-Wegener-Institute, Helmholtz Centre for Polar and Marine Research, GERMANY; Federal Institute for Geosciences and Natural Resources, GERMANY; GFZ Helmholtz Centre for Geosciences, GERMANY; Ludwig Maximilians University Munich, GERMANY; Universities of Karlsruhe and Stuttgart, GERMANY; Hungarian Research Network Institute of Earth Physics and Space Science, HUNGARY; Science Institute, University of Iceland, ICELAND; Indian Institute of Geomagnetism, INDIA; National Geophysical Research Institute, Council of Scientific and Industrial Research, INDIA; The Irish Meteorological Service, IRELAND; Geological Survey of Israel, ISRAEL; Istituto Nazionale di Geofisica e Vulcanologia, ITALY; Geospatial Information Authority of Japan, JAPAN; Japan Meteorological Agency, JAPAN; Nampula Geomagnetic Observatory, MOZAMBIQUE; Institute of Geological and Nuclear Sciences Limited, NEW ZEALAND; University of Tromso, The Auroral Observatory, NORWAY; Instituto Geofisico del Perú, PERU; Institute of Geophysics Polish Academy of Sciences, POLAND; Instituto Geofysico, Universidade de Coimbra, PORTUGAL; Instituto Portugues do Mar e de Atmosfera, PORTUGAL; Geological Institute of Romania, ROMANIA; Arctic and Antarctic Research Institute, RUSSIA; Russian Academy of Sciences, RUSSIA; Ministry of Natural Resources & Environment - Meteorology Division, SAMOA; Republic Geodetic Authority, SERBIA; Earth Science Institute of the Slovak Academy of Sciences, SLOVAKIA; South African National Space Agency, SOUTH AFRICA; Korean Meteorological Administration, SOUTH KOREA; Ebro Observatory, SPAIN; Instituto Geografico Nacional, SPAIN; Real Instituto y Observatorio de la Armada, SPAIN; Geological Survey of Sweden, SWEDEN; Swedish Institute of Space Physics, SWEDEN; ETH Zürich, Institut für Geophysik, SWITZERLAND; Earthquake Research Institute, TÜRKIYE; Institute of Geophysics of the National Academy of Sciences of Ukraine, UKRAINE; National Antarctic Scientific Center of Ukraine, UKRAINE; British Geological Survey, UNITED KINGDOM; Halliburton Sperry Drilling, UNITED STATES OF AMERICA; United States Geological Survey, UNITED STATES OF AMERICA; and Institute

of Geophysics of the Vietnamese Academy of Science and Technology, VIETNAM. The INTERMAGNET program and ICSU World Data System (primarily the World Data Centre for Geomagnetism, Edinburgh) assist in the quality control and dissemination of observatory data. The magnetic activity indices Kp and Dst were computed and provided by GFZ Helmholtz Centre for Geosciences (GFZ), Germany and World Data Center for Geomagnetism in Kyoto, respectively. We acknowledge use of NASA/GSFC's Space Physics Data Facility's ftp service, and OMNI data, particularly measurements from the NASA/ACE and NOAA/DSCOVR missions. This model could not have been produced without the efforts of all these institutes.

Contents

1. The Model

1.1 Introduction

The Earth is like a giant magnet. At every location on or above the Earth, its magnetic field has a generally well-defined direction, which can be used to orient ships, aircraft, satellites, antennas, drilling equipment and handheld devices. At some places on the globe the horizontal direction of the magnetic field coincides with the direction of geographic north ("true" north), but in general this is not the case. The angular amount by which the horizontal direction of the magnetic field differs from true north is called the magnetic declination, or simply declination (D, see Figure 1). This is the correction required to convert between a magnetic bearing and a true bearing. The primary function of the World Magnetic Model (WMM) is to provide magnetic declination for any specified location on Earth. In addition to the magnetic declination, the WMM also provides the complete geometry of the field from 1 km below the World Geodetic System 1984 (WGS 84) ellipsoid surface to at least 850 km above it (MIL-PRF-89500B, Department of Defense, 2019). The exact upper limit can vary because of the way solar wind affects the magnetic field in space (see Table 17). The magnetic field extends deep into the Earth and far out into space, but the WMM is not valid at these extremes.

The Earth's magnetism has several sources. All sources affect a scientific or navigational instrument but only some are represented in the WMM. The strongest contribution, by far, is the magnetic field produced by the Earth's liquid-iron outer core, called the "core field". Magnetic minerals in the crust and upper mantle make a further contribution that can be locally significant, called the "crustal field". Electric currents induced by the flow of conducting sea water through the ambient magnetic field make a further, albeit weak, contribution to the observed magnetic field. All of these are of "internal" origin and their large-scale components (see below) are included in the WMM. Deliberately excluded from the WMM by the data selection process and by other means (e.g., model co-estimation) are so-called "disturbance fields". These are contributions arising from electric currents in the upper atmosphere and near-Earth space. These "external" magnetic fields are time-varying, and have a further effect. They induce electric currents in the Earth and oceans, producing secondary internal magnetic fields, which are considered part of the disturbance field and are not represented in the WMM.

The mathematical representation of the WMM is an expansion of the magnetic potential into spherical harmonic functions up to degree and order 12. The minimum resolved wavelength is given by $360^\circ/\sqrt{12 \times 13} = 28.8^\circ$ in arc-length, which corresponds to approximately 3,200 km in longitude at the equator and in latitude globally (see section 3.6.3 of Backus et al., 1996). The WMM models the internal magnetic fields that are not part of the disturbance field and have spatial wavelengths exceeding 30° in arc-length. This encompasses nearly the entire core field and the long-wavelength components of the crustal and oceanic fields. In this report, the term "main field" refers to the portion of the Earth's magnetic field at epoch 2025.0 that is represented by the WMM.

The core magnetic field undergoes perceptible changes from year to year. This phenomenon, known as the secular variation (SV), is accounted for in the WMM by a linear SV model. Specifically, each coefficient in the spherical harmonic representation of the magnetic potential is modeled as a straight-line function of time (see Section 1.2). Due to unpredictable non-linear variations in the core field, the WMM coefficients must be updated every five years. The revision described in this report, WMM2025, is valid from 2025.0 to 2030.0.

This release introduces a new product: a higher spatial resolution version of the WMM, known as the World Magnetic Model – High Resolution (WMMHR). The WMMHR expands the spherical harmonic representation up to degree and order 133, resolving a minimum wavelength of $360^\circ/\sqrt{133 \times 134} = 2.70^\circ$ in arc-length, corresponding to approximately 300 km in longitude at the equator and in latitude globally. From degrees 1 to 15, the WMMHR is dominated by the core magnetic field. From degrees 16 to 133, it is primarily dominated by the crustal magnetic field and is derived from the MF7 model (Maus et al., 2008; https://geomag.colorado.edu/magnetic-field-model-mf7). The SV in WMMHR is truncated at a maximum degree

of 15. While the WMM only uses 336 non-zero coefficients, the WMMHR needs 18,210 non-zero coefficients. Another difference lies in the precision of the coefficients: the WMM coefficients are provided with one decimal place, while the WMMHR coefficients are provided with four decimal places to ensure sufficient accuracy.
All users are encouraged to use WMMHR in systems that can support the additional coefficients. WMMHR is expected to outperform WMM in all cases, and WMM should be implemented only in legacy systems that are unable to ingest the additional coefficients. See Section 3.3 for more details.

1.1.1 Magnetic elements

The geomagnetic field vector, $\mathbf{B}_m$, is described by seven elements. These are the northerly intensity X, the easterly intensity Y, the vertical intensity Z (positive downwards) and the following quantities derived from X, Y and Z: the horizontal intensity H, the total intensity F, the inclination angle I (also called the dip angle and measured from the horizontal plane to the field vector, positive downwards) and the declination angle D (also called the magnetic variation and measured clockwise from true north to the horizontal component of the field vector). In the descriptions of X, Y, Z, H, F, I, and D above, the vertical direction is perpendicular to the WGS 84 ellipsoid model of the Earth, the horizontal plane is perpendicular to the vertical direction and the rotational directions clockwise and counter-clockwise are determined by a view from above (see Figure 1).

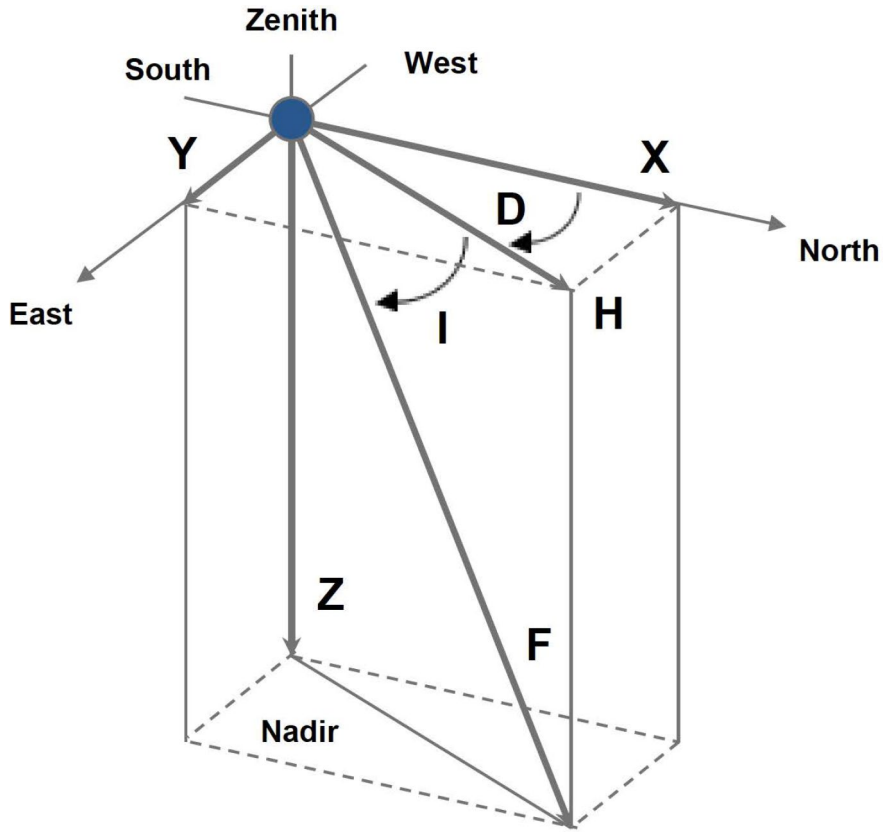

Figure 1: The seven elements of the geomagnetic field vector $\mathbf{B}_m$ associated with an arbitrary point in space.

The quantities X, Y and Z are the sizes of perpendicular vectors that add vectorially to $\mathbf{B}_m$. Conversely, X, Y and Z can be determined from the quantities F, I and D (i.e., the quantities that specify the size and direction of $\mathbf{B}_m$).

1.1.2 Grid variation

In the polar regions, or near the rotation axis of the Earth, the angle *D* changes strongly with a change in the longitude of the observer, and is therefore a poor measure of the direction of $\mathbf{B}_m$. For this reason, the WMM specification (MIL-PRF-89500B, Department of Defense, 2019) defines two auxiliary angles, called grid variation north (GV_N) and south (GV_S), for the direction of $\mathbf{B}_m$ in the horizontal plane in each polar region. Their definitions are:

$$GV_N = D - \lambda \quad \text{for} \quad \varphi > 55^\circ \tag{1}$$

$$GV_S = D + \lambda \quad \text{for} \quad \varphi < -55^\circ$$

where λ is the longitude and φ is the geodetic latitude.

The quantities GV_N and GV_S defined above are examples of a more general concept, namely grid variation (also called grid magnetic angle or grivation). At a location on the plane of a chosen horizontal grid coordinate system, grivation is the angle between grid north and magnetic north, i.e., the angle measured clockwise from the direction parallel to the grid's northing axis to the horizontal component of the magnetic field at the observer's location. Grivation is useful for local surveys, where location is given by grid coordinates rather than by longitude and latitude. It is dependent on the map projection used to define the grid coordinates. In general, it is

$$GV_{\text{grid}} = D - C \tag{2}$$

where D is the magnetic declination and C is the "convergence-of-meridians" defined as the clockwise angle from the northward meridional arc to the grid Northing direction.

For example, large scale military topographic mapping routinely employs the Universal Transverse Mercator (UTM) grid coordinates for the map projection of the sheet, for the definition of a grid to overprint, and for a grivation calculation as defined above. Above 84°N and below 80°S, it employs the Universal Polar Stereographic (UPS) grid. For these two grids, the grid variation could be notated GV_{UTM} and GV_{UPS}, respectively.

In the WMM subroutine library, both GV_{UPS} and GV_{UTM} are provided within certain restrictions (see the software user's guide).

1.1.3 Range of the magnetic elements at the Earth's surface

Table 1 shows the expected range of the magnetic field elements and GV at the Earth's surface.

Table 1: Range of magnetic elements and GV at the Earth's surface.

Element	Name	Alternative Name	Min Range	Max Range	Unit	Positive Sense
X	North component	Northerly intensity	−17000	43000	nT	North
Y	East component	Easterly intensity	−18000	17000	nT	East
Z	Down component	Vertical intensity	−67000	62000	nT	Down
H	Horizontal intensity	N/A	0	43000	nT	None
F	Total intensity	Total field	23000	67000	nT	None
I	Inclination	Dip	−90	90	Degree	Down
D	Declination	Magnetic variation	−180	180	Degree	East / Clockwise
GV	Grid variation	Grivation	−180	180	Degree	East / Clockwise

1.2 Relevant model equations

This section describes the representation of the magnetic field in the WMM and WMMHR and lists the equations needed to obtain the magnetic field elements for the desired location and time from the WMM and WMMHR coefficients. All variables in this section adhere to the following measurement conventions: angles are in radians, lengths are in meters, magnetic intensities are in nanoteslas (nT, where one tesla is one weber per square meter or one $kg.s^{-2}.A^{-1}$) and times are in years. The software may display these quantities in different units, which will be clearly indicated.

The main magnetic field $\mathbf{B}_m$ is a potential field and therefore can be written in geocentric spherical coordinates (longitude λ, latitude φ', radius r) as the negative spatial gradient of a scalar potential

$$\mathbf{B}_m(\lambda, \varphi', r, t) = -\nabla V(\lambda, \varphi', r, t) \tag{3}$$

where t is the time. This potential can be expanded in terms of spherical harmonics:

$$V(\lambda, \varphi', r, t) = a \sum_{n=1}^{N} \left(\tfrac{a}{r}\right)^{n+1} \sum_{m=0}^{n} \left(g_n^m(t)\cos(m\lambda) + h_n^m(t)\sin(m\lambda)\right) \breve{P}_n^m(\sin\varphi') \tag{4}$$

where N = 12 (respectively N = 133) is the degree of the expansion of the WMM (respectively WMMHR), a (6,371,200 m) is the geomagnetic reference radius (which is close to the mean Earth radius), (λ, φ', r) are the longitude, latitude and radius in a spherical geocentric reference frame, $g_n^m(t)$ and $h_n^m(t)$ are the time-dependent Gauss coefficients of degree n and order m describing the Earth's main magnetic field. For any real number μ, $\breve{P}_n^m(\mu)$ are the Schmidt semi-normalized associated Legendre functions defined as:

$$\begin{aligned} \breve{P}_n^m(\mu) &= \sqrt{2\tfrac{(n-m)!}{(n+m)!}} P_{n,m}(\mu) \;\text{ if }\; m > 0 \\ \breve{P}_n^m(\mu) &= \qquad\qquad P_{n,m}(\mu) \;\text{ if }\; m = 0 \end{aligned} \tag{5}$$

Here, the definition of $P_{n,m}(\mu)$ is commonly used in geodesy and geomagnetism (e.g., Heiskanen and Moritz, 1967, equation 1–60; Langel, 1987, equation 8). Sample functions, for geocentric latitude φ', are:

$$\begin{aligned} P_{3,0}(\sin\varphi') &= \tfrac{1}{2}(\sin\varphi')\left(5\sin^2\varphi' - 3\right) \\ P_{3,1}(\sin\varphi') &= -\tfrac{3}{2}(\cos\varphi')\left(1 - 5\sin^2\varphi'\right) \\ P_{3,2}(\sin\varphi') &= 15(\sin\varphi')\left(1 - \sin^2\varphi'\right) \\ P_{3,3}(\sin\varphi') &= 15\cos^3\varphi' \end{aligned} \tag{6}$$

These $P_{n,m}(\mu)$ are related to the $P_n^m(\mu)$ defined in Abramowitz and Stegun (1972, Chapter 8) or Gradshteyn and Ryzhik (1994, Chapter 8.7) by $P_{n,m}(\mu) = (-1)^m P_n^m(\mu)$.

WMM2025 (and WMMHR2025, respectively) comprises two sets of Gauss coefficients to degree and order N = 12 (and N = 133, respectively). One set provides a spherical harmonic main field model for 2025.0 in units of nT, while the other set provides a predictive secular variation model for the period 2025.0 to 2030.0 in units of nT/year. The secular variation model was derived from geomagnetic data prior to 2025.0. It represents our

best knowledge of the geomagnetic main field evolution at the time of the WMM release and is expected to yield geomagnetic main field values within defined uncertainty parameters for the lifetime of the model. The WMMHR2025 secular variation coefficients are all zero for degrees greater or equal to 16.

A step-by-step procedure is provided below for computing the magnetic field elements at a given location and time (λ, φ, h_{MSL}, t), where λ and φ are the longitude and geodetic latitude, h_{MSL} is height above Mean Sea Level (MSL), and t is the time given in decimal years.

In the first step, the user provides the time, location and height above MSL at which the magnetic elements are to be calculated. The height above MSL is then converted to height h above the WGS 84 ellipsoid by using the geopotential model EGM96 (Lemoine et al., 1998). This is accomplished by interpolating a grid of the geoid height file with a spatial resolution of 15 arc-minutes. This stage of converting height above MSL to height above the WGS 84 ellipsoid has a very small effect on the resulting magnetic field values (of the order of 1 nT or less) and is unnecessary in the majority of implementations. Note that the user can also directly enter the height above the WGS 84 ellipsoid into the software.

The geodetic coordinates (λ, φ, h) are then transformed into spherical geocentric coordinates (λ, φ', r) by recognizing that λ is the same in both coordinate systems, and that (φ', r) is computed from (φ, h) according to the equations:

$$
\begin{aligned}
p &= (R_c + h)\cos\varphi \\
z &= \left(R_c\left(1 - e^2\right) + h\right)\sin\varphi \\
r &= \sqrt{p^2 + z^2} \\
\varphi' &= \arcsin\tfrac{z}{r}
\end{aligned}
\tag{7}
$$

Here, $p = \sqrt{x^2 + y^2}$, where x, y and z are the coordinates of a geocentric Cartesian coordinate system in which the positive *x* and *z* axes point in the directions of the prime meridian (λ = 0) and the Earth's rotation axis, respectively. The semi-major axis A, reciprocal flattening $1/f$, eccentricity squared e^2 and radius of curvature of the prime vertical (also called normal section) R_c at the given latitude φ are given for the WGS 84 ellipsoid as

$$
\begin{aligned}
A &= 6378137\ \ m \\
\tfrac{1}{f} &= 298.257223563 \\
e^2 &= f(2 - f) \\
R_c &= \frac{A}{\sqrt{1 - e^2\sin^2\varphi}}
\end{aligned}
\tag{8}
$$

In the second step, the Gauss coefficients $g_n^m(t)$ and $h_n^m(t)$ are determined for the desired time t from the model coefficients $g_n^m(t_0)$, $h_n^m(t_0)$, $\dot{g}_n^m(t_0)$ and $\dot{h}_n^m\left(t_0\right)$ as

$$
\begin{aligned}
g_n^m(t) &= g_n^m(t_0) + (t - t_0)\dot{g}_n^m(t_0) \\
h_n^m(t) &= h_n^m(t_0) + (t - t_0)\dot{h}_n^m(t_0)
\end{aligned}
\tag{9}
$$

where the time is given in decimal years and t_0 = 2025.0, the reference epoch of the model. The quantities $g_n^m(t_0)$ and $h_n^m(t_0)$ are called the main field coefficients and the quantities $\dot{g}_n^m\left(t_0\right)$ and $\dot{h}_n^m\left(t_0\right)$ are called the secular variation coefficients.

In the third step, the field vector components X', Y' and Z' in geocentric coordinates are computed as

$$\begin{aligned} X'(\lambda,\varphi',r) &= -\tfrac{1}{r}\tfrac{\partial V}{\partial \varphi'} \\ &= -\sum_{n=1}^{12}\left(\tfrac{a}{r}\right)^{n+2}\sum_{m=0}^{n}\left(g_n^m(t)\cos m\lambda + h_n^m(t)\sin m\lambda\right)\tfrac{d\breve{P}_n^m(\sin\varphi')}{d\varphi'} \end{aligned} \tag{10}$$

$$\begin{aligned} Y'(\lambda,\varphi',r) &= -\tfrac{1}{r\cos\varphi'}\tfrac{\partial V}{\partial \lambda} \\ &= \tfrac{1}{\cos\varphi'}\sum_{n=1}^{12}\left(\tfrac{a}{r}\right)^{n+2}\sum_{m=0}^{n} m\left(g_n^m(t)\sin m\lambda - h_n^m(t)\cos m\lambda\right)\breve{P}_n^m(\sin\varphi') \end{aligned} \tag{11}$$

$$\begin{aligned} Z'(\lambda,\varphi',r) &= \tfrac{\partial V}{\partial r} \\ &= -\sum_{n=1}^{12}\left(n+1\right)\left(\tfrac{a}{r}\right)^{n+2}\sum_{m=0}^{n}\left(g_n^m(t)\cos m\lambda + h_n^m(t)\sin m\lambda\right)\breve{P}_n^m(\sin\varphi') \end{aligned} \tag{12}$$

At this point, the secular variation of the field components can be computed as

$$\begin{aligned} \dot{X}'(\lambda,\varphi',r) &= -\tfrac{1}{r}\tfrac{\partial \dot{V}}{\partial \varphi'} \\ &= -\sum_{n=1}^{12}\left(\tfrac{a}{r}\right)^{n+2}\sum_{m=0}^{n}\left(\dot{g}_n^m\cos m\lambda + \dot{h}_n^m\sin m\lambda\right)\tfrac{d\breve{P}_n^m(\sin\varphi')}{d\varphi'} \end{aligned} \tag{13}$$

$$\begin{aligned} \dot{Y}'(\lambda,\varphi',r) &= -\tfrac{1}{r\cos\varphi'}\tfrac{\partial \dot{V}}{\partial \lambda} \\ &= \tfrac{1}{\cos\varphi'}\sum_{n=1}^{12}\left(\tfrac{a}{r}\right)^{n+2}\sum_{m=0}^{n} m\left(\dot{g}_n^m\sin m\lambda - \dot{h}_n^m\cos m\lambda\right)\breve{P}_n^m(\sin\varphi') \end{aligned} \tag{14}$$

$$\begin{aligned} \dot{Z}'(\lambda,\varphi',r) &= \tfrac{\partial \dot{V}}{\partial r} \\ &= -\sum_{n=1}^{12}(n+1)\left(\tfrac{a}{r}\right)^{n+2}\sum_{m=0}^{n}\left(\dot{g}_n^m\cos m\lambda - \dot{h}_n^m\sin m\lambda\right)\breve{P}_n^m(\sin\varphi') \end{aligned} \tag{15}$$

$$\tfrac{d\breve{P}_n^m(\sin\varphi')}{d\varphi'} = (n+1)(\tan\varphi')\breve{P}_n^m(\sin\varphi') - \sqrt{(n+1)^2 - m^2}(\sec\varphi')\breve{P}_{n+1}^m(\sin\varphi') \tag{16}$$

In the fourth step, the geocentric magnetic field vector components $\boldsymbol{X}'$, $\boldsymbol{Y}'$ and $\boldsymbol{Z}'$, are rotated into the ellipsoidal reference frame, using

$$\begin{aligned} X &= X' \cos\left(\varphi' - \varphi\right) - Z' \sin\left(\varphi' - \varphi\right) \\ Y &= Y' \\ Z &= X' \sin\left(\varphi' - \varphi\right) + Z' \cos\left(\varphi' - \varphi\right) \end{aligned} \tag{17}$$

Similarly, the time derivatives of the vector components, $\dot{X}'$, $\dot{Y}'$ and $\dot{Z}'$ are rotated:

$$\begin{aligned} \dot{X} &= \dot{X}' \cos\left(\varphi' - \varphi\right) - \dot{Z}' \sin\left(\varphi' - \varphi\right) \\ \dot{Y} &= \dot{Y}' \\ \dot{Z} &= \dot{X}' \sin\left(\varphi' - \varphi\right) + \dot{Z}' \cos\left(\varphi' - \varphi\right) \end{aligned} \tag{18}$$

In the last step, the magnetic elements $\boldsymbol{H}$, $\boldsymbol{F}$, $\boldsymbol{I}$ and $\boldsymbol{D}$ are computed from the orthogonal components:

$$H = \sqrt{X^2 + Y^2},\ F = \sqrt{H^2 + Z^2},\ I = \arctan\left(Z,H\right),\ D = \arctan\left(Y,X\right) \tag{19}$$

where $\arctan\left(a,b\right)$ is $\tan^{-1}\left(a/b\right)$, taking into account the angular quadrant, avoiding a division by zero, and resulting in a declination in the range of $-\pi$ to π and an inclination in the range of $-\pi/2$ to $\pi/2$. These angles in radians are then output by the WMM software in degrees.

The secular variation of these elements is computed using

$$\begin{aligned} \dot{H} &= \frac{X \times \dot{X} + Y \times \dot{Y}}{H} \\ \dot{F} &= \frac{X \times \dot{X} + Y \times \dot{Y} + Z \times \dot{Z}}{F} \\ \dot{I} &= \frac{H \times \dot{Z} - Z \times \dot{H}}{F^2} \\ \dot{D} &= \frac{X \times \dot{Y} - Y \times \dot{X}}{H^2} \\ G\dot{V} &= \dot{D} \end{aligned} \tag{20}$$

where $\dot{I}$, $\dot{D}$ and $G\dot{V}$ are given in radians per year. The WMM software then outputs these angles in arc-minutes per year or decimal degrees per year.

1.3 The WMM2025 coefficients

The model coefficients, also referred to as Gauss coefficients, are listed in Table 2. These coefficients can be used to compute values for the field elements and their annual rates of change at any location near the Earth's surface, and at any date between 2025.0 and 2030.0. (The WMMHR2025 coefficients are not reproduced in this report due to the large number of coefficients.)

Table 2: Final coefficients for WMM2025. Units are nT for the main field, and nT per year for the secular variation. The index n is the degree and m is the order. Since $h_n^m(t_0)$ and $\dot{h}_n^m(t_0)$ are not defined for m = 0, the corresponding fields are left blank. (The corresponding coefficients are set to zero in the WMM2025 coefficient file.)

n	m	$g_n^m(t_0)$	$h_n^m(t_0)$	$\dot{g}_n^m(t_0)$	$\dot{h}_n^m(t_0)$
1	0	−29351.8		12	
1	1	−1410.8	4545.4	9.7	−21.5
2	0	−2556.6		−11.6	
2	1	2951.1	−3133.6	−5.2	−27.7
2	2	1649.3	−815.1	−8	−12.1
3	0	1361		−1.3	
3	1	−2404.1	−56.6	−4.2	4
3	2	1243.8	237.5	0.4	−0.3
3	3	453.6	−549.5	−15.6	−4.1
4	0	895		−1.6	
4	1	799.5	278.6	−2.4	−1.1
4	2	55.7	−133.9	−6	4.1
4	3	−281.1	212	5.6	1.6
4	4	12.1	−375.6	−7	−4.4
5	0	−233.2		0.6	
5	1	368.9	45.4	1.4	−0.5
5	2	187.2	220.2	0	2.2
5	3	−138.7	−122.9	0.6	0.4
5	4	−142	43	2.2	1.7
5	5	20.9	106.1	0.9	1.9
6	0	64.4		−0.2	
6	1	63.8	−18.4	−0.4	0.3
6	2	76.9	16.8	0.9	−1.6
6	3	−115.7	48.8	1.2	−0.4
6	4	−40.9	−59.8	−0.9	0.9
6	5	14.9	10.9	0.3	0.7
6	6	−60.7	72.7	0.9	0.9
7	0	79.5		0	
7	1	−77	−48.9	−0.1	0.6
7	2	−8.8	−14.4	−0.1	0.5
7	3	59.3	−1	0.5	−0.8
7	4	15.8	23.4	−0.1	0
7	5	2.5	−7.4	−0.8	−1
7	6	−11.1	−25.1	−0.8	0.6
7	7	14.2	−2.3	0.8	−0.2
8	0	23.2		−0.1	
8	1	10.8	7.1	0.2	−0.2
8	2	−17.5	−12.6	0	0.5
8	3	2	11.4	0.5	−0.4
8	4	−21.7	−9.7	−0.1	0.4
8	5	16.9	12.7	0.3	−0.5
8	6	15	0.7	0.2	−0.6
8	7	−16.8	−5.2	0	0.3
8	8	0.9	3.9	0.2	0.2
9	0	4.6		0	
9	1	7.8	−24.8	−0.1	−0.3
9	2	3	12.2	0.1	0.3
9	3	−0.2	8.3	0.3	−0.3
9	4	−2.5	−3.3	−0.3	0.3
9	5	−13.1	−5.2	0	0.2
9	6	2.4	7.2	0.3	−0.1
9	7	8.6	−0.6	−0.1	−0.2
9	8	−8.7	0.8	0.1	0.4
9	9	−12.9	10	−0.1	0.1
10	0	−1.3		0.1	
10	1	−6.4	3.3	0	0
10	2	0.2	0	0.1	0
10	3	2	2.4	0.1	−0.2
10	4	−1	5.3	0	0.1
10	5	−0.6	−9.1	−0.3	−0.1
10	6	−0.9	0.4	0	0.1
10	7	1.5	−4.2	−0.1	0
10	8	0.9	−3.8	−0.1	−0.1
10	9	−2.7	0.9	0	0.2
10	10	−3.9	−9.1	0	0
11	0	2.9		0	
11	1	−1.5	0	0	0
11	2	−2.5	2.9	0	0.1
11	3	2.4	−0.6	0	0
11	4	−0.6	0.2	0	0.1
11	5	−0.1	0.5	−0.1	0
11	6	−0.6	−0.3	0	0
11	7	−0.1	−1.2	0	0.1
11	8	1.1	−1.7	−0.1	0
11	9	−1	−2.9	−0.1	0
11	10	−0.2	−1.8	−0.1	0
11	11	2.6	−2.3	−0.1	0
12	0	−2		0	
12	1	−0.2	−1.3	0	0
12	2	0.3	0.7	0	0
12	3	1.2	1	0	−0.1
12	4	−1.3	−1.4	0	0.1
12	5	0.6	0	0	0
12	6	0.6	0.6	0.1	0
12	7	0.5	−0.1	0	0
12	8	−0.1	0.8	0	0
12	9	−0.4	0.1	0	0
12	10	−0.2	−1	−0.1	0
12	11	−1.3	0.1	0	0
12	12	−0.7	0.2	−0.1	−0.1

1.4 Singularities at the geographic poles

The World Magnetic Model has singularities at the North and South geographic poles. This is a mathematical issue, not a geophysical phenomenon, stemming from the ambiguity of longitude at a Pole and at any altitude over a Pole. Related to this, the North-East-Down (NED) frame of unit vectors to which the X', Y', Z' quantities are referred is defined everywhere except at or over a Pole. This section extends these concepts. The North Pole is discussed in the following, with similar implications for the South Pole.

To most comprehensively appreciate the model equations, let the arbitrariness of the North Pole's longitude disambiguate the North Pole's NED frame. In other words, if the Pole is assigned a longitude of λ, then the NED frame at the Pole is to be oriented so that the unit vector "N" of NED has the same direction as for a point approaching the pole along the λ-*meridian*, the unit vector "D" is directed downward, and the unit vector "E" is directed so that NED is right-handed. This is equivalent to requiring the NED frame at longitude λ and latitude 90° to be the limit of NED frames as the latitude approaches 90° and the longitude and altitude remain fixed.

On January 1, 2025, directly above the North (resp. South) Pole at 6,371,200 meters from the Earth's center, the magnetic field vector predicted by the WMM lies in the half-plane of the 166.27°W (resp. 31.62°W) meridian. The magnetic field vector predicted by the WMMHR lies in the half-plane of the 165.98°W (resp. 31.47°W) meridian. If the Pole is assigned λ = 0°, the components X', Y', Z' (also the components X, Y, Z) predicted by the WMM are 1709.5 nT, 417.8 nT, and 56517.5 nT respectively at the North Pole, 14185.8 nT, −8732.7 nT, and −51366.5 nT respectively at the South Pole. The components X', Y', Z' predicted by the WMMHR are 1702.7 nT, 425.2 nT, and 56441.4 nT respectively at the North Pole, 14243.1 nT, −8718.6 nT, and −51359.1 nT respectively at the South Pole. A change in the longitude assigned to the Pole is equivalent to a rotation of the NED frame about the polar axis.

The model equations of Section 1.2 support the above pole calculation and others like it provided the equation for Y' is extended by continuity as follows to ameliorate the factor $\cos(\varphi')$ in the denominator. As φ' approaches 90°, the function $\left(\check{P}_n^m(\sin\varphi')\right)/\cos\varphi'$ approaches zero if $m > 1$. It approaches certain non-zero finite limits if $m = 1$. It multiplies a zero coefficient and can be ignored if $m = 0$. For $m = 1$ and $1 \le n \le 12$ respectively, the limits are:

1	2	3	4	5	6	7	8	9	10	11	12
1	$\sqrt{3}$	$\sqrt{6}$	$\sqrt{10}$	$\sqrt{15}$	$\sqrt{21}$	$2\sqrt{7}$	6	$3\sqrt{5}$	$\sqrt{55}$	$\sqrt{66}$	$\sqrt{78}$

1.5 Model equations numerical example

A software implementation of the relevant model equations is provided with this report. Most software developers should find the C programs and/or C subroutines to be sufficient for their purposes, after adaptations are made to their own software structures.

To assist software developers who need to re-implement the model equations for special requirements, Tables 3a to 3e provide a numerical example showing the intermediate calculations of Section 1.2 for both WMM2025 and WMMHR2025. To facilitate verification of the correct implementation of the equations, the tables display more digits than are warranted by the accuracy of both models.

The output in Table 3c includes grivation calculations for four grid systems, whether or not the grid system is commonly used in that part of the world. This is helpful for the purposes of verifying correct implementation of the mathematics in the software, and if not used the unwanted grid systems may be ignored.

Table 3a: High-precision numerical example. Given values for time, altitude, latitude and longitude.

Time	2027.5000 0000	yr
Height-above-Ellipsoid	100.0000 0000	km
Latitude	−80.0000 0000	deg
Longitude	240.0000 0000	deg

Table 3b: High-precision numerical example. Computations of the magnetic field elements for WMM2025.

Row	Physical Quantity	Numerical Value	Unit
1	lambda	4.18879 02048	rad
2	phi	−1.39626 34016	rad
3	h	1 00000.00000 00000	m
4	t	2027.50000 00000	yr
5	phi−prime	−1.39512 89589	rad
6	r	64 57402.34844 73705	m
7	g(1,0,t)	−29321.80000 00000	nT
8	g(1,1,t)	−1386.55000 00000	nT
9	g(2,0,t)	−2585.60000 00000	nT
10	g(2,1,t)	2938.10000 00000	nT
11	g(2,2,t)	1629.30000 00000	nT
12	h(1,0,t)	0.00000 00000	nT
13	h(1,1,t)	4491.65000 00000	nT
14	h(2,0,t)	0.00000 00000	nT
15	h(2,1,t)	−3202.85000 00000	nT
16	h(2,2,t)	−845.35000 00000	nT
17	Xprime	5928.02413 92588	nT
18	Yprime	14760.13597 57868	nT
19	Zprime	−49324.42735 70284	nT
20	Xprime-dot	30.65654 57063	nT/yr
21	Yprime-dot	−8.04942 28995	nT/yr
22	Zprime-dot	89.18268 62382	nT/yr
23	X	5983.97604 96518	nT
24	Y	14760.13597 57868	nT
25	Z	−49317.67061 54255	nT
26	Xdot	30.55535 33530	nT/yr
27	Ydot	−8.04942 28995	nT/yr
28	Zdot	89.21740 69382	nT/yr
29	F	51825.69071 72314	nT
30	H	15927.00798 60130	nT
31	D	1.18563 08407	rad
32	I	−1.25842 21541	rad
33	Fdot	−83.66435 06802	nT/yr
34	Hdot	4.02033 61601	nT/yr
35	Ddot	−0.00196 77910	rad/yr
36	Idot	0.00060 28663	rad/yr

Table 3c: High-precision numerical example. Computations of the magnetic field elements for WMMHR2025.

Row	Physical Quantity	Numerical Value	Unit
1	lambda	4.18879 02048	rad
2	phi	−1.39626 34016	rad
3	h	1 00000.00000 00000	m
4	t	2027.50000 00000	yr
5	phi-prime	−1.39512 89589	rad
6	r	64 57402.34844 73705	m
7	g(1,0,t)	−29321.90235 00000	nT
8	g(1,1,t)	−1386.40040 00000	nT
9	g(2,0,t)	−2585.70880 00000	nT
10	g(2,1,t)	2938.07185 00000	nT
11	g(2,2,t)	1629.23580 00000	nT
12	h(1,0,t)	0.00000 00000	nT
13	h(1,1,t)	4491.66015 00000	nT
14	h(2,0,t)	0.00000 00000	nT
15	h(2,1,t)	−3202.91275 00000	nT
16	h(2,2,t)	−845.29965 00000	nT
17	Xprime	5935.64802 94825	nT
18	Yprime	14743.28736 76966	nT
19	Zprime	−49366.43274 17512	nT
20	Xprime-dot	30.34385 65209	nT/yr
21	Yprime-dot	−7.67906 61880	nT/yr
22	Zprime-dot	88.20089 01063	nT/yr
23	X	5991.64758 76618	nT
24	Y	14743.28736 76966	nT
25	Z	−49359.66732 42538	nT
26	Xdot	30.24377 81600	nT/yr
27	Ydot	−7.67906 61880	nT/yr
28	Zdot	88.23525 67101	nT/yr
29	F	51861.75008 21388	nT
30	H	15914.28173 75217	nT
31	D	1.18478 63334	rad
32	I	−1.25890 45281	rad
33	Fdot	−82.66723 60605	nT/yr
34	Hdot	4.27260 13056	nT/yr
35	Ddot	−0.00194 22510	rad/yr
36	Idot	0.00060 04871	rad/yr

Table 3d: High-precision numerical example. Grivation calculations for WMM2025. Angles are in degrees.

Grid System — Grid Zone	UPS — North	UPS — South	UTM — 10	UTM — 11
TrueN-to-GridN	240.00000 00000	−240.00000 00000	−2.95450 46801	2.95450 46801
GridN-to-MagN	−172.06835 67684	307.93164 32316	70.88614 79117	64.97713 85515
TrueN-to-MagN	67.93164 32316	67.93164 32316	67.93164 32316	67.93164 32316

Table 3e: High-precision numerical example. Grivation calculations for WMMHR2025. Angles are in degrees.

Grid System — Grid Zone	UPS — North	UPS — South	UTM — 10	UTM — 11
TrueN-to-GridN	240.00000 00000	−240.00000 00000	−2.95450 46801	2.95450 46801
GridN-to-MagN	−172.11674 34715	307.88325 65285	70.83776 12086	64.92875 18484
TrueN-to-MagN	67.88325 65285	67.88325 65285	67.88325 65285	67.88325 65285

1.6 Magnetic poles and geomagnetic coordinate systems

There are different ways of defining magnetic poles. The most common understanding is that they are the positions on the Earth's surface where the geomagnetic field is perpendicular to the ellipsoid, that is, vertical (assuming the deflection of the vertical is negligible). These positions are called ***dip poles***, and the north and south dip poles do not have to be (and are not now) antipodal. In principle the dip poles can be found by experiment, conducting a magnetic survey to determine where the field is vertical (Newitt et al., 2009). In practice the geomagnetic field is vertical on oval-shaped loci traced on a daily basis, with considerable variation from one day to the next.

Other magnetic pole definitions originate from models of the geomagnetic field (Table 4). The WMM representation of the field includes a magnetic dipole at the center of the Earth. This dipole defines an axis that intersects the Earth's surface at two antipodal points, known as the ***geomagnetic poles***. The geomagnetic poles, also called the dipole poles, can be computed from the first three Gauss coefficients of the WMM. Based on the WMM2025 coefficients for 2025.0 the geomagnetic north pole is at 72.76°W longitude and 80.79°N geocentric latitude (80.85°N geodetic latitude), and the geomagnetic south pole is at 107.24°E longitude and 80.79°S geocentric latitude (80.85°S geodetic latitude). The axis of the dipole is currently inclined at 9.21° to the Earth's rotation axis. The same dipole is the basis for the simple geomagnetic coordinate system of geomagnetic latitude and longitude (see Section 4, Geomagnetic longitude and latitude in Mercator projection). The geomagnetic equator is at geomagnetic latitude 0°. Note that the first three Gauss coefficients of the WMMHR are the same as those of the WMM, with more significant digits (see Section 2); as a result, the geomagnetic poles inferred from WMMHR2025 and WMM2025 at 2025.0 are the same to the level of precision provided above.

The WMM and WMMHR can also be used to calculate dip pole positions. These ***model dip poles*** are computed from all the Gauss coefficients using an iterative method. In 2025.0 the north dip pole computed from WMM2025 is located at longitude 139.30°E and geodetic latitude 85.76°N and the south dip pole at longitude 135.08°E and geodetic latitude 63.85°S. The north dip pole from WMMHR2025 (truncated at degree N = 15, i.e.,

representing, the core field only, see Section 2) is located at longitude 139.38°E and geodetic latitude 85.77°N and the south dip pole at longitude 135.07°E and geodetic latitude 63.86°S. Past, current, and future dip pole positions are available on NCEI's Wandering of The Geomagnetic Poles and BGS's Magnetic Poles webpages. Over the next five years, the WMM2025 predicts a very slow drift of the south dip pole, at about 9 km/year on average, and a faster (yet gradually decelerating) drift of the north dip pole, at about 35 km/year.

Scientists, map makers and polar explorers have an interest in the dip and geomagnetic pole locations. Although geomagnetic pole observations cannot be made to indicate their positions, these poles are arguably of greater significance than the dip poles. Auroral ovals, which are approximately 5° latitude bands where aurorae are likely to be seen, are approximately centered on the geomagnetic poles. They are usually displaced slightly to the night-side of the geomagnetic poles and greatly vary in size: bands of greatest activity occur between 15° and 25° from the geomagnetic poles.

A further concept is that of *eccentric dipole*, or off-centered dipole. The location of the center of the eccentric dipole (sometimes known as magnetic center), computed using the first eight Gauss coefficients of WMM2025 for 2025.0 (Langel, 1987, p. 386), is at (r, φ', λ) = (605 kilometers, 22.76°N, 135.34°E). The axis of the eccentric dipole is parallel to the axis of the (centered) dipole field. The first eight Gauss coefficients of the WMMHR are identical to those of the WMM, with more significant digits (see Section 2); as a result, the location of the eccentric dipole from WMMHR2025 is the same to the level of precision provided above.

Table 4: Computed pole positions based on WMM2025 and WMMHR2025 (truncated at degree N = 15).

Poles	Date	North	South
Geomagnetic Poles, WMM2025 & WMMHR2025	2025.0	72.76° W 80.79° N (geocentric) 80.85° N (geodetic)	107.24° E 80.79° S (geocentric) 80.85° S (geodetic)
Model Dip Poles, WMM2025	2025.0	139.29° E 85.76° N (geodetic)	135.08° E 63.85° S (geodetic)
Model Dip Poles, WMMHR2025 (N = 15)	2025.0	139.38° E 85.77° N (geodetic)	135.07° E 63.86° S (geodetic)

1.7 South Atlantic Anomaly

The South Atlantic Anomaly (SAA) represents a significant weakness in Earth's magnetic field, where the field strength drops to less than 60% of average magnetic field strength over a large region centered primarily over the South Atlantic Ocean and South America. This phenomenon leads to an increased flux of energetic particles at lower altitudes, posing potential risks to satellites traversing the region. Using WMM2025, we analyze the progression of the South Atlantic Anomaly (SAA) from 2025 and 2030, contextualized by recent trends observed from Swarm Geomagnetic Virtual Observatory (GVO; Hammer et al., 2021) data between 2019 and 2024 (Figure 2). The GVO data (indicated by white lines centered on red grid points in Figure 2) reveal the trends of the change in the total magnetic field intensity (F), with the most pronounced decrease occurring near the Caribbean region, amounting to approximately 406 nT over the five-year period. The GVO trends show that the decrease in F is most pronounced in the NW and SW edges of the SAA.

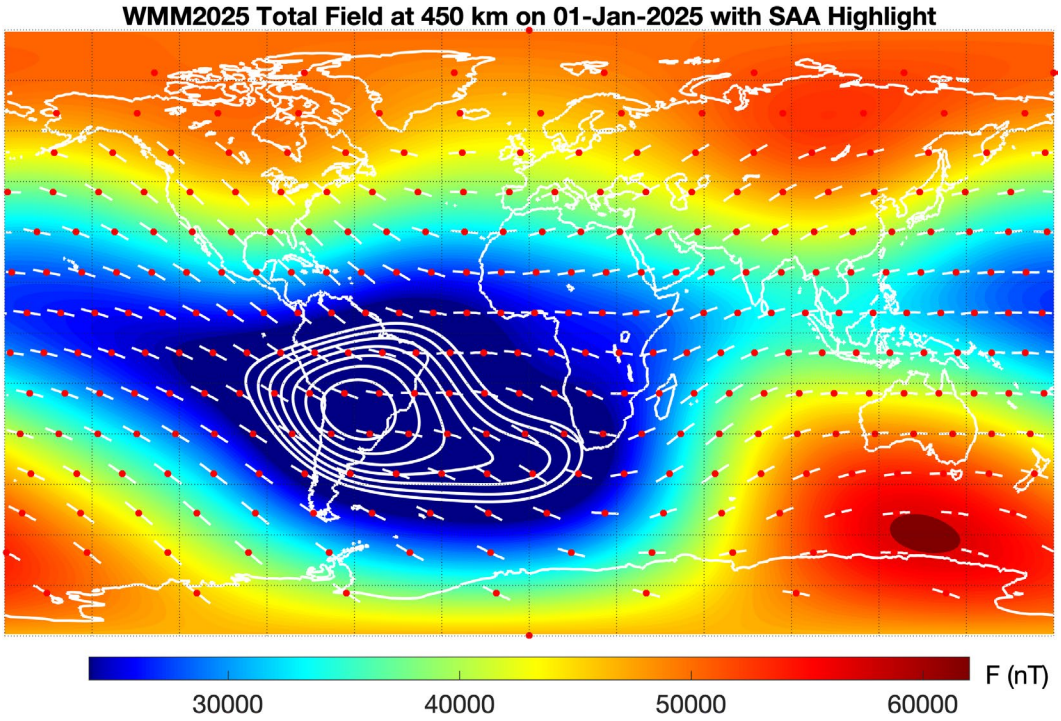

Figure 2: WMM2025 prediction of total magnetic field intensity (F) at 450 km altitude for January 1, 2025. Recent trends (2019-2024) derived from Swarm Geomagnetic Virtual Observatory (GVO) data are overlaid (white vectors indicate change over time at specific grid locations). The South Atlantic Anomaly (SAA) region is highlighted with white contours ranging from 19100 nT to 22100 nT in 500 nT increments.

The WMM predictions for F at a representative low-Earth orbit altitude of 450 km indicate a continued evolution of the SAA. Specifically, the model predicts an intensification of the anomaly between 2025 and 2030 (Figure 3), characterized by a decrease in the minimum F value within the SAA anomaly region. This intensification is visualized through highlighted SAA contours ranging from 18600 nT to 22100 nT in 500 nT increments (white). While the 2025 map displays contours starting from 19100 nT, indicating a minimum F above 18600 nT, the 2030 prediction shows the appearance of the 18600 nT contour, indicating the deepening of the anomaly. When mapped at Earth's surface, the appearance of a second, local, minimum at the eastern end of the SAA has been observed developing in recent years (Rother et al., 2021). This possible development of a two-lobed structure is attributed to two patches of reversed flux that can be observed at the core-mantle boundary, the western-most contributing to the SAA minimum over South America, and the eastern-most with a more strongly negative flux located SW of South Africa. Furthermore, a comparison of the contour shapes between 2025 (Figure 2) and 2030 (Figure 3) suggests a spatial broadening of the SAA, particularly evident in the eastward expansion of the lower intensity contours, alongside some westward expansion. This combination of intensification and spatial drift highlights the complex evolution of the SAA as projected by the WMM. If the current trends hold true, the SAA is expected to further widen and deepen in the next decade.

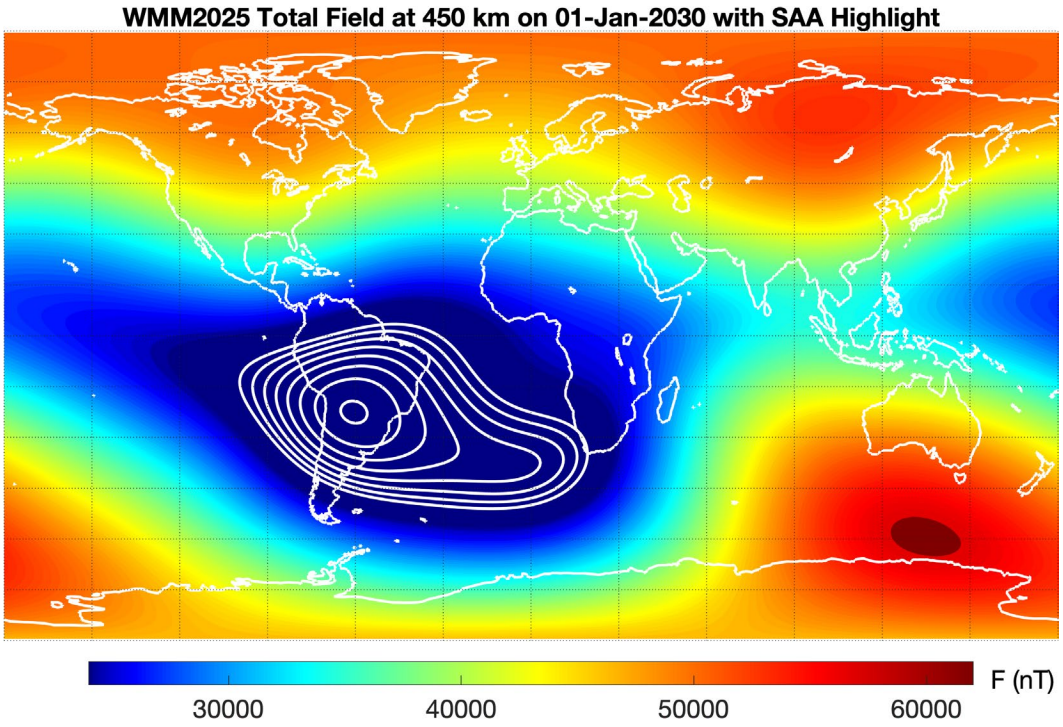

Figure 3: WM2025 prediction of total magnetic field intensity (F) at 450 km altitude for January 1, 2030. The South Atlantic Anomaly (SAA) region is highlighted with white contours ranging from 18600 nT to 22100 nT in 500 nT increments, illustrating the predicted intensification (appearance of the 18600 nT contour) and broadening of the anomaly compared to 2025.

1.8 Blackout Zones

Both WMM2025 and WMMHR2025 come with "Blackout Zones" (BoZs) at the magnetic poles. BoZs were first introduced with WMM2020 to provide better guidance to navigators and users. These zones are generated for both the north and south magnetic poles to help delineate areas where compass readings become unreliable. Within a Blackout Zone, WMM declination values are inaccurate, and compasses cannot be trusted. Surrounding each BoZ, Caution Zones serve as warnings for navigators, indicating regions where compass accuracy becomes increasingly unreliable (see Figure 4). The requirements for BoZs are described in MIL-PRF-89500B (Department of Defense, 2019).

Previously, the United States Department of Defense (DoD) Safety of Navigation (SoN) guidance included the following warning on all polar maps and charts (Defense Mapping Agency, 1981):

> "The compass becomes increasingly unreliable approaching the magnetic pole from a distance of approximately 1000 miles".

Because the magnetic poles shift significantly over time, and paper products may not always be updated to reflect these changes, this warning was stamped on all maps and charts covering areas within 1000 miles of the geographic poles (see Legacy Zones in Figure 4). With the prevalence of easily updatable digital maps, the DoD introduced BoZs as part of its modernized polar SoN guidance.

Compass needles align with the horizontal magnetic field lines allowing users to see where magnetic north is from their current location. Over most of the globe, the magnetic field lines are near parallel to the Earth's surface. However, at the magnetic poles the magnetic field lines are vertical, which is why a compass will not work well. The needle in the compass will want to point vertically and the result is a spinning needle. The BoZs are calculated to cover regions of the Earth where the horizontal component of the magnetic field is significantly weaker than the vertical component of the magnetic field.

Specifically, the BoZs are defined as constantly moving regions of the WGS 84 ellipsoid where the horizontal intensity (H) is less than 2000 nT. Each BoZ is surrounded by a Caution Zone where the horizontal intensity is less than 6000 nT. The BoZ regions are provided to users in the form of shapefiles available, and are plotted on some maps for visualization purposes (see Section 1.10). In addition, both NGA products and the online calculators provided by NCEI include warnings to navigators approaching the BoZs.

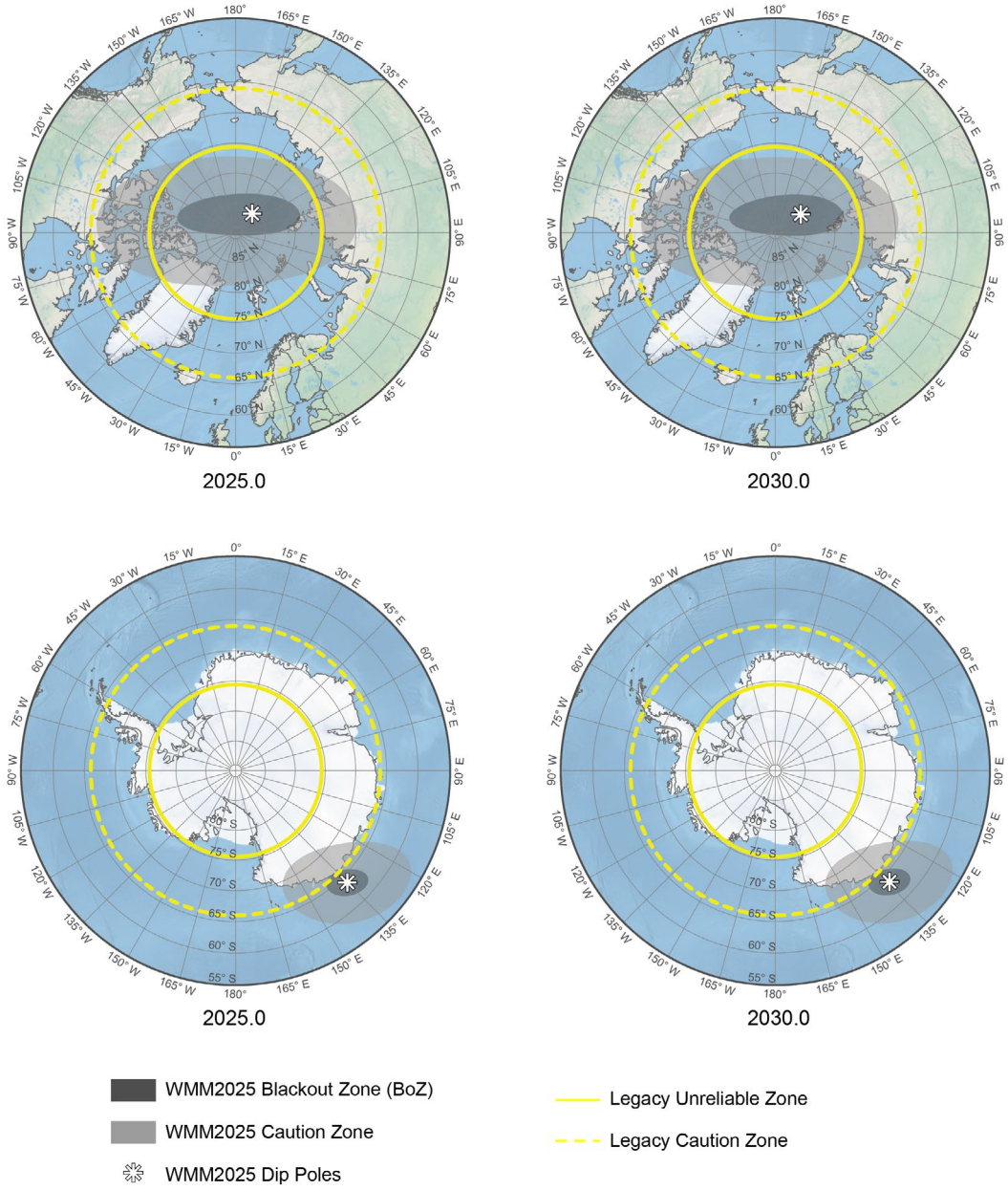

Figure 4: BoZ refinement against legacy warning zones. BoZ and Caution Zone shown at epochs 2025.0 and 2030.0 in the Northern (top) and Southern (bottom) Hemispheres.

NCEI Warnings: "Warning: location is in the blackout zone around the magnetic pole as defined by the WMM military specification (https://www.ngdc.noaa.gov/geomag/WMM/data/MIL-PRF-89500B.pdf). Compass accuracy is highly degraded in this region." [triggered if H < 2000 nT]

"Caution: location is approaching the blackout zone around the magnetic pole as defined by the WMM military specification. Compass accuracy may be degraded in this region." (triggered if H ≥ 2000 nT and H < 6000 nT)

NGA Warning: "This location is, either approaching or within the magnetic blackout zone defined by the World Magnetic Model (WMM) military specification, MIL-PRF-89500B. Compass accuracy is increasingly unreliable approaching the blackout zone where declination errors exceed 1 degree; and highly degraded within the blackout zone where declination errors of up to 180 degrees will occur. The large declination errors are a result of weak horizontal magnetic intensity and proximity of the magnetic pole."

There are two important considerations regarding the BoZs that must be understood before their implementation in navigation systems. First, BoZs move over time with the magnetic poles. WMM2025 provides BoZ locations until December 2029, and it is the user's responsibility to ensure they are using the correct BoZ for the current time. The second important consideration is that BoZs indicate regions where compass reliability becomes increasingly worse, not strict boundaries where a compass suddenly becomes unusable. A compass will not function perfectly one meter outside the BoZ and then completely fail one meter inside. The Caution Zone serves as a buffer, helping navigators anticipate increasing compass unreliability.

Figure 4 and Table 5 show the refinement of the BoZs compared against legacy paper map guidance. For the Arctic Region, the area of unreliability is reduced by over 6 million square kilometers and the area of caution is reduced by over 14 million square kilometers. The Antarctic Region reduces the area of unreliability and area of caution significantly more, and more appropriately portrays the warning zone near the magnetic pole not the geographic pole.

Table 5: BoZ size reduction against legacy warning zones. All surface areas in square kilometers on the WGS 84 ellipsoid. WMM2025 values calculated at epoch 2025.0.

Zone	Arctic	Antarctic
Legacy Unreliable Zone	8,093,922	8,093,922
WMM2025 BoZ (Unreliable Zone)	1,438,240	278,457
Difference	6,655,682	7,815,465
Legacy Caution Zone	22,221,903	22,221,903
WMM2025 Caution Zone	7,880,917	2,299,258
Difference	14,340,986	19,922,645

1.9 Supersession of the models

WMM2025 and WMMHR2025 supersede WMM2020 (Chulliat et al., 2020) and should replace it in navigation and other systems. Also included with the models is software for computing the magnetic field components X, Y, Z, H, F, I, D and auxiliary angles GV_N and GV_S as defined above, as well as the blackout zone products and the model uncertainty on each component (see Section 3). WMM2025 and WMMHR2025 are to be used from January 1, 2025 to December 31, 2029. In December 2029, barring unforeseen circumstances, the U.S. and U.K. agencies will replace WMM2025 and WMMHR2025 with new degree and order 12 (WMM) and 133 (WMMHR) main field models, and new degree and order 12 (WMM) and 15 (WMMHR) predictive secular-variation models.

1.10 Policy on alternate software for the U.S. Department of Defense

The WMM2025 product release includes several software items by which the WMM2025 and WMMHR2025 models may be computed and/or their subroutines incorporated into larger U.S. Department of Defense (DoD) systems. It is hoped that the software provided is useful for most occasions of DoD systems procurement and development.

If there are special requirements, and the model equations must be implemented anew or a separate interpolation algorithm invented, the software developer may use the label WMM2025 (or WMMHR2025) for the resulting product provided the resulting software agrees with the relevant model equations within the following tolerances:

Between latitudes 89.992°S and 89.992°N,

Quantities in nanotesla (nT) shall be correct to within 0.1 nT

Quantities in nanotesla (nT) per year shall be correct to within 0.1 nT/year

(see Section 1.4 for the computation problems exactly at the Poles).

This policy is designed to promote interoperability and to track departures from consistency when necessary. It permits systems developers to display as many digits as needed and not display unneeded digits. It also allows that the computations be taken to less than full double precision accuracy and the software retains the WMM2025 (or WMMHR2025) label. This policy refers to the allowed computational error in the software, not to the accuracy or limitations of the science or the geomagnetic model.

If there are special requirements, and the model equations are implemented anew or separate interpolation algorithm invented, and accuracy is sacrificed for speed of computation such that the above tolerances are not met, the label WMM2025 (or WMMHR2025) may not be applied to the resulting product. In this situation, the DoD entity or contractor is urged to apply to NGA or NCEI acting on behalf of NGA, for the label to adopt to indicate that this is a modification of WMM2025 (or WMMHR2025).

1.11 Description of charts

Charts of magnetic elements and their annual rates of change, and of grid variation, are available from the NOAA WMM website. Some charts are replicated in Section 4. They are also available at the BGS WMM website.

The following charts are available:

- Main field magnetic elements X, Y, Z, H, F, I and D on the Miller projection between geodetic latitudes 90°S and 90°N.
- Main field magnetic elements X, Y, Z, H, F, I and D on the north and south polar stereographic projection for geodetic latitudes northward of 55°N and southward of 55°S.
- Secular variation of X, Y, Z, H, F, I and D on the Miller projection between geodetic latitudes 90°S and 90°N.
- Secular variation of X, Y, Z, H, F, I and D on the north and south polar stereographic projection for geodetic latitudes northward of 55°N and southward of 55°S.
- Grid variation (GV) on the north and south polar stereographic projection for geodetic latitudes northward of 55°N and southward of 55°S.
- Geomagnetic latitude and longitude on the Miller projection between geodetic latitudes 90°S and 90°N.

Each chart comes in two versions: with the blackout zone and without the blackout zone.

1.12 Software online calculators and test values

The WMM and WMMHR coefficient files, software that computes WMM and WMMHR values, and several derived products are distributed by NOAA/NCEI and BGS both online and offline on behalf of NGA and DGC. They are available at:

- https://www.ncei.noaa.gov/products/world-magnetic-model
- https://www.ncei.noaa.gov/products/world-magnetic-model-high-resolution

WMM and WMMHR online calculators allow users to compute values of the magnetic field at any point within the spatial domain of validity of the model, and at any time between the model release and 2030.0. Various input and output formats are available, as well as web-based application programming interfaces (API). The calculators are available at:

- https://www.ngdc.noaa.gov/geomag/calculators/magcalc.shtml
- https://geomag.bgs.ac.uk/data_service/models_compass/wmm_calc.html

To verify the correctness of a coefficient update or new software installation, Tables 6 and 7 provide test values to validate software output.

Table 6: WMM2025 test values. The computation was carried out with double precision arithmetic. Single precision arithmetic can cause differences of up to 0.1 nT. Heights are with respect to the WGS 84 Ellipsoid. Grid Variation is with respect to the Grid North of the Universal Polar Stereographic projection.

Date	Height (km)	Lat (deg)	Lon (deg)	X (nT)	Y (nT)	Z (nT)	H (nT)	F (nT)	I (deg)	D (deg)	GV (deg)
2025.0	0	80	0	6521.6	145.9	54791.5	6523.2	55178.5	83.21	1.28	1.28
2025.0	0	0	120	39677.8	−109.6	−10580.2	39677.9	41064.3	−14.93	−0.16	
2025.0	0	−80	240	6117.5	15751.9	−52022.5	16898.1	54698.2	−72.00	68.78	−51.22
2025.0	100	80	0	6216.0	92.4	52598.8	6216.7	52964.9	83.26	0.85	0.85
2025.0	100	0	120	37688.6	−96.2	−10152.1	37688.7	39032.1	−15.08	−0.15	
2025.0	100	−80	240	5907.6	14780.3	−49540.7	15917.1	52035.0	−72.19	68.21	−51.79
2027.5	0	80	0	6500.8	294.5	54869.4	6507.5	55253.9	83.24	2.59	2.59
2027.5	0	0	120	39701.6	−167.4	−10381.8	39702.0	41036.9	−14.65	−0.24	
2027.5	0	−80	240	6200.7	15730.3	−51783.7	16908.3	54474.2	−71.92	68.49	−51.51
2027.5	100	80	0	6196.7	233.8	52670.5	6201.1	53034.3	83.29	2.16	2.16
2027.5	100	0	120	37711.5	−148.7	−9969.8	37711.8	39007.4	−14.81	−0.23	
2027.5	100	−80	240	5984.0	14760.1	−49317.7	15927.0	51825.7	−72.10	67.93	−52.07

Date	Height (km)	Lat (deg)	Lon (deg)	Xdot (nT/yr)	Ydot (nT/yr)	Zdot (nT/yr)	Hdot (nT/yr)	Fdot (nT/yr)	Idot (deg/yr)	Ddot (deg/yr)
2025.0	0	80	0	−8.3	59.5	31.1	−7.0	30.1	0.01	0.52
2025.0	0	0	120	9.5	−23.1	79.4	9.6	−11.2	0.11	−0.03
2025.0	0	−80	240	33.3	−8.6	95.5	4.0	−89.6	0.03	−0.12
2025.0	100	80	0	−7.7	56.5	28.7	−6.9	27.6	0.01	0.52
2025.0	100	0	120	9.2	−21.0	72.9	9.2	−10.0	0.11	−0.03
2025.0	100	−80	240	30.6	−8.0	89.2	3.9	−83.8	0.03	−0.11
2027.5	0	80	0	−8.3	59.5	31.1	−5.6	30.3	0.01	0.53
2027.5	0	0	120	9.5	−23.1	79.4	9.6	−10.7	0.11	−0.03
2027.5	0	−80	240	33.3	−8.6	95.5	4.2	−89.5	0.04	−0.12
2027.5	100	80	0	−7.7	56.5	28.7	−5.6	27.8	0.01	0.52
2027.5	100	0	120	9.2	−21.0	72.9	9.3	−9.7	0.11	−0.03
2027.5	100	−80	240	30.6	−8.0	89.2	4.0	−83.7	0.03	−0.11

Table 7: WMMHR2025 test values. The computation was carried out with double precision arithmetic. Single precision arithmetic can cause differences of up to 0.1 nT. Heights are with respect to the WGS 84 Ellipsoid. Grid Variation is with respect to the Grid North of the Universal Polar Stereographic projection.

Date	Height (km)	Lat (deg)	Lon (deg)	X (nT)	Y (nT)	Z (nT)	H (nT)	F (nT)	I (deg)	D (deg)	GV (deg)
2025.0	0	80	0	6517.4	144.8	54701.3	6519.0	55088.3	83.20	1.27	1.27
2025.0	0	0	120	39643.1	−100.3	−10580.7	39643.2	41030.9	−14.94	−0.14	
2025.0	0	−80	240	6136.3	15740.2	−52096.7	16894.0	54767.4	−72.03	68.70	−51.30
2025.0	100	80	0	6218.6	81.8	52567.3	6219.1	52933.9	83.25	0.75	0.75
2025.0	100	0	120	37679.1	−98.7	−10148.9	37679.3	39022.1	−15.07	−0.15	
2025.0	100	−80	240	5916.0	14762.5	−49580.3	15903.8	52068.5	−72.22	68.16	−51.84
2027.5	0	80	0	6494.8	293.5	54779.0	6501.5	55163.4	83.23	2.59	2.59
2027.5	0	0	120	39667.0	−159.1	−10383.9	39667.3	41003.9	−14.67	−0.23	
2027.5	0	−80	240	6218.5	15719.7	−51860.8	16905.0	54546.5	−71.95	68.42	−51.58
2027.5	100	80	0	6197.8	223.2	52638.8	6201.8	53002.9	83.28	2.06	2.06
2027.5	100	0	120	37702.1	−152.0	−9968.1	37702.4	38997.9	−14.81	−0.23	
2027.5	100	−80	240	5991.6	14743.3	−49359.7	15914.3	51861.8	−72.13	67.88	−52.12

Date	Height (km)	Lat (deg)	Lon (deg)	Xdot (nT/yr)	Ydot (nT/yr)	Zdot (nT/yr)	Hdot (nT/yr)	Fdot (nT/yr)	Idot (deg/yr)	Ddot (deg/yr)
2025.0	0	80	0	−9.0	59.5	31.1	−7.7	29.9	0.01	0.52
2025.0	0	0	120	9.6	−23.5	78.7	9.6	−11	0.11	−0.03
2025.0	0	−80	240	32.9	−8.2	94.4	4.3	−88.4	0.03	−0.11
2025.0	100	80	0	−8.3	56.6	28.6	−7.6	27.5	0.01	0.52
2025.0	100	0	120	9.2	−21.3	72.3	9.2	−9.9	0.11	−0.03
2025.0	100	−80	240	30.2	−7.7	88.2	4.1	−82.8	0.03	−0.11
2027.5	0	80	0	−9.0	59.5	31.1	−6.3	30.1	0.01	0.53
2027.5	0	0	120	9.6	−23.5	78.7	9.7	−10.6	0.11	−0.03
2027.5	0	−80	240	32.9	−8.2	94.4	4.5	−88.3	0.04	−0.11
2027.5	100	80	0	−8.3	56.6	28.6	−6.3	27.7	0.01	0.52
2027.5	100	0	120	9.2	−21.3	72.3	9.3	−9.5	0.11	−0.03
2027.5	100	−80	240	30.2	−7.7	88.2	4.3	−82.7	0.03	−0.11

2. Construction of the models

2.1 Background on the geomagnetic field

The Earth's magnetic field ($\mathbf{B}$) is a vector quantity varying in space ($\mathbf{r}$) and time (t). The field, as measured by a magnetic sensor on or above the Earth's surface, is actually a composite of several magnetic field contributions, generated by a variety of sources. These fields are superimposed and the sources and fields interact through inductive processes with each other. The most important of these geomagnetic sources are:

- Core field, $\mathbf{B}_{\text{core}}$, generated in Earth's conducting, fluid outer core;
- Crustal field, $\mathbf{B}_{\text{crust}}$, from Earth's crust/upper mantle;
- Combined disturbance field, $\mathbf{B}_{\text{disturbance}}$, from electrical currents flowing in the upper atmosphere and magnetosphere, which also induce electrical currents in the sea and the ground

The observed magnetic field is a sum of contributions:

$$\mathbf{B}(\mathbf{r},t) = \mathbf{B}_{\text{core}}(\mathbf{r},t) + \mathbf{B}_{\text{crust}}(\mathbf{r}) + \mathbf{B}_{\text{disturbance}}(\mathbf{r},t) \tag{21}$$

$\mathbf{B}_{\text{core}}$ dominates the field, accounting for over 95% of the field strength at the Earth's surface. *Secular variation* is the slow change in time of $\mathbf{B}_{\text{core}}$. The field arising from magnetized crustal rocks, $\mathbf{B}_{\text{crust}}$, varies spatially, but is nearly constant for the time-scales considered here. In most locations $\mathbf{B}_{\text{crust}}$ is much smaller in magnitude than $\mathbf{B}_{\text{core}}$ but can have significant local impact on magnetic compass devices. The field arising from currents flowing in the ionosphere and magnetosphere and their resultant induced currents in the Earth's mantle and crust, $\mathbf{B}_{\text{disturbance}}$, varies both with location and time.

$\mathbf{B}_{\text{crust}}$ exhibits spatial variations ranging from meters to thousands of kilometers and cannot be fully modeled with low-degree spherical harmonic models. The WMM does not account for contributions from the crust, except for those of very long wavelength, which are masked by the core field, whereas the WMMHR includes a much greater contribution from the crust (see Section 2.3). $\mathbf{B}_{\text{crust}}$ is generally smaller at sea than on land and decreases with increasing altitude (like the core field, but much more rapidly as its sources are near the Earth's surface and its power spans a wide range of spatial scales). The rock magnetization resulting in $\mathbf{B}_{\text{crust}}$ may be induced by the core field, be remnant from the time of formation, or result from a combination of both.

Figure 5 shows the various current systems flowing in the magnetosphere. The disturbance field can vary regularly, with fundamental periods of one day and one year, as well as irregularly on time scales of seconds to days. The regular variations are both diurnal and annual, and are essentially generated by the daylit atmosphere at altitudes of 100–130 kilometers, ionized by the Sun's radiation and, moved in the Earth's magnetic field by winds and tides, thus producing the necessary conditions (motion of a conductor in a magnetic field) for a dynamo to operate. Further daily and annual variations are caused by the rotation of the Earth in the magnetospheric field, which is approximately fixed in orientation relative to the Sun. The irregular variations in the disturbance field are due to magnetic storms and sub-storms. Magnetic storms generally have three phases: an initial phase, often with a sudden commencement and increased horizontal field at mid-latitudes; a main phase; and a recovery phase. The main phase involves an intensification of the ring current (Figure 5) from the plasma sheet.

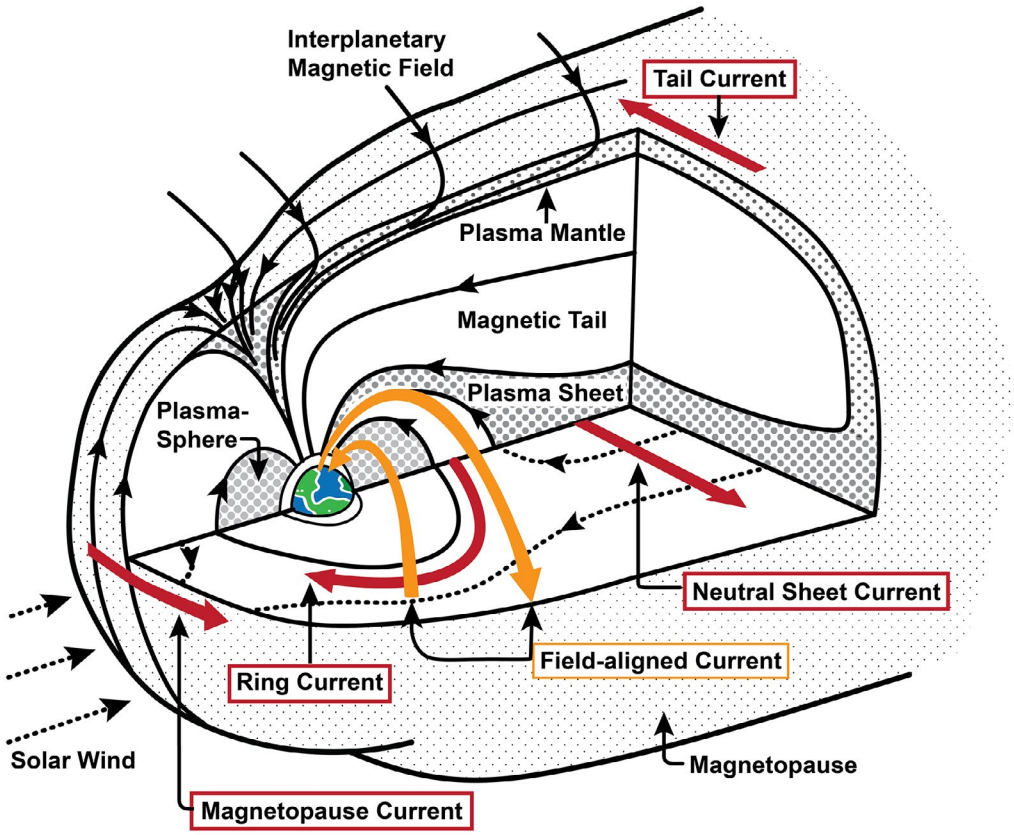

Figure 5: Current systems of the magnetosphere.

During the recovery phase the ring current returns to normal over a number of days and associated sub-storms subside. Magnetic storm and sub-storm effects are generally more severe at high geomagnetic latitudes where the ionized region of the upper atmosphere (i.e., the ionosphere) is coupled to the magnetosphere by field-aligned currents. They are therefore strongly influenced by the interplanetary magnetic field and current systems in the magnetotail. Both the regular and irregular disturbance field variations are modulated by season and the solar magnetic activity cycle. The primary disturbance field is often known as the external field, as its main sources, the ionosphere and magnetosphere, are external to the surface of the Earth where geomagnetic measurements have been traditionally observed. However, this term can be confusing when using satellite data, as the ionospheric dynamo region (100–130 kilometers) is below satellite altitude and therefore effectively internal to the orbital region. For further information about the crustal and disturbance fields, and general information about geomagnetism, see Merrill et al. (1996) and Parkinson (1983).

2.2 Data acquisition and quality control

To create an accurate magnetic field model, it is necessary to have vector component measurements with good global coverage and low noise levels. The three satellites of the European Space Agency (ESA) Swarm mission, launched in November 2013, are presently the most suitable global magnetic field observing system. Ground observatory hourly mean data are also available. Although poorer in spatial coverage, the observatory data can provide valuable constraints on the time variations of the geomagnetic field.

2.2.1 Satellite data

The principal characteristic of satellite data is global coverage using consistent instrumentation collected within a relatively short time span. The inclination of the orbit (the angle between the plane containing the satellite's path and the Earth's equatorial plane) determines the latitudinal extent of the data coverage: an inclination of

90° provides 100% coverage, an inclination of slightly less or slightly more than 90° results in gaps with no data for small regions around the geographic poles. Another important characteristic of satellite data is that localized, small-scale crustal magnetization and electromagnetic induction effects close to the Earth surface are strongly attenuated at satellite altitude, resulting in a cleaner magnetic environment for measuring the main field.

The three Swarm satellites slowly drift in local time (details below) with the Earth rotating beneath them. Thus, they provide a crude picture of the entire Earth within 24 hours. During this time each satellite completes about 15 orbits, with a longitudinal spacing of around 24 degrees. Swarm data were used in the production of the WMM2025 and WMMHR2025.

2.2.1.1 SWARM

Swarm is an ESA mission designed for studying all aspects of the Earth's magnetic field. Swarm is composed of three satellites, two of which fly in a constellation at a lower altitude while the third flies higher and is not synchronized with the lower pair (Friis-Christensen et al., 2006). The Swarm satellites were built by Astrium and launched on November 22, 2013 from Plesetsk in Russia on a Rokot launcher into a low Earth orbit. The planned mission duration was four years; however, funding for the satellite's lifetime has been extended multiple times.

Satellite and orbit

Swarm is composed of three satellites (A, B, C) which all fly in near-polar orbits. The lower pair (A and C) have inclinations of 87.4° and altitudes of about 470 km in late 2024, while the higher satellite (B) has an inclination of about 87.8° and an altitude of about 510 km. The satellites complete an orbit in approximately 90 minutes at a speed of about 8 km/s. Each satellite weighed 468 kg at launch, and is just over 9 m in length with the boom deployed.

Magnetometers

Each Swarm satellite carries a Vector Field Magnetometer (VFM) mid-boom (Figure 6), built by the Danish Technical University. The VFMs are tri-axis fluxgate magnetometers sampling the field at 50 Hz. Once calibrated, they have an accuracy better than 1 nT. Additionally, there is an Absolute Scalar Magnetometer (ASM) at the tip of the boom used to perform an absolute calibration of the vector instruments. Each ASM has a redundant sensor. These were built by the French Atomic Energy Commission - Laboratoire d'Electronique de Technologie et d'Instrumentation (CEA-Leti), under a contract with the French National Center for Space Studies (CNES). The scalar magnetometers are optically-pumped metastable helium-4 magnetometers, sampling the field at 1 Hz in nominal mode, and at 250 Hz in a so-called "burst" mode. They have a resolution of 0.1 nT and an absolute accuracy better than 0.3 nT.

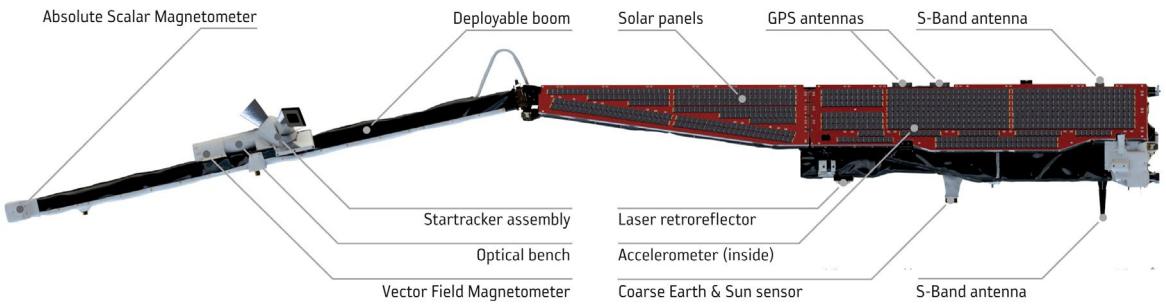

Figure 6: Swam instruments. On each satellite, the scalar magnetometer is located at the top of the boom. The vector fluxgate magnetometer is located mid-boom, about 1.6 m from them, and is co-mounted with the star imagers.

Star imagers

A star imager, developed and supplied by the Danish Technical University, provides satellite attitude control. An ultra-stable optical bench connects the star imager and the vector magnetometer. Attitude uncertainty is the largest source of error in satellite vector magnetic data. Star imagers are often blinded by the sun or moon and provide an unreliable attitude with regard to rotations about their direction of vision (bore sight). For this reason, Swarm is equipped with a triple-head star imager, while earlier magnetic satellites were equipped with single-head (Ørsted) or dual-head (CHAMP) star imagers.

Global positioning system (GPS) receivers

Each Swarm satellite is equipped with a dual frequency GPS receiver providing precise positioning and time-tagging of the data acquired by the instruments. Precise positioning is also used for spacecraft control. The GPS receivers were provided by ESA.

Data products

Swarm's standard data products are labeled from level-0 to level-2, according to the amount of processing applied to the original data. Level-0 products are raw measurements from the onboard instruments. Level-1 products are processed raw measurements that are in physical units, as well as having transformations applied so that they are in useful coordinate systems (e.g., geographic). Level-2 refers to scientific products (e.g., field models) which make direct use of the Level-1 data. The data used for the WMM2025 and WMMHR2025 comes from the most recent Level-1(b) Swarm dataset (version 0605 and later), which is freely provided by ESA.

2.2.1.2 In-orbit calibration of satellite magnetometers

Experience with several satellite missions shows that calibration parameters can change significantly during deployment into space. Furthermore, calibration parameters exhibit gradual changes over the life of the mission. Regular in-flight calibration and updates of the respective parameters is therefore essential. To enable a successful calibration in orbit, it is of critical importance that the instruments be built in such a way that they can be described by a linear model with constant (over one day) calibration parameters. While these parameters may change slowly over the mission lifetime, they must be independent of strength or direction of the ambient magnetic field. In particular, past satellite magnetic missions have shown that it is not possible to perform an in-orbit scalar calibration of a vector magnetometer when the component readings suffer from a "transverse field effect" (Brauer et al., 1997).

The linear instrument model used for Swarm is similar to the one previously used to successfully calibrate the Danish Ørsted satellite (Olsen et al., 2003). It can be formulated as a linear transform from the desired quantity $\mathbf{B}$, the magnetic field vector in the reference frame of the star tracker, to the instrument output vector $\mathbf{E}$ as

$$\mathbf{E} = \underline{\mathbf{S}}\ \underline{\mathbf{P}}\ \underline{\mathbf{R}}\ \mathbf{B} + \mathbf{b} \tag{22}$$

where $\underline{\mathbf{S}}$ is a diagonal matrix of scale factors, $\underline{\mathbf{P}}$ corrects for non-orthogonalities of the sensor elements, $\underline{\mathbf{R}}$ rotates from the star tracker reference frame into the vector magnetometer frame, and $\mathbf{b}$ is the offset vector. Each of these corrections generally has three parameters which have to be determined in the calibration. (The Swarm calibration incorporates the characterization of a Sun-driven disturbance field which includes more parameters, see Tøffner-Clausen et al., 2016).

The scalar in-orbit calibration is based on a comparison between the readings of the scalar and vector magnetometer. In a least-squares estimation procedure, the nine calibration parameters of a fluxgate can be determined. Here, the synthetic laboratory test field is replaced by the natural ambient field recorded over a day. This allows for regular verification of the offset vector $\mathbf{b}$, non-orthogonalities $\underline{\mathbf{P}}$, and scale factors $\underline{\mathbf{S}}$.

The calibration parameters of the matrix $\underline{\mathbf{R}}$, namely the three rotation angles between the magnetometer and star tracker reference systems, are determined in a final, independent step. To determine these angles, one makes use of the fact that div($\mathbf{B}$) is zero, and chooses measurements outside of the auroral current regions, where curl($\mathbf{B}$) is also zero. Under these circumstances, the effect of misalignments of the star tracker and vector magnetometer reference system can be separated cleanly from genuine magnetic fields, and the three calibration parameters of the matrix $\underline{\mathbf{R}}$ can be determined by a least-squares inversion. This calibration can only succeed if the vector magnetometer and the star tracker are co-mounted onto an optical bench with sufficient rigidity and temperature stability.

2.2.2 Observatory data

One of the principal characteristics of observatory data is the long-term continuous coverage over time. The spatial distribution of observatories is largely determined by the location of habitable land and by the availability of local expertise, funds and energy supply. While the distribution is uneven and sparse compared to that of satellite data, it has been reasonably constant in time (Figure 7).

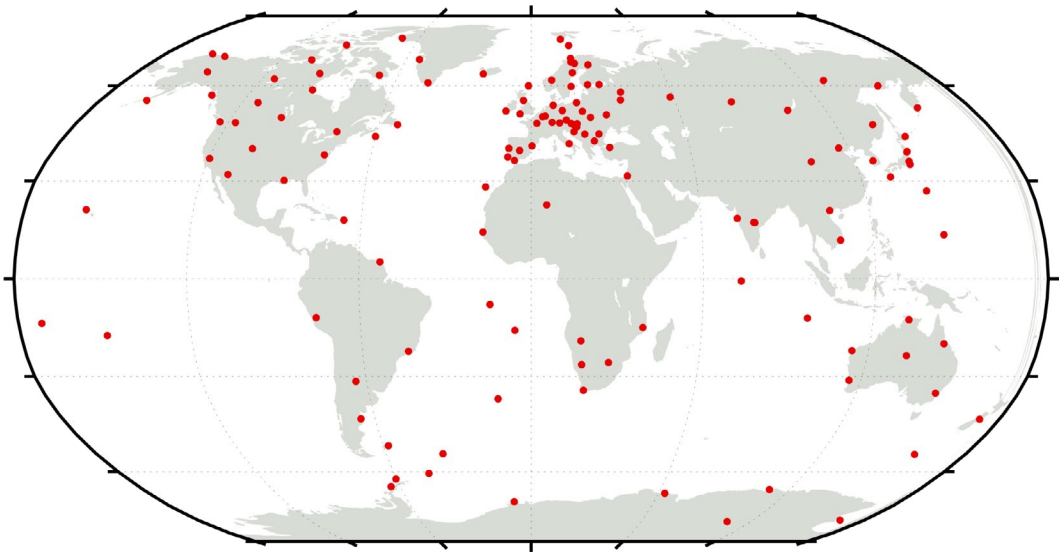

Figure 7: Locations of observatories whose data contributed to the BGS parent model.

Instrumentation

There are three categories of instruments at an observatory. The first category comprises variometers, which make continuous measurements of elements of the geomagnetic field vector. Both analog and digital variometers require temperature-controlled environments, extremely stable platforms, and can generally operate without manual intervention. Today, the most common type of variometer is the tri-axial fluxgate magnetometer.

The second category comprises absolute instruments that can make measurements of the magnetic field in terms of absolute physical basic units or universal physical constants. The most common types of absolute instrument are the fluxgate theodolite, for measuring D and I, and the proton precession magnetometer for measuring F. In the former instrument the basic unit of measurement is an angle. To determine these angles, the fluxgate sensor mounted on the telescope of a non-magnetic theodolite is used to detect when it is perpendicular to the magnetic field vector. With the fluxgate sensor operating in this null-field mode, the stability of the sensor and its electronics is maximized. To complete the determination of D and I, true north is found by reference to a fixed mark of known azimuth, usually by astronomical observations. In a proton

precession absolute magnetometer, the universal physical constant is the gyromagnetic ratio of the proton. Measurements with a fluxgate theodolite can only be made manually while a proton magnetometer can operate automatically.

The third category comprises semi-absolute instruments. These instruments measure deviations from a field, which is determined on a regular basis using an absolute instrument. One example is a proton vector magnetometer where artificial orthogonal bias fields are applied to a proton precession magnetometer sensor, located at the center of a set of coils through which currents can be passed, to obtain the components of the field vector. Like variometers, these instruments are temperature-sensitive and require stable platforms. For more information on magnetic instrumentation and operation of magnetic observatories, see Macmillan (2007), Jankowski and Sucksdorff (1996), and Chulliat et al. (2017).

Data collection and quality control

BGS and NOAA actively collect observatory data through their involvement in the World Data Center (WDC) system. They maintain databases suitable for magnetic field modeling, maintain contacts with organizations operating magnetic observatories, and collaborate with other WDCs. Each year BGS sends requests to all organizations with operating observatories for the latest data and other relevant information. The WDCs for geomagnetism benefit greatly from the efforts of INTERMAGNET, an organization whose objectives are to establish a global network of cooperating digital magnetic observatories, to adopt modern standard specifications for measuring and recording equipment, and to facilitate data exchange and the production of geomagnetic products in close to real time. In addition to operating nine of the observatories shown in Figure 7, BGS runs one of five INTERMAGNET GINs (Geomagnetic Information Node) and the data portal, and plays a leading role in the organization.

The hourly means used in the WMM were selected from definitive data held at the WDC for Geomagnetism, Edinburgh and from recent quasi-definitive data (Peltier and Chulliat, 2010; Clarke et al., 2013) produced primarily by INTERMAGNET observatories. The quality of the data an observatory produces is the responsibility of the operator. The most important aspect of the quality for global modeling is the stability of the baseline, the difference between the calibrated variometer data and the absolute observations. A baseline with many points, low scatter, few drifts and offsets is an indicator of good quality. Baseline plots for the INTERMAGNET observatories are available along with their definitive data.

Quality assurance and control measures, other than those carried out by the observatory operators, are also accomplished by INTERMAGNET through its observatory standardization program, the WDCs, and by participation in the International Association of Geomagnetism and Aeronomy (IAGA) Division V Observatory Workshops.

Final quality control procedures prior to deriving the WMM are completed by BGS. For the hourly means this involves plotting all data to identify typographical errors and large offsets, and then plotting residuals to hourly models to identify remaining measurement artefacts such as noise, small offsets, and trends. Hourly spherical harmonic models of degree nine and order one are fit to residuals after estimates of the core, crustal and ionospheric fields are removed from the observatory hourly means, the details of which are in Macmillan and Olsen (2013). (Although these models are not realistic magnetospheric field models, they help reduce signals that are coherent in time and space.) Observatories used in the production of WMM2025 are listed in Table 8.

Table 8: Observatories used in production of BGS parent model. An asterisk (*) with the IAGA code indicates observatories for which the record contains an unquantified jump, about which data series are split and treated as independent series. The number of data indicates the number of vector triples or scalar values used from each location.

IAGA code	Name	Latitude [°]	Longitude [°]	Altitude [m]	Number of data
ABG*	Alibag	18.638	72.872	7	2403
ABK	Abisko	68.358	18.823	380	2566
AIA	Faraday Islands (Argentine Island) – Akademik Vernadsky base	−65.245	−64.258	10	2348
API	Apia	−13.816	−171.781	2	1359
ARS	Arti	56.433	58.567	290	1200
ASC	Ascension Island	−7.950	−14.380	177	2646
ASP	Alice Springs	−23.762	133.883	557	2830
BDV	Budkov	49.080	14.020	496	2578
BEL	Belsk	51.836	20.789	180	2558
BFO	Black Forest	48.331	8.325	641	2297
BGY	Bar Gyora	31.723	35.088	750	951
BJN	Bear Island	74.500	19.200	80	2543
BLC	Baker Lake	64.318	−96.012	30	1519
BMT	Beijing Ming Tombs	40.300	116.200	183	2226
BOU	Boulder	40.140	−105.233	1682	2810
BOX	Borok	58.070	38.230	115	1897
BRD	Brandon	49.870	−99.974	380	2340
BRW	Barrow	71.320	−156.620	12	2877
BSL	Stennis Space Center (Bay St. Louis)	30.350	−89.640	8	2199
CBB	Cambridge Bay	69.123	−105.031	20	1931
CBI	Chichijima	27.096	142.185	155	2733
CKI	Cocos (Keeling) Islands	−12.188	96.834	3	2765
CLF	Chambon−la−Foret	48.025	2.260	145	2615
CMO	College	64.870	−147.860	197	2893
CNB	Canberra	−35.320	149.360	859	2787
COI	Coimbra	40.223	−8.418	99	1704
CPL*	Choutuppal	17.294	78.919	360	1788
CSY	Casey Station	−66.283	110.533	41	2773
CTA	Charters Towers	−20.090	146.264	370	2484
CYG	Cheongyang	36.370	126.854	165	1687
DLT	Dalat	11.950	108.480	1583	1260
DOB	Dombas	62.073	9.117	660	2507
DOU	Dourbes	50.100	4.600	225	2595
DUR	Duronia	41.650	14.470	920	1696
EBR	Ebro	40.957	0.333	532	2604
ESA	Esashi	39.237	141.355	396	1305
ESK	Eskdalemuir	55.314	−3.206	245	2636
EYR	Eyrewell	−43.474	172.393	102	2344
FCC	Fort Churchill	58.759	−94.088	15	2237
FRD	Fredericksburg	38.210	−77.367	69	2784

IAGA code	Name	Latitude [°]	Longitude [°]	Altitude [m]	Number of data
FRN	Fresno	37.090	−119.720	331	2676
FUR	Furstenfeldbruck	48.170	11.280	572	2419
GAN*	Gan International Airport	−0.695	73.154	2	2077
GCK	Grocka	44.633	20.767	231	1858
GDH	Qeqertarsuaq (Godhavn)	69.252	−53.533	24	2564
GNG	Gingin	−31.356	115.715	50	2806
GUI	Guimar	28.321	−16.441	868	2033
GUA	Guam	13.590	144.870	140	2352
HAD	Hartland	51.000	−4.480	95	2636
HBK	Hartebeesthoek	−25.880	27.710	1555	2273
HER	Hermanus	−34.430	19.230	26	2577
HLP*	Hel	54.604	18.811	1	2559
HON	Honolulu	21.320	−158.000	4	2408
HRB	Hurbanovo	47.873	18.190	120	2419
HRN	Hornsund	77.000	15.550	15	2393
HUA	Huancayo	−12.050	−75.330	3313	2294
HYB	Hyderabad	17.420	78.550	500	2380
IQA*	Iqaluit	63.753	−68.518	67	1742
IRT	Irkutsk (Patrony)	52.170	104.450	478	1946
IZN	Iznik	40.500	29.720	256	2309
JCO	Jim Carrigan Observatory	70.356	−148.799	20	2828
KAK	Kakioka	36.232	140.186	36	2820
KDU	Kakadu	−12.690	132.470	15	2815
KEP	King Edward Point	−54.282	−36.493	7	2723
KHB	Khabarovsk	47.610	134.690	92	2189
KIR*	Kiruna	67.843	20.420	395	2299
KIV	Kiev	50.720	30.300	140	1578
KMH	Keetmanshoop	−26.540	18.110	1065	2026
KNY	Kanoya	31.420	130.880	107	2762
KNZ	Kanozan	35.256	139.956	342	1980
KOU	Kourou	5.210	−52.730	10	2674
LER	Lerwick	60.138	−1.183	85	2636
LIV	Livingston Island	−62.662	−60.395	19	1865
LON	Lonjsko Polje	45.408	16.659	95	2470
LRM	Learmonth	−22.220	114.100	4	2801
LRV	Leirvogur	64.183	−21.700	5	2657
LVV	Lviv	49.900	23.750	326	1771
LYC	Lycksele	64.612	18.748	270	2573
LZH	Lanzhou	36.087	103.845	1560	1353
MAB*	Manhay	50.298	5.682	440	2467
MAW	Mawson	−67.600	62.880	12	2660
MBO	Mbour	14.390	−16.960	7	1364
MCQ*	Macquarie Island	−54.500	158.950	4	2830

IAGA code	Name	Latitude [°]	Longitude [°]	Altitude [m]	Number of data
MEA	Meanook	54.616	−113.347	700	2577
MGD	Magadan	60.051	150.728	226	2228
MIZ	Mizusawa	39.112	141.204	125	1922
MMB	Memambetsu	43.910	144.190	42	2789
MOS	Krasnaya Pakhra (Moscow)	55.467	37.317	200	1454
NAQ	Narsarsuaq	61.167	−45.433	4	1779
NCK	Nagycenk	47.630	16.720	153	1668
NEW	Newport	48.270	−117.120	770	2715
NGK	Niemegk	52.070	12.680	78	2577
NMP	Nampula	−15.089	39.254	374	822
NUR	Nurmijarvi	60.510	24.660	105	2102
NVS	Novosibirsk (Klyuchi)	54.850	83.230	130	2625
ORC	Orcadas	−60.737	−44.737	3	1782
OTT	Ottawa	45.403	−75.552	75	2493
PAG*	Panagjurishte	42.515	24.177	556	2262
PET	Paratunka (Petropavlovsk)	52.971	158.248	50	2332
PHU	Phuthuy	21.030	105.960	5	947
PIL	Pilar	−31.667	−63.881	336	2458
PPT*	Pamatai (Papeete)	−17.567	−149.574	357	2584
PST	Port Stanley	−51.700	−57.890	135	2670
RES	Resolute Bay	74.690	−94.895	30	2694
SBA	Scott Base	−77.829	166.671	130	2462
SBL	Sable Island	43.932	−60.010	5	2746
SFS	San Fernando	36.667	−5.945	111	2035
SHE	Saint Helena	−15.961	−5.747	586	2459
SHU*	Shumagin	55.350	−160.460	80	2324
SIT	Sitka	57.060	−135.330	24	2809
SJG	San Juan	18.110	−66.150	424	2279
SOD	Sodankyla	67.370	26.630	178	1865
SPG	Saint Petersburg	60.542	29.716	46	1198
SPT	San Pablo−Toledo	39.550	−4.350	922	2575
STJ	St Johns	47.595	−52.677	100	2058
STT	San Teotonio	37.547	−8.728	115	1111
SUA	Surlari	44.680	26.250	84	2648
TAM	Tamanrasset	22.790	5.530	1373	2544
TDC	Tristan da Cunha	−37.067	−12.316	41	1376
THL	Qaanaaq (Thule)	77.470	−69.227	57	2732
THY	Tihany	46.900	17.890	187	2572
TRO	Tromso	69.663	18.948	105	2548
TRW	Trelew	−43.267	−65.383	15	840
TSU	Tsumeb	−19.202	17.584	1273	2295
TUC	Tucson	32.170	−110.730	946	2804
UPS	Uppsala (Fiby)	59.903	17.353	50	2577

IAGA code	Name	Latitude [°]	Longitude [°]	Altitude [m]	Number of data
VAL	Valentia	51.933	−10.250	14	1292
VIC	Victoria	48.520	−123.420	197	2683
VNA	Neumayer Station III	−70.683	−8.282	46	2360
VOS	Vostok	−78.464	106.835	3488	533
VSS	Vassouras	−22.400	−43.650	457	2735
WIC	Conrad Observatory	47.931	15.866	1088	2094
WNG	Wingst	53.725	9.053	66	2560
YAK	Yakutsk	61.960	129.660	100	1381
YKC	Yellowknife	62.480	−114.482	198	1171

2.2.3 Other data and derived products

Other types of magnetic data and products used in the production of the WMM2025 and WMMHR2025 are: various magnetic activity indices derived from observatory data and solar wind data measured by the measured by the ACE and DSCOVR satellites. These are used to either select the data for input to the model or to form part of the input to the model.

Index Kp

The planetary Kp ("planetarische Kennziffer") index (Bartels, 1957; Matzka et al., 2021; https://kp.gfz.de/en/) is based on the K-index, a local index of the three-hourly range in magnetic activity of the two horizontal field components (X and Y) relative to an assumed quiet-day curve for the geomagnetic observatory. Local disturbance levels are determined by measuring the range (difference between the highest and lowest values) during three-hour time intervals for the most disturbed magnetic field component. The range is then converted into a local K-index according to a pseudo-logarithmic scale, which is station-specific, in an attempt to normalize the frequency of the different disturbance sizes. The three-hourly Kp index is the average of local K values from 13 selected subauroral stations and is expressed in a scale of thirds (28 values). The IAGA station codes (in order of geomagnetic latitude) are: LER, MEA, SIT, ESK, UPS, OTT, BFE (Brorfelde), HAD, WNG, NGK, FRD, CNB, and EYR. Prior to the averaging, the K values are standardized according to station and season. Also, CNB and EYR are averaged first, as are UPS and BFE and then used as single points in the overall average of eleven. The Kp index is used to select measurements during magnetically undisturbed times.

Indices Dst and RC

Charged particles trapped by the geomagnetic field in the magnetosphere drift around the Earth at a distance of 3-8 Earth radii creating a westward electric ring current whose field opposes the main geomagnetic field. The strength of this field is on the order of tens of nT during quiet times and several hundred nT during magnetic storms. Magnetopause, tail and partial ring currents represent additional contributions leading to asymmetries in the field which increase during storms. The symmetric part of this composite disturbance field is tracked by the Dst (disturbance storm-time) index (Sugiura, 1964; https://wdc.kugi.kyoto-u.ac.jp/dstdir) and the RC (ring current) index (Olsen et al., 2014; https://www.spacecenter.dk/files/magnetic-models/RC/current). The Dst index is derived from measurements collected at four low-latitude observatories. The RC index is derived from measurements at 21 mid- and low-latitude observatories and is generally thought to more accurately track the quiet-time ring current field at ground and low Earth orbit altitude. The Dst and RC indices and their time derivatives are used for data selection.

Interplanetary magnetic field

The solar wind drives electric currents in the Earth's magnetosphere and ionosphere. An interplanetary magnetic field (IMF) is carried by the plasma of the solar wind. Relevant for the response of the magnetosphere is the speed of the solar wind and the direction and strength of the IMF. These solar wind parameters are monitored by NASA's Advanced Composition Explorer (ACE) satellite and NOAA's Deep Space Climate Observatory (DSCOVR) satellite. Using magnetospheric models, the ACE solar wind measurements are projected downstream onto the magnetospheric bow shock (the boundary between the solar wind and the magnetosphere) and are made available by NASA as 1-minute readings in geocentric magnetospheric coordinates via OMNIWeb at NASA's Space Physics Data Facility (SPDF). The IMF is used both for data selection and as a quantitative parameter to correct for magnetospheric disturbance fields.

Merging electric field E_m

The merging electric field, derived from the IMF and solar wind speed (available via OMNIWeb), is a parameter suitable for describing the variation of the magnetospheric tail current field. Following Kan and Lee (1979), the merging electric field, E_m, is calculated as

$$E_m = v_{SW} \left(B_y^2 + B_z^2\right)^{1/2} \sin^2 \frac{\Theta}{2} \tag{23}$$

where v_{SW} is the solar wind velocity, B_y and B_z are the IMF components in the Geocentric Solar Magnetospheric (GSM) frame and Θ is the clock angle of the IMF (i.e., the angle made by the B_y and B_z components of the IMF in the vertical plane to the ecliptic, counted from 0 when IMF B_z is north). Here we use a revised definition of the merging electric field, following Newell et al. (2007) and Olsen et al. (2014):

$$E_m = 0.33\, v_{SW}^{4/3} \left(B_y^2 + B_z^2\right)^{2/3} \sin^{8/3} \frac{\Theta}{2} \tag{24}$$

The merging electric field is used for data selection.

2.3 Derivation of the models

The WMM and WMMHR are jointly developed by NCEI and BGS. Both groups used separate, completely independent processing chains, reflecting different modeling strategies, and produced their own sets of WMM and WMMHR coefficients, referred to as *candidate models* in what follows. The derivations of the NCEI and BGS candidate models are described in Subsections 2.3.1 and 2.3.2, respectively. The candidate models are then validated and cross-validated using the techniques outlined in Subsection 2.3.3. For this release, the final WMM2025 and WMMHR2025 coefficients were obtained by averaging the NCEI and BGS main field and secular variation coefficients for each model.

The final WMM2025 and WMMHR2025 coefficients are provided with one decimal place and four decimal places, respectively. This applies to both the main field and secular variation coefficients. Also, the WMM2025 coefficients, which range from degree one to 12, are rounded versions of the WMMHR2025 coefficients for degrees one to 12. To achieve the required level of precision for each model and ensure consistency between the rounded versions, NCEI and BGS derived candidate models with three decimal places for the WMM and five decimal places for the WMMHR.

The WMMHR extends the WMM to spherical harmonic degree and order 133. The main field coefficients for degrees 16 to 133 of the WMMHR are derived from the MF7 crustal field model (Maus et al., 2008; https://geomag.colorado.edu/magnetic-field-model-mf7). The secular variation coefficients for degrees 16 to 133 of the WMMHR are set to zero. Therefore, the WMMHR candidate models derived by NCEI and BGS are for degrees one to 15, while the WMM candidate models are for degrees one to 12 (the full range).

Since the WMM and the WMMHR, truncated at degree 15, only describe the long-wavelength internal part of the geomagnetic field, it is important to separate unrelated contributions to the field that would otherwise contaminate their coefficients. Both the NCEI and BGS modeling strategies rely on four elements:

1. Data selection

Measurements during daytime and during periods of strong solar activity are contaminated by external current systems, which are difficult to accurately model. Therefore, only nighttime data measured during magnetically quiet periods, as inferred from the above-described indices, are used in estimating the WMM and WMMHR coefficients.

2. Data corrections

Some contributions to the measured magnetic field, such as the crustal magnetic field, can be accurately modeled and corrected prior to the estimation of the WMM and WMMHR coefficients.

3. Data weighting

The disturbance field includes features that, even after careful data selection, cannot be modelled. Also, polar orbiting satellites collect more data per unit area at high-latitudes than at low-latitudes. Data including these features may be downweighted in the estimation of the WMM and WMMHR coefficients.

4. Use of parent models

To account for contributions that have not been removed in the previous three steps, an extended set of model parameters is estimated as an intermediate step towards the WMM and WMMHR model coefficients. These parameters may account for smaller-wavelength internal magnetic field contributions (spherical harmonic degree greater than 12 or 15), higher time derivatives (e.g., secular acceleration or an extended time series of models), and contributions from currents external to the Earth. This extended set of model parameters is referred to as the *parent model* of the WMM and WMMHR.

2.3.1 NCEI candidate models

The NCEI candidate models for WMM2025 and WMMHR2025 were derived from a parent model, defined as a series of main field and secular variation models spanning epochs from 2018.5 to 2024.33, with a one-month time step. These models were constructed entirely from Swarm Alpha and Bravo satellite vector data, specifically from the level 1b MAGx_LR (1 Hz) data, baseline 0605/0606. No scalar data were used. The models included a parameterization of the main field to spherical harmonic degree and order 18, and a parameterization of the secular variation to spherical harmonic degree and order 15. In the following sections, we further describe the data selection and preprocessing, data weighting, the parent model, and the derivation of the NCEI candidate models.

Data selection

Prior to the data selection, the Swarm data were downsampled to one sample every 10 seconds. Swarm nominally samples the geomagnetic field at 1 Hz, which is a higher resolution than is needed for the WMM. To minimize contributions from external fields originating in the ionosphere and magnetosphere, data were

used only during certain local time periods when ionospheric contributions are minimal, and outside disturbed periods of geomagnetic activity, as tracked by geomagnetic activity indices. Additionally, erroneous Swarm measurements were removed from the dataset using flags indicating satellite maneuvers, star camera blinding, or other instrument errors, as well as outlier detection algorithms. The data selection criteria employed for the NCEI parent model are shown in Table 9.

Table 9: Data selection criteria for Swarm satellite data used when producing the NCEI candidate models.

Parameter	Description	Criterion
LT	Local time	00:00 ≤ LT ≤ 05:00
Kp, Kp_{-3h}	3-hour planetary Kp index at datum and in preceding 3-hour interval	0 ≤ Kp < 1+ 0 ≤ Kp_{-3h} < 1+
|Dst|	Absolute value of the Dst (disturbance storm-time) index	0 nT ≤ |Dst| < 20 nT
IMF By, IMF Bz	Interplanetary Magnetic Field (IMF) By and Bz components	− 3 nT < IMF By < 3 nT 0 nT < IMF Bz < 5 nT

Data corrections and weighting

The selected data were corrected for the static and smaller-scale crustal magnetic field using the MF7 model (Maus et al., 2008; https://geomag.colorado.edu/magnetic-field-model-mf7), and for the magnetospheric field using the CHAOS-7.18 model, which is parameterized by the RC index (Finlay et al., 2020; https://www.spacecenter.dk/files/magnetic-models/CHAOS-7/).

Despite careful data selection and preprocessing, inevitably a small number of erroneous measurements or measurements contaminated by external magnetic fields may still be included in the model. To minimize the impact of such measurements, the parent models were obtained through several iterations of model fitting, with additional weights assigned at each iteration to detect and downweight these outliers. This procedure, known as Iterative Reweighted Least Squares (IRLS), was implemented using Huber weights (Huber, 1996).

Parent model

The parent model consisted of a series of 71 main field and secular variation models fitted to one-year data windows, from 2018.5 to 2024.33, at 1/12-year intervals. For each data window, a main field model up to spherical harmonic degree and order 18 and a secular variation model up to spherical harmonic degree and order 15 were co-estimated. The epoch of both models was the center point of the window. The total number of parameters estimated for each model was 615, while the total number of parameters estimated across the entire procedure was 43,665. The main field models were regularized by minimizing the energy norm at the core-mantle boundary (Gubbins, 1983). The secular variation models were regularized using a single damping parameter applied to all coefficients.

Derivation of NCEI candidate models

As the parent model was prepared in late 2024, it was impossible to include data on or around the WMM and WMMHR epoch of 2025.0. The latest data included in the parent model estimation (and not rejected by the selection process) was collected on October 13, 2024. To derive candidate models at epoch 2025.0, cubic smoothing splines were first fitted to the series of parent model main field coefficients, for each individual coefficient. The cubic splines were then extrapolated until 2026.0 with a one-month time step. The candidate model main field coefficients for WMM and WMMHR were taken as the rounded versions, to three and five decimal places respectively, of the cubic spline values at 2025.0. The secular variation coefficients were obtained by taking the plus two-month minus two-month time derivative of the cubic splines at 2025.0, with the same rounding applied as the main field coefficients.

2.3.2 BGS candidate models

The BGS estimates of the main field and secular variation coefficients for WMM2025 were derived from an extended parent model. This parent model includes smaller wavelength spatial features, higher time derivatives of variations, and additional modelled contributions to Earth's observed field. From this parent model, the large-scale internal field and its secular variation could be more accurately extracted. The procedure for selecting, correcting and weighting data to produce the parent model, parameterizing the model, and extracting the desired coefficients, is described in the following sections.

Data selection

Two data sources were used to construct the parent model: (1) the ground observatory network, and (2) the ESA Swarm mission.

Data were collected from available ground observatory locations with the earliest and latest selected data spanning January 1, 2018 to October 6, 2024. The distribution of locations is shown Figure 7, and observatory details are summarized in Table 8. Vector observations were used at low- and mid-geomagnetic dipole latitudes (GMDL), while for high GMDL, a unit vector given by a prior BGS model of the internal geomagnetic field was used to project the vector observations to a pseudo-scalar field value in the prior unit vector direction. The projection of scalar data onto a prior model direction creates a linear relation between these data and the model coefficients for which we wish to solve. All data were transformed from the reported geodetic coordinate system to a geocentric coordinate system, and subject to selection for geomagnetically quiet, local night times, as summarised in Table 10. Observatory records that contained any unquantified jumps were split about these times and treated as independent data series. Such records are indicated with asterisks in Table 7.

Swarm data from the Alpha, Bravo and Charlie satellites were collected with the earliest and latest selected data spanning January 2, 2018 to September 11, 2024. The latest available data baselines were used, consisting of versions 0605 and 0606. Vector observations were used at all latitudes, with very few scalar observations used where vector data were not available. All data were subjected to a rigorous selection procedure for geomagnetically quiet periods. Low- and mid-GMDL data were used only during local night times to avoid the influence of solar-driven fields in the ionosphere, while high GMDL data were used at all local times to avoid seasonal gaps in the data. The data selection procedure is summarized in Table 10.

Table 10: Data selection criteria for Swarm satellite and ground observatory data used when producing the BGS parent model.

Filter	Description	Satellite	Observatory
Sampling		Every 20th 1Hz datum	Hourly mean
Kp, Kp_{-3h}	3−hour planetary K index at datum and in preceding 3-hour interval	≤ 2o, ≤ 2o	≤ 2_+
$\|D_{st}\|$ [nT], $\|dD_{st}/dt\|$ [nT·h−1]	Storm time disturbance and its rate of change per hour at datum	≤ 30, ≤ 2	–, ≤ 5
IMF |Bx|, |By| Bz [nT]	Projected Interplanetary Magnetic Field at datum	≤ 10, ≤ 3, 0 ≤ x ≤ 6	–, –, ≥ −2
v_{sw} [km·s^{-1}]	Projected solar wind velocity at datum	≤ 450	–
LT (<|55°GMD|)	Local time at GMD latitudes below |55°|	23:00 ≤ x ≤ 05:00	01:00 ≤ x ≤ 02:00
$\|d-d_{prior}\|$ [nT]	Absolute difference between datum and a prior BGS field model estimation	≤ 100	–
|F−|B|| [nT]	Absolute difference between ASM and magnitude of VFM data	≤ 2	–
E_{min} (>|55°GMD|) [mV·m^{-1}]	Hourly mean of 1-minute merging electric field (calculated after Olsen et al., 2014) at GMD latitudes above |55°|	≤ 0.8	–
z (°)	Zenith angle at GMD latitudes above |55°|	≥100.5	–

Data correction and weighting

A prior BGS crustal field model to spherical harmonic degree and order 100 was removed from all satellite and observatory data. Doing so allows the parent modelling process to perform a less complex calculation, solving only for the larger-scale and time varying parts of the observed field.

Data weights (variances) were assigned to each datum to account for local and global, small- and large-scale sources of uncertainty, following the scheme of Thomson et al. (2010). For satellite data, these weights were:

- Along-track standard deviation over each 20-second orbit segment of 1 Hz data, in each vector component and for the scalar field
- Disturbance field activity interpolated from measurements at the nearest three encompassing ground observatories (LAVA index, Thomson et al., 2010)
- Spatially uniform noise (2 nT standard deviation)
- Function of solar zenith angle, z, $(1+\cos(z))^2$
- Data density per unit area relative to the mean data density within 1° equal-area tesserae

For observatory data, these weights were:

- Spatially uniform noise for vector data below |55°| GMD latitude (2 nT standard deviation)
- Spatially uniform noise for projected scalar data above |55°| GMD latitude (6 nT standard deviation)
- Function of solar zenith angle, z, $(1+\cos(z))^2$
- Data density per unit area relative to the mean data density within 5° equal-area tesserae

A final scaling was applied to these weights such that the sum of the total weights of observatory data was approximately 10% of the sum of the total weights assigned to satellite data.

Model description

The BGS parent model co-estimates several field sources, and is parameterized as follows.

- Core field:
  - Spherical harmonic (SH) degree and order 15
  - Order-6 B-spline time dependence, with six-month spaced knots from 2018.0 to 2025.0
  - Regularized time integral of the third time derivative of the radial magnetic field over the core-mantle boundary (CMB)
  - Regularised 2nd time derivative of the radial magnetic field over the CMB, at the spline end knots
- Large-scale crustal field correction:
  - Static in time, described from SH degrees 16 to 30
  - Variation relative to the prior SH degree 100 crustal field model used to correct data
- Large-scale slowly varying external field:
  - SH degree and order 1
  - Order-2 B-spline time dependence, with 3 month spaced knots from 2018.0 to 2025.0
- Large-scale rapidly varying external and induced field:
  - SH degree and order 1
  - Order-1 B-spline time dependence scaled by the external and induced coefficients of the VMD index (Thomson and Lesur, 2007), and by Dst for the most recent period where insufficient observatory data is available to derive VMD, with three month spaced knots from 2018.0 to 2025.0

- Periodic variations:
  - SH degree and order 1, sine and cosine constants accounting for external and induced, annual and semi-annual variations
  - SH degree 1 order 1 only, external, offset, sine and cosine terms, order 1 B-spline with annual knots, parameterised by sun-synchronous longitude
- Local crustal biases:
  - Static offsets per vector or scalar field component at each observatory location to account for small-scale crustal field

The model was fit by robust iteratively-reweighted least-squares, and converged within three iterations. Damping values were chosen to balance the fit to the data against the level of temporal smoothing applied to the core field by the regularisation.

Derivation of BGS main field and secular variation candidate models

The BGS secular variation coefficients for 2025 to 2030 were taken to be the mean of the instantaneous secular variation coefficients of the parent model, from 2023.25 to 2024.25 in 0.1 year increments, inclusive. This period was chosen to be as up-to-date as possible given the data used, while avoiding end-effects of the temporal B-spline parameterisation. These secular variation coefficients were then used to calculate the BGS main field coefficients at 2025.0, by propagating the instantaneous main field coefficients of the parent model at 2024.5 forward in time by six months. The coefficients for the WMM and WMMHR candidates were taken from the same parent model, truncated to the appropriate precisions and maximum spherical harmonic degrees.

2.3.3 Validation process

Each candidate model was first validated by comparing it to other similar recent models (developed by NCEI, BGS, and other organizations, e.g. for the International Geomagnetic Reference Field) and to a global set of geomagnetic observatory data. While the observatory data comparison applies only to the secular variation (due to the existence of static, local crustal anomalies at each observatory that are difficult to entirely remove from observatory data), it provides a useful independent check of the secular variation over a wide range of global locations. A more widespread, semi-independent, validation of secular variation was also able to be made with Swarm satellite-derived geomagnetic virtual observatory data (Hammer et al., 2021), a useful check for regions with limited ground observatory data, such as the Pacific. NCEI and BGS candidate models were then compared to each other, both in the spectral domain (e.g., by directly comparing coefficients) and in the spatial domain (e.g., by plotting maps of model differences for various components). Since both models were derived using slightly different datasets but fully independent methods and algorithms, this provided a semi-independent validation of each model.

The final coefficients for both the WMM and WMMHR were obtained by averaging the NCEI and BGS candidate model coefficients for both the main field and secular variation, and further rounding coefficients to one and four decimal places, respectively. The final models were then validated using the same approach as described above before being approved for public release.

One of the tools used to assess the quality of a model in the spectral space is the so-called Lowes-Mauersberger power spectrum (Mauersberger, 1956; Lowes, 1966), defined as

$$R_n = (n+1)\sum_{m=0}^{n}\left[\left(g_n^m\right)^2 + \left(h_n^m\right)^2\right] \tag{25}$$

$$\dot{R}_n = (n+1)\sum_{m=0}^{n}\left[\left(\dot{g}_n^m\right)^2 + \left(\dot{h}_n^m\right)^2\right]$$

for each degree n of the spherical harmonic expansion, where g_n^m and h_n^m are the main field coefficients, and $\dot{g}_n^m$ and $\dot{h}_n^m$ are the secular variation coefficients (cf. Equation 9). Figure 8 shows the power spectra of the final WMM2025 and WMMHR2025 at the Earth's surface for both the main field and secular variation coefficients on January 1, 2025. As expected, the model power decreases from degree one to 15, reflecting the faster attenuation of smaller spatial scales originating in the core due to the distance from the core to the Earth's surface. The power from degree 16 to 133 slightly increases and then flattens, reflecting the fact that crustal field sources, which dominate in this part of the spectrum, are close to the Earth's surface. The small differences in WMM and WMMHR powers, especially for degrees 11 and 12, are due to the different precisions of their coefficients.

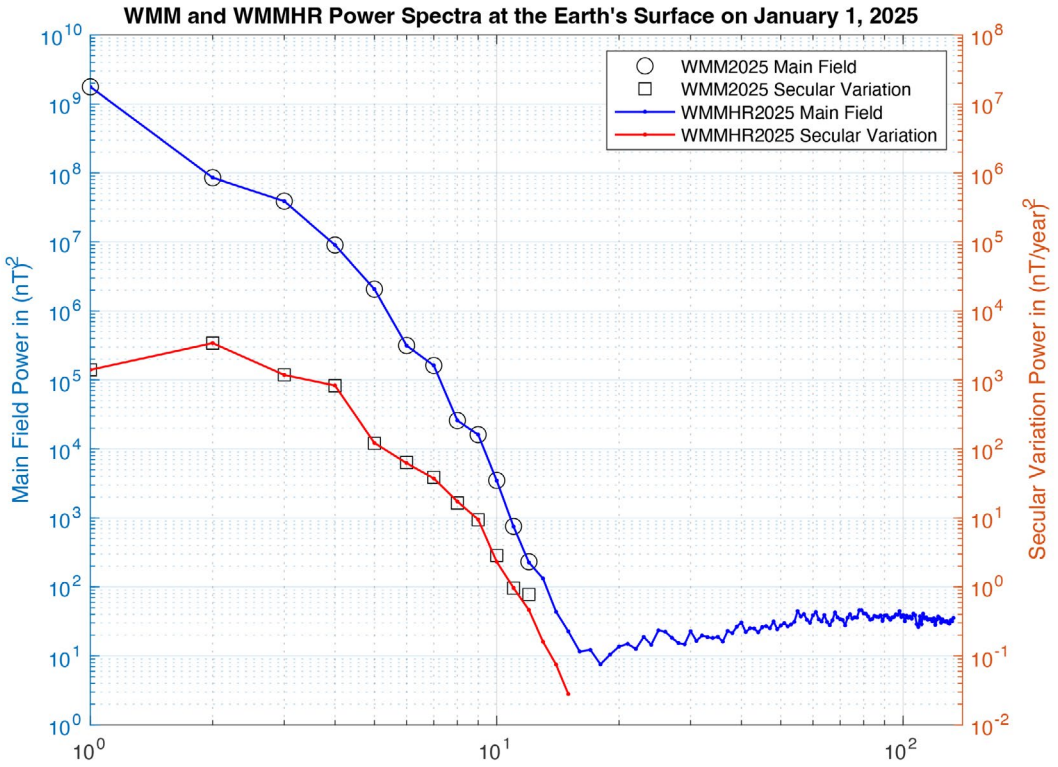

Figure 8: Power spectra of the WMM2025 and WMMHR2025 main field and secular variation at the Earth's surface on January 1, 2025. Degrees one to 15 of the WMMHR2025 model are dominated by sources in the Earth's core, while degrees 16 to 133 are dominated by sources in the Earth's crust.

3. Model uncertainties

The WMM2025 and WMMHR2025 models are valid from January 1, 2025 to December 31, 2029. Like all physical models, they contain uncertainties that must be carefully considered by users. This section discusses the various sources of uncertainty in WMM2025 and WMMHR2025 and quantifies the uncertainties associated with each source at or near the Earth's surface (Sections 3.1–3.4). These uncertainties are then combined into a total error budget, which forms the basis of a simple error model that provides uncertainty estimates for each magnetic field component. This error budget verifies that WMM2025 meets the accuracy requirements of military specification MIL-PRF-89500B (Department of Defense, 2019) and demonstrates that WMMHR2025 exhibits lower uncertainties than WMM2025, as expected for a higher spatial resolution model. (As of now, there is no military specification for WMMHR.)

The WMM error budget is regularly updated throughout the model's period of validity by comparing its predictions with the latest satellite and ground-based observatory data as they become available. Since 2021, NCEI and BGS have published an annual *State of the Geomagnetic Field* report presenting the results of these performance assessments and evaluating whether the WMM continues to meet its military specification throughout its five-year cycle (Chulliat et al., 2021b; NCEI and BGS, 2022, 2023). During the 2020–24 cycle, WMM2020 errors for all magnetic field components were found to remain well below the maximum limits specified by the military standard. Similar annual reports are expected during the upcoming 2025–29 cycle.

For the first time, this report also addresses the vertical validity range of the WMM (Section 3.5). According to the current specification, the WMM is intended to remain valid from 1 km below the WGS 84 ellipsoid surface to at least 850 km above it (Department of Defense, 2019). NCEI recently conducted a critical assessment of this specification using models of the various geomagnetic field sources that influence the WMM error with increasing altitude (Nair et al., in preparation). The results of this study are summarized in Table 17 and could help inform a future revision of the military specification.

3.1 Sources of uncertainty

Apart from human-made disturbances of the measurements, which are not discussed here, there are two primary sources of disagreement between magnetic field observations and the WMM (or WMMHR). The first results from inaccuracies in the model coefficients and is commonly referred to as the *commission error*. The second arises because the WMM (or WMMHR) does not account for all contributions to the observed magnetic field and is often referred to as the *omission error*.

The commission error is the sum of errors due to inaccuracies in main field coefficients, describing the field in 2025.0, and predictive secular variation coefficients, describing the linear part of the field variation from 2025.0 to 2030.0. Since the early 2000s, inaccuracies have been much reduced due to a series of high-precision magnetic survey satellites. However, in the case of the secular variation there is an additional error due to the fact that the true secular variation is not exactly linear. This is because changes of the fluid flow in the Earth's outer core lead to slightly non-linear changes in the Earth's magnetic field. The non-linear part of the secular variation is currently unpredictable, but, fortunately, it is small compared to the linear secular variation. It follows that, by surveying the field for several years, one can precisely map the present field and its rate of change, and then linearly extrapolate the rate out into the future for several years. Provided that suitable satellite magnetic observations are available, the prediction of the WMM is highly accurate on its release date and then subsequently deteriorates towards the end of the 5-year epoch, when it has to be updated with revised values of the model coefficients.

Non-linear core field variations are often related to short-lived, global increases in the power of the second order time derivative of the core field, a phenomenon referred to as a "secular acceleration pulse". Over the past 25 years, high-quality, low-Earth orbit satellite data have provided an increasingly detailed picture of acceleration

pulses (e.g., Chulliat and Maus, 2014; Pavón-Carrasco et al., 2021; Bai et al., 2024). At least six pulses have been detected; these pulses were centered near 2006, 2009, 2012, 2016, 2018, and 2021, and lasted two to three years. They were strongest at mid-to-low latitudes and had spatially and temporally alternating polarity (i.e., for example, a positive secular acceleration in 2006 was followed by a negative one in 2009). At many magnetic observatories, pulses were preceded and/or followed by so-called "geomagnetic jerks", or sudden changes in the secular variation at a given location. Geomagnetic jerks have long been observed and are ubiquitous in observatory data (e.g., Brown et al., 2013). Recent research suggests that acceleration pulses and at least some geomagnetic jerks might be related to hydromagnetic waves in the Earth's core (e.g., Aubert and Finlay, 2019; Gillet et al., 2022). When a large pulse occurs just after the release of the WMM, non-linear core field variations can lead to significant errors in the WMM predictions after a few years. Such was the case during the WMM2015 cycle; the issue was fixed by releasing an out-of-cycle update of the WMM (Chulliat et al., 2019; Chulliat et al., 2021a).

The omission error arises from portions of the geomagnetic field that cannot be described by the WMM (or WMMHR) because either their spatial scale is too small or their time scale is too short. Most of these contributions are generated in the Earth's crust and upper mantle, and in the ionosphere and magnetosphere, whereas the long-wavelength portion of the Earth's magnetic field represented by the WMM originates within the Earth's fluid outer core. The WMMHR includes smaller spatial scales of the Earth's magnetic field compared to the WMM, including the largest scales of the crustal magnetic field (down to approximately 300 km at the equator); however, it doesn't include a large portion of the crustal field, resulting in an omission error due to the crustal field as well. Sources in the crust and upper mantle produce static spatial anomalies, while sources in the ionosphere and magnetosphere produce rapidly varying disturbance fields, either global or regional. The omission error is the largest contributor to the total error (see Section 3.2) and can reach very large values in certain locations and at specific times. For example, differences between the observed declination and the WMM (WMMHR) can exceed 10 degrees. Such large anomalies are uncommon but do exist. Declination anomalies of three or four degrees are not unusual, though they tend to have small spatial or temporal extent.

On land, spatial anomalies are produced by mountain ranges, ore deposits, cloud-to-ground lightning, geological faults, etc. The corresponding deviations are usually smaller at sea, increase with increasing latitude, and decrease with increasing altitude of an air- or spacecraft. In ocean areas these anomalies occur most frequently along continental margins, near seamounts, and near ocean ridges, trenches and fault zones, particularly those of volcanic origin.

Since the crustal field is almost constant in time, it can be inferred from all available satellite, marine and aeromagnetic measurements of the past decades. These data have been compiled into a spherical harmonic degree-790 Enhanced Magnetic Model (EMM). Developed as a research model for the NGA, the EMM2017 provides consistent global representation of the magnetic field, including the crustal field, down to wavelengths of approximately 51 kilometers, for the period from 2000–22. The WMM subroutine library was designed to be compatible with the EMM. The use of the EMM should be considered in applications that require higher demands in pointing accuracy.

3.2 Estimating uncertainty

Various approaches were used to estimate the uncertainty of the WMM2025 and WMMHR2025. Some approaches provide the uncertainties associated with one type of error and/or one omitted source, while others provide combined uncertainties for different sources. It is important to recognize that the omission error, particularly the one associated to the crustal field, dominates over the commission error, and that the omitted sources are only partially sampled in space and time. Therefore, it is not possible to precisely estimate the

WMM2025 uncertainty in every location at the Earth's surface. What is achievable is a global estimate of the uncertainty, based upon a statistical analysis of the differences between the WMM2025 and its predecessors and independent geomagnetic measurements in as many locations as possible on the Earth's surface.

In the previous two WMM technical reports (Chulliat et al., 2015, 2020), formal commission errors for all magnetic field components were estimated by (a) computing the error in the Gauss coefficients from their variance-covariance matrix, and (b) propagating these errors to the magnetic field components. However, errors of this type were found to be extremely small (less than 1 nT) and negligible compared to other sources of error relevant to the WMM and WMMHR, including commission errors obtained from model comparisons. This is because the formal approach does not account for uncertainties associated with how data are selected and corrected prior to inclusion in the parent models, how the parent models are extrapolated forward in time to the WMM epoch, and how NCEI and BGS models are combined. For these reasons, formal commission errors are no longer included in this report.

3.2.1 Commission error from model comparisons

Because BGS and NOAA use different data and modeling approaches, some insight into the errors arising from imperfect modeling and prediction of the core field signal (up to degree 12 in WMM and degree 15 in WMMHR) can be gained by inter-comparing their respective models and by comparing the preliminary and final versions of WMM2025 and WMMHR2025 with WMM2020. These comparisons are performed by computing the magnetic field components on a 1° latitude/longitude grid (defined using geocentric latitude) and calculating root-mean-square (RMS) differences weighted by the cosine of the latitude. The north and south BoZs (as defined in Section 1.8) are excluded from declination and grid variation (north and south) calculations. Table 11 lists these differences and, for reference, also includes similar differences computed between WMM2020 and both WMM2015v1 (the original version of WMM2015, released in December 2014) and WMM2015v2 (the out-of-cycle update; cf. Chulliat et al., 2019).

The RMS differences at epoch 2025.0 between both the preliminary NOAA and BGS WMM models (Table 11, row 1a) and the final NOAA and BGS WMM models (row 4a) are similar to those obtained at epoch 2020.0 during the preparation of WMM2020 (see Table 11 in Chulliat et al., 2020), despite methodological changes by both teams. This consistency suggests that the differences are robust and provide a reliable representation of the actual commission errors. RMS differences at epoch 2025.0 between the preliminary and final NOAA and BGS WMMHR models (rows 1b and 4b) yield nearly identical values (often identical for most components), indicating that increasing the spherical harmonic expansion of the core field from degree 12 to degree 15 does not significantly affect commission errors. However, the WMMHR models (preliminary and final) differ noticeably from the corresponding WMM models (rows 1c–1d and 4c–4d).

At epoch 2030.0, the RMS differences between NOAA and BGS WMM models increase (rows 2a and 5a), as expected, since these differences include not only differences between main fields but also the cumulated effect of secular variation differences over five years. Once again, the corresponding WMMHR model differences (rows 2b and 5b) are nearly identical, suggesting that expanding the secular variation from degree 12 to degree 15 has little impact on commission errors. RMS differences between WMMHR and WMM models at epoch 2030.0 are nearly identical to corresponding differences at 2025.0 (compare rows 2c–2d and 5c–5d with rows 1c–1d and 4c–4d), suggesting that the additional degrees in the spherical harmonic expansion of the secular variation are too small to produce noticeable effects in the model differences.

Note the large GV_N and GV errors at the end of the 2015-2020 interval (row 6c) for the WMM2015v1 model, compared to the corresponding errors for WMM2020 at epoch 2025.0 (row 6a). These errors were related to the fast drift of the north magnetic dip pole during the 2015-2020 cycle and the occurrence of a geomagnetic jerk at the beginning of that period. GV_S errors were much smaller, reflecting the slower drift of the south magnetic dip pole. The detection of these large grid variation errors as part of the regular performance assessment of

WMM2015v1 prompted the development and release of the WMM2015v2 out-of-cycle update. The new model significantly reduced commission errors for all components, including GV_N and GV (row 6d). Note also the significantly larger errors for all components incurred by the WMM after 10 years (rows 7a-7c and 8a-8d).

Table 11: RMS differences at Earth's surface. These approximate the core field contributions to overall errors. Note increase in error if the model is not updated every five years (rows 7 and 8).

Row	Description	Date	X (nT)	Y (nT)	Z (nT)	H (nT)	F (nT)	I (°)	D (°)	GV (°)	GV_N (°)	GV_S (°)
1a	NOAA prelim – BGS prelim	2025.0	3	2	4	3	4	0.00	0.01	0.02	0.02	0.02
1b	NOAA prelim HR – BGS HR prelim	2025.0	3	2	4	3	4	0.00	0.01	0.02	0.03	0.02
1c	NOAA prelim HR – NOAA prelim	2025.0	7	6	10	7	9	0.01	0.03	0.06	0.07	0.04
1d	BGS prelim HR – BGS prelim	2025.0	8	6	10	8	9	0.01	0.03	0.06	0.07	0.04
2a	NOAA prelim – BGS prelim	2030.0	11	8	16	11	16	0.02	0.04	0.08	0.10	0.05
2b	NOAA prelim HR – BGS prelim HR	2030.0	11	8	16	11	16	0.02	0.04	0.08	0.10	0.05
2c	NOAA prelim HR – NOAA prelim	2030.0	7	6	10	7	9	0.01	0.03	0.05	0.06	0.04
2d	BGS prelim HR – BGS prelim	2030.0	8	7	10	8	9	0.01	0.03	0.06	0.07	0.04
3a	WMM2025prelim – WMM2020	2025.0	47	53	85	47	55	0.13	0.14	0.17	0.23	0.08
3b	WMMHR2025prelim – WMM2020	2025.0	47	53	85	48	56	0.13	0.14	0.17	0.22	0.10
3c	WMMHR2025prelim – WMM2025prelim	2025.0	8	6	10	8	9	0.01	0.03	0.06	0.07	0.04
4a	NOAA final – BGS final	2025.0	3	2	4	3	4	0.00	0.01	0.02	0.03	0.02
4b	NOAA final HR – BGS final HR	2025.0	3	2	4	3	4	0.00	0.01	0.02	0.03	0.02
4c	NOAA final HR – NOAA final	2025.0	7	6	10	7	9	0.01	0.03	0.06	0.07	0.04
4d	BGS final HR – BGS final	2025.0	8	6	10	8	9	0.01	0.03	0.06	0.07	0.05
5a	NOAA final – BGS final	2030.0	14	8	19	14	20	0.02	0.04	0.09	0.12	0.04
5b	NOAA final HR – BGS final HR	2030.0	14	8	20	14	20	0.02	0.04	0.09	0.12	0.04
5c	NOAA final HR – NOAA final	2030.0	7	6	10	7	9	0.01	0.03	0.05	0.06	0.04
5d	BGS final HR – BGS final	2030.0	8	7	11	8	9	0.01	0.03	0.06	0.07	0.04
6a	WMM2025 –WMM2020	2025.0	46	53	85	47	55	0.13	0.14	0.17	0.23	0.08
6b	WMMHR2025 –WMM2020	2025.0	47	53	86	48	56	0.13	0.14	0.17	0.22	0.10
6c	WMM2020-WMM2015v1	2020.0	46	56	89	47	67	0.12	0.22	0.41	0.56	0.16
6d	WMM2020-WMM2015v2	2020.0	9	15	21	9	11	0.03	0.04	0.06	0.07	0.04
6e	WMMHR2025 –WMM2025	2025.0	8	6	10	8	9	0.01	0.03	0.06	0.07	0.04
7a	WMM2025 – WMM2020	2030.0	112	135	211	114	130	0.31	0.34	0.42	0.56	0.19
7b	WMMHR2025 – WMM2020	2030.0	112	135	211	114	131	0.31	0.34	0.41	0.55	0.21
7c	WMMHR2025 – WMM2025	2030.0	8	7	11	8	10	0.01	0.03	0.06	0.07	0.05
8a	WMM2025 –WMM2015v1	2025.0	106	127	201	109	147	0.27	0.48	0.84	1.14	0.37
8b	WMM2025 –WMM2015v2	2025.0	50	66	102	49	63	0.15	0.19	0.22	0.26	0.18
8c	WMMHR2025 –WMM2015v1	2025.0	106	127	202	109	147	0.27	0.48	0.84	1.14	0.37
8d	WMMHR2025 –WMM2015v2	2025.0	50	66	102	49	64	0.15	0.19	0.21	0.25	0.17

The differences between WMM2020 and WMM2025 (and WMMHR2025) predictions for the magnetic field at 2025.0 are shown in Figure 9. The spatial distribution of differences is not necessarily an indication of where the largest errors will occur in the future. However, the largest errors in declination and grid variation will again be concentrated near the magnetic poles where the strength of the horizontal component of the field is lowest.

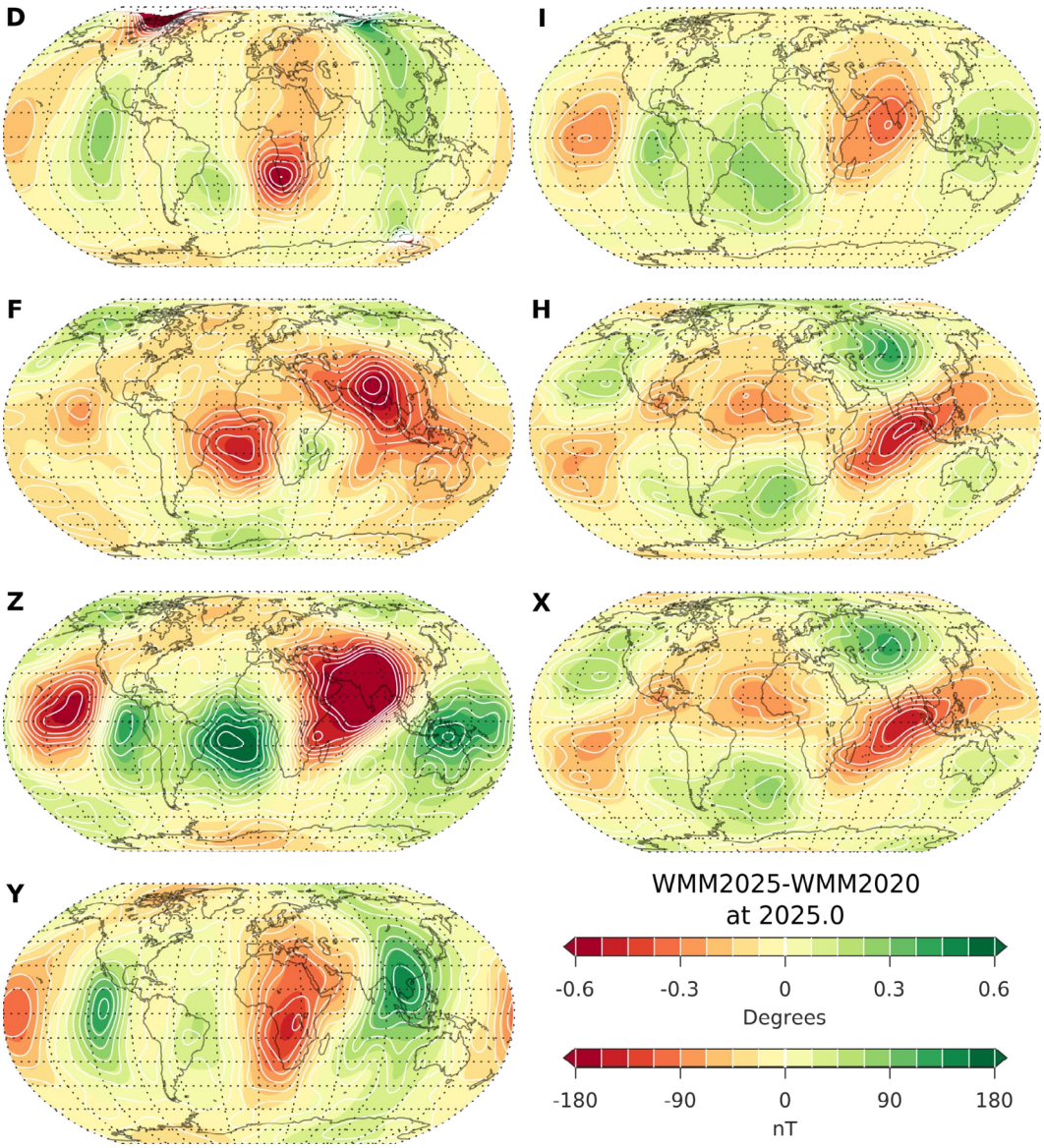

Figure 9: Differences between WMM2025 (WMMHR2025) and WMM2020 at mean Earth radius, at 2025.0. BoZ is shown as light grey areas around dip poles in the declination map. Colored contours depict WMM2025 values, white contours depict WMMHR2025 values.

To further demonstrate the difficulty in modelling declination near the magnetic poles the differences in declination between the two parent models from BGS and NOAA, truncated at degree 12, at 2020.0 and 2025.0 are shown in Figures 10 and 11.

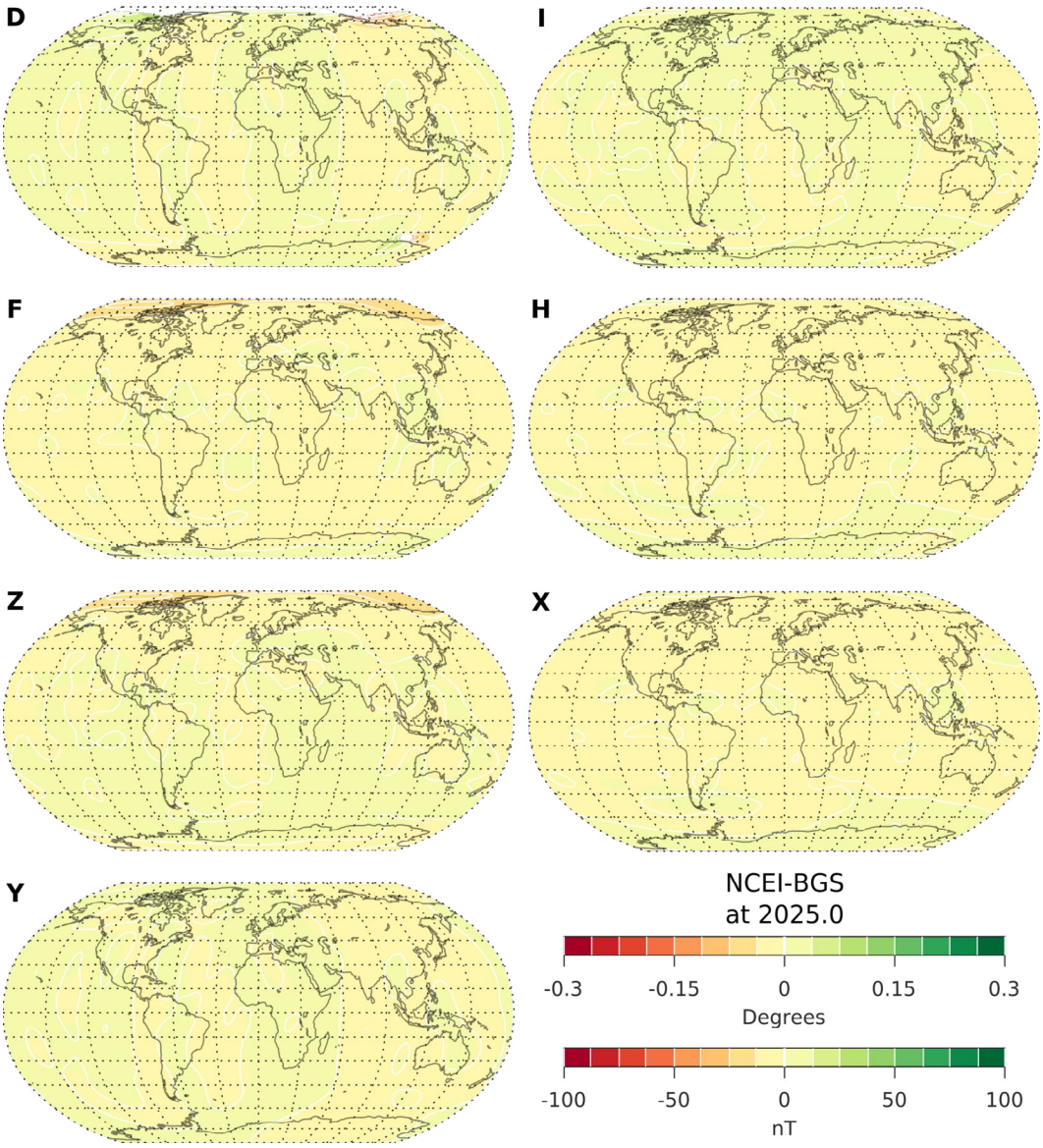

Figure 10: Differences between BGS and NCEI final main field models at mean Earth's radius, at 2025.0. BoZ is shown as light grey areas around dip poles in the declination map. Colored contours depict standard resolution model values, white contours depict high resolution model values.

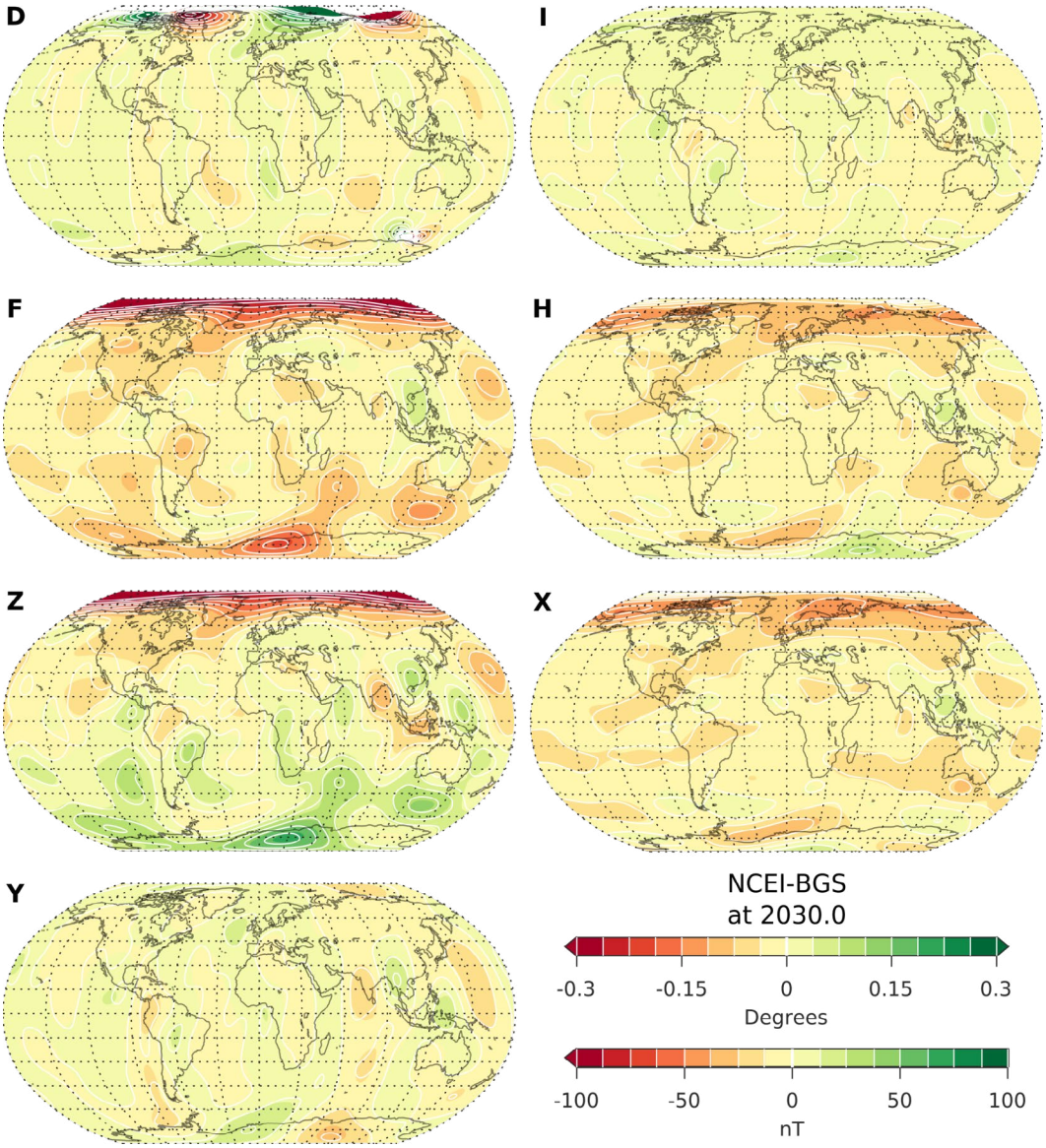

Figure 11: Differences between BGS and NCEI final main field models at mean Earth's radius, at 2030.0. BoZ is shown as light grey areas around dip poles in the declination map. Colored contours depict standard resolution model values, white contours depict high resolution model values.

3.2.2 Crustal field contribution – method #1

The crustal field is the largest source of uncertainty in the WMM near Earth's surface. Although high-resolution crustal field models (such as the EMM) exist, they capture only the largest spatial scales of the crustal field. As a result, any rigorous attempt to quantify the crustal field's contribution to the omission error must rely on actual field measurements.

The first method used to estimate crustal field error involved comparing past WMM predictions with two datasets: (a) trackline data from aeromagnetic and marine surveys archived in NCEI's GEODAS (GEOphysical DAta System) and collected over 2000-2018; and (b) data from 162 geomagnetic observatories archived at BGS's World Data Centre for Geomagnetism in Edinburgh and collected over 2000-2020. Both datasets represent updates and extensions of those used in the WMM2020 Technical Report and are applied here to both the standard WMM and the new high-resolution WMMHR.

Since WMMHR2025 is the inaugural version of WMMHR, a retrospective series of WMMHR models was constructed to cover the period 2000-2020. These models were produced at epochs 2000, 2002.5, 2005, 2007.5, 2010, 2012.5, 2015, 2017.5, and 2020, using core field modeling techniques similar to those employed in the WMM. Magnetic field measurements were obtained from multiple satellite missions, including CHAMP (2000–10), Ørsted (1999–2013), and Swarm (2013-present). More information on the CHAMP and Ørsted missions is available in the WMM2015 Technical Report. To minimize contamination from external magnetic fields, data selection criteria similar to those described in Sections 2.3.1 and 2.3.2 were applied. Contributions from the large-scale lithospheric field (MF7) and the magnetospheric field (CHAOS-7) were subtracted from the data to isolate the core field signal. For each epoch, data from a three-year window ending two months prior were used, mimicking the standard WMM production approach. The core field, including the main field, secular variation, and secular acceleration, was modeled using spherical harmonics up to degree and order 15 and a quadratic time polynomial for each Gauss coefficient, which was then extrapolated to the model epoch. Due to the limited availability of satellite data prior to 2000, a shorter time window and linear time parameterization were used for the 2000.0 epoch. Details of the model inversion procedure, including data weighting and regularization strategies, are provided in Alken et al., (2020). Finally, the time-varying core field coefficients (degrees one–15) were combined with the static crustal field coefficients (degrees 16–133) from the MF7 model to produce WMMHR models consistent with WMMHR2025.

Magnetic trackline data (primarily from marine and aeromagnetic surveys) provide extensive spatial coverage, especially over oceanic regions. The NCEI GEODAS dataset used for this analysis spans the period 2000–18 and includes 24,770,926 total field (F) measurements distributed over a wide range of latitudes and longitudes (see Figure 12). This represents a substantial extension of the error analysis presented in the WMM2020 Technical Report, which was based on 6,857,662 data points collected over the 2000–14 time interval.

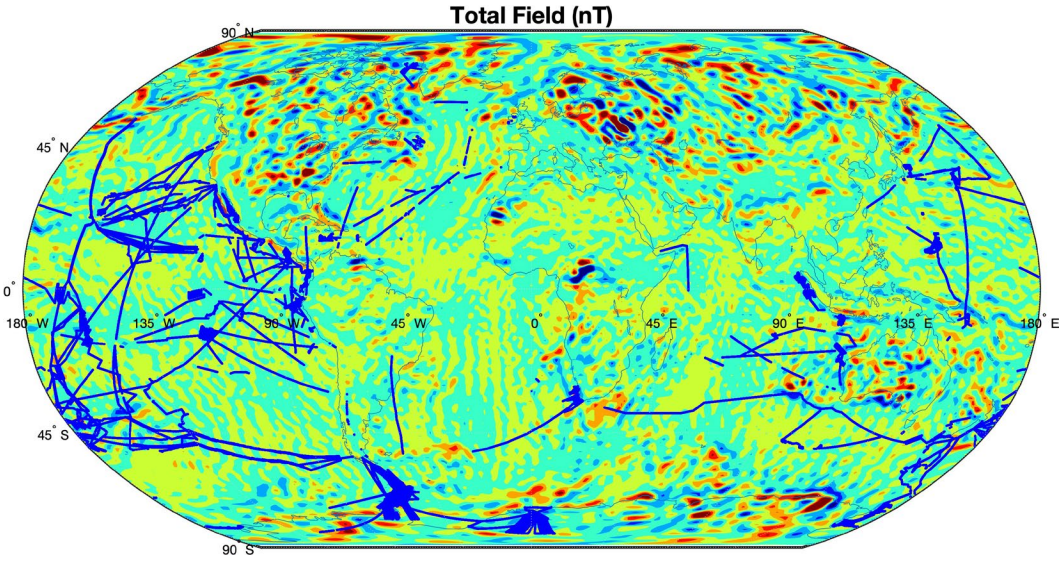

Figure 12: Locations of magnetic trackline data used to estimate crustal field errors. The base map shows the total field (F) derived from the WMMHR crustal field model.

In the first phase of the analysis, residuals between the trackline measurements and model predictions were computed for both WMM and WMMHR models. For WMMHR, two cases were considered: models produced every two and a half years (referred to hereafter as WMMHR-2.5yr) and models produced every five years (referred to hereafter as WMMHR-5yr). For benchmarking purposes, residuals were also computed for the High-Definition Geomagnetic Model 2023 (HDGM2023; Nair et al., 2021), the International Geomagnetic Reference

Field 13th Generation (IGRF-13; Alken et al., 2021), and the Enhanced Magnetic Model 2017 (EMM2017; https://www.ncei.noaa.gov/products/enhanced-magnetic-model). Residuals were binned by absolute magnetic apex latitude (e.g., Laundal and Richmond, 2020), and RMS residuals were then computed for each bin using robust statistical methods to reduce the influence of outliers. These RMS values represent the combined effect of commission errors (e.g., secular variation forecast errors) and omission errors (crustal and external field contributions).

As expected, the WMMHR models have consistently lower RMS residuals than the WMM, due to their higher spatial resolution (Figure 13); however, there is no significant difference between WMMHR-5yr and WMMHR-2.5yr. The EMM2017 and HDGM2023, which have even higher spatial resolution, exhibit significantly lower RMS residuals at all latitudes. The IGRF-13 also outperforms the WMM because it was retrospectively updated for epochs prior to 2020; however, its forward-looking portion is not expected to outperform the WMM. For all models, a clear latitude dependency is observed, with higher residuals at higher latitudes due to stronger crustal and external magnetic fields. A similar trend was observed in the WMM-only error analysis from the WMM2020 Technical Report, which used a smaller trackline dataset, although slightly higher RMS values were observed at high latitudes. To minimize contamination from external magnetic fields, the analysis is restricted to data within the 10° to 50° absolute geomagnetic latitude range. Within this range, average trackline RMS residuals (F component) are: 122 nT for WMM, 114 nT for WMMHR-5yr, and 111 nT for WMMHR-2.5 yr.

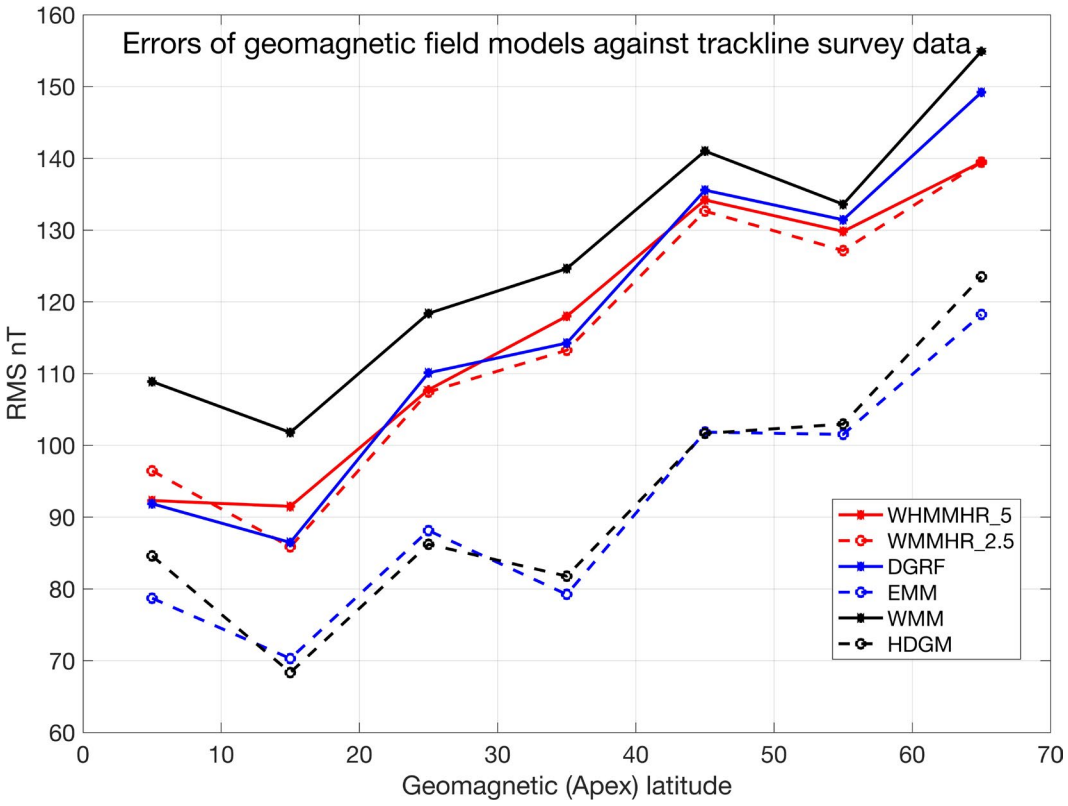

Figure 13: RMS residuals between model predictions and trackline total field (F) measurements, sorted into 10° bins of absolute geomagnetic apex latitudes. "WMMHR_5" refers to "WMMHR-5yr", "WMMHR_2.5" to "WMMHR-2.5yr", and DGRF to the retrospectively updated portion of IGRF-13.

In the second phase of the analysis, hourly mean values from 162 magnetic observatories over 2000–20 were processed. Data were filtered for low geomagnetic activity (ap ≤ 10) and nighttime local times (00:00–04:00 LT), and subsequently least-square fitted with cubic splines, with knots every year. This procedure removes most external field contributions, which typically vary on timescales shorter than one year, except for smaller

external fields varying with the 11-year solar cycle. As a result, each spline fit represents the combined core and crustal fields at the observatory location. RMS differences between the spline fits and WMM predictions were then computed for each component, using 10º bins of absolute geomagnetic latitude. Initial RMS errors for the F component at observatories were found to be much larger than those from trackline data (e.g., 316 nT vs. 122 nT for WMM within the 10°–50° absolute geomagnetic latitude range), primarily due to strong local crustal anomalies near some observatories. To address this, an outlier detection algorithm was applied to select a subset of observatories (between 125 and 127 out of 162 globally) for each model (WMM, WMMHR-2.5yr, WMMHR-5yr), such that the resulting RMS error in F within the 10°–50° latitude range matched the corresponding trackline RMS error for that model. This calibration yielded RMS error estimates for all vector components based on observatory data, anchored to the trackline-derived F error level.

Results are presented in Table 12. In line with the F residuals discussed above, and as expected for higher-resolution models, the RMS residuals for components other than F are generally smaller for the WMMHR models compared to WMM (rows 1a–1c and 2a–2c). A few exceptions suggest that the improvements may be more subtle for some components and that the observatory dataset is not sufficiently extensive to fully capture the benefits of increased spatial resolution.

To separate error contributions from the crustal field and the secular variation, RMS differences between spline fits and WMM predictions were calculated for the first day of each model epoch, and the same set of observatories selected for the full 2000–20 interval. The results represent crustal field-only error values and are presented in Table 12 (rows 3). Corresponding secular variation error values (rows 4) were obtained by subtracting the crustal error (rows 2) from the total error (rows 2) in quadrature.

Note that grid variation north (GV_N) and south (GV_S) are not separated in Table 12 as (a) the dominant source of error is the unmodeled crustal field which is assumed to be of the same order of magnitude in both hemispheres, and (b) there was not enough data to robustly separate GV_N and GV_S. Observatories in the north and south BoZs (as defined in Section 1.8) were excluded from this analysis.

Table 12: RMS differences between observatory data and model predictions (WMM, WMMHR-5r and WMMHR-2.5yr) for the period 2000–20. Rows 1a–1c and 2a–2c report RMS values over the full 2000-2020 interval. Rows 3a–3c show RMS values computed on the first day of model epochs (2000.0, 2005.0, 2010.0 and 2020.0 for WMM and WMMHR-5yr, and every 2.5 years for WMMHR-2.5yr), using a subset of observatories such that the RMS error in F matches that from trackline data within the 10°–50° geomagnetic latitude (MLat) range. Rows 4a–4c provide the estimated secular variation error, obtained by subtracting rows 3a-3c from rows 2a–2c in quadrature. For each case, the total number of observatories (N_obs_all) and the number of selected observatories (N_obs_sel) are provided.

Row	Description	N_obs_sel /N_obs all	X (nT)	Y (nT)	Z (nT)	H (nT)	F (nT)	I (°)	D (°)	GV (°)
1a	Crustal field and secular variation; 10°–50° MLat; WMM	78/105	147	65	136	147	122	0.20	0.15	0.71
1b	Crustal field and secular variation; 10°–50° MLat; WMMHR–5yr	81/105	133	57	141	132	113	0.20	0.14	0.67
1c	Crustal field and secular variation; 10°–50° MLat; WMMHR-2.5yr	81/105	138	54	133	137	110	0.20	0.13	0.66
2a	Crustal field and secular variation; all latitudes; WMM	126/162	144	86	139	144	127	0.19	0.33	0.71
2b	Crustal field and secular variation; all latitudes; WMMHR–5yr	127/162	132	82	133	131	117	0.18	0.35	0.67
2c	Crustal field and secular variation; all latitudes; WMMHR–2.5yr	125/162	136	73	126	135	111	0.18	0.30	0.66
3a	Crustal field only; all latitudes; WMM	126/162	139	80	130	139	120	0.18	0.32	0.68
3b	Crustal field only; all latitudes; WMMHR–5yr	127/162	136	79	122	136	112	0.18	0.34	0.64
3c	Crustal field only; all latitudes; WMMHR–2.5yr	125/162	137	72	123	135	109	0.18	0.29	0.64
4a	Inferred secular variation; all latitudes; WMM	N/A	38	32	49	38	42	0.06	0.08	0.20
4b	Inferred secular variation; all latitudes; WMMHR–5yr	N/A	30	22	53	20	34	0.00	0.08	0.20
4c	Inferred secular variation; all latitudes; WMMHR–2.5yr	N/A	0	12	27	0	21	0.00	0.08	0.16

3.2.3 Crustal field contribution – method #2

World Magnetic Models since 2000 (representing those produced during the era of higher resolution data from magnetic satellite surveys) were compared with compilations of ground-based vector data. Each of the five models comprises main-field coefficients at a base epoch and predictive secular variation coefficients valid for the following five years. Two data compilations were used in the comparison: (1) repeat station and land survey data and (2) observatory annual means. Both compilations are from the World Data Centre for Geomagnetism (Edinburgh) and have only modest contamination from external fields, as data are mostly reduced to quiet night time or annual mean equivalents in (1) and annual averaging smooths out much of the unwanted signal in (2). Choosing to quantify crustal omission from the limited number of repeat station data (see Figure 14 for data locations through time) available since 2000 was to allow consistency between uncertainty models for WMM and WMMHR models, as HR models of the core field cannot accurately be calculated prior to the satellite era. Crustal uncertainty is thus potentially lower due to the accuracy of modern measurement and models but may be less representative of under sampled regions.

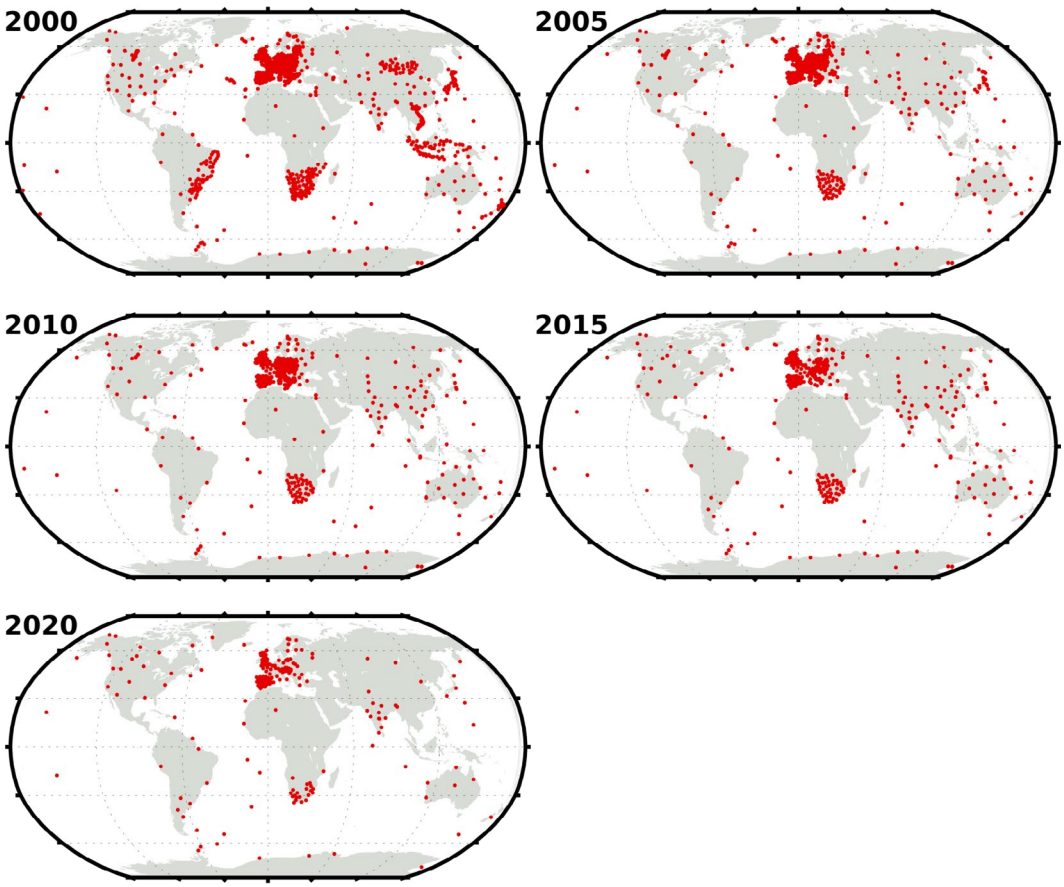

Figure 14: The locations of repeat stations, vector land surveys and observatories that provided data for model comparisons (crustal field contribution, method #2). Maps show locations of data in the five-year WMM period from each date shown.

RMS differences were computed for all seven elements, and for each of the five models after elimination of outliers (any differences greater than three standard deviations). The sample sizes vary according to the element but are greater than 1500. Table 13 (row 1) lists these RMS differences. Note that there was not enough data to robustly separate grid variation north (GV_N) and south (GV_S) in this analysis. Also, no data were used in the north and south BoZs (as defined in Section 1.8). In an approach similar to that used in Section 3.2.2, RMS differences were calculated on the first year of each model epoch to determine the contribution to the error

from the crustal field only. The results are reported in Table 13 (row 2). Subtraction of the values estimated for the first year of each model epoch from those for the full model period gives an inferred estimate of the contribution from secular variation (Table 13, row 3).

The contribution to the overall error budget for the WMM from the crustal field estimated here using vector data collected on land is conservative, i.e. over-cautious. One way of justifying the use of lower values is to employ near-surface scalar data, i.e., total intensity. These data are plentiful as they are relatively easy to collect from ships and aircraft and, importantly, they cover both land and sea. Global scalar anomaly compilations have been made in recent years, for example the World Digital Magnetic Anomaly Map (WDMAM, Lesur et al., 2016) and NOAA's Earth Magnetic Anomaly Grids EMAG2 (Maus et al., 2009) and EMAG2v3 (Meyer et al., 2017). The mean absolute differences for F derived from the land-based vector observations can be compared with those from global compilations. For WDMAM (version 2) the mean absolute anomaly in F is 107 nT, for EMAG2 it is 105 nT and for EMAG2v3 it is 83 nT. These are likely to be underestimated at the Earth's surface because these compilations are above the surface at 5 km and 4 km, respectively. However, even if these were to be downward-continued to the Earth's surface they would not be as high as the value from the repeat stations and observatories (195 nT). Another source of scalar data is NOAA's GEODAS (GEOphysical DAta System), as described in Section 3.2.2. For 2000 onwards, the spatial distribution of these data is not as good as that of the WDMAM and EMAG2, but they are collected at the Earth's surface.

Following the same approach as in the WMM2020 Technical Report, the values from the repeat stations and observatories are scaled according to the mean of the RMS difference from EMAG2 and the GEODAS surveys (121 nT) and are shown in Table 13 (row 4).

Table 13: RMS differences between observations and models in World Magnetic Model series since 2000, using all data (row 1) or only data collected in the same year as the model epoch (row 2). Row 3 is calculated as row 2 subtracted from row 1 in quadrature. Row 4 is obtained by rescaling row 2 values so that the RMS difference on the F component is equal to 121 nT (all components are rescaled using the same ratio).

Row	Description	X (nT)	Y (nT)	Z (nT)	H (nT)	F (nT)	I (°)	D (°)	GV (°)
1	Crustal field and secular variation; repeat stations and observatory annual means; 2000 to 2025	181	142	205	165	208	0.22	0.47	0.80
2	Crustal field only; repeat stations and observatory annual means; 2000 to 2025, first year of each epoch only	172	131	192	153	195	0.21	0.43	0.70
3	Inferred secular variation; repeat stations and observatory annual means; 2000 to 2025	56	55	72	62	72	0.07	0.19	0.39
4	Rescaled crustal field (row 2), according to information from EMAG2_v3 and GEODAS	107	81	119	95	121	0.13	0.27	0.43

3.2.4 Crustal field contribution – method #3

A third method, closely resembling Method #2, was used to estimate crustal field errors in WMMHR-5yr and WMMHR-2.5yr, as well as in WMM. This approach relied on the same retrospective series of WMMHR models described in Section 3.2.2, in addition to the older WMM models. For all three models, predictions were compared to a total of 3,094 repeat station vector data collected between 2000 and 2017 during geomagnetically quiet periods (Figure 15).

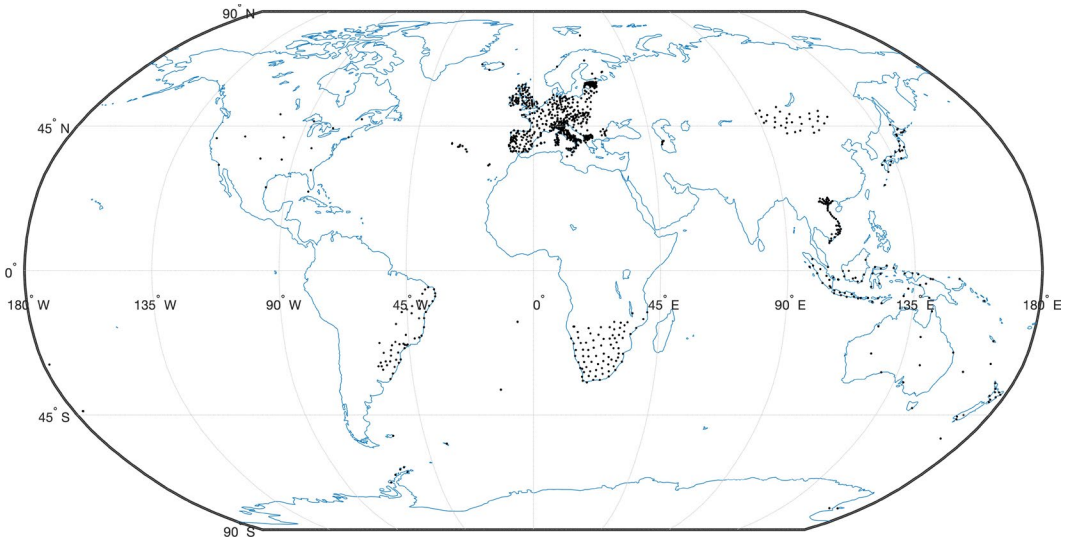

Figure 15: The locations of repeat stations that provided data for model comparisons (crustal field contribution, method #3). Maps show locations of data in the 2000–17 time interval used in the analysis.

The resulting RMS residuals were significantly larger than the trackline errors reported in Section 3.2.2, primarily due to the closer proximity of repeat station measurements to crustal sources compared to marine and airborne trackline data. To account for this, the residuals were re-scaled relative to the model-specific trackline RMS error in the F component (see Section 3.2.2 for values). The final values (Table 14) represent an estimate of crustal field errors over continental areas, calibrated to the trackline error level.

Table 14: RMS differences between repeat station observations and models in WMM, WMMHR-5yr and WMMHR-2.5yr over 2000–17, before (rows 1a–1c) and after (rows 2a–2c) re-scaling relative to the trackline RMS F errors.

Row	Description	X (nT)	Y (nT)	Z (nT)	H (nT)	F (nT)	I (°)	D (°)	GV (°)
1a	Repeat station errors, WMM	156	99	177	153	217	0.27	0.36	0.60
1b	Repeat station errors, WMMHR–5yr	146	98	174	147	216	0.27	0.36	0.56
1c	Repeat station errors, WMMHR–2.5yr	146	98	169	147	212	0.27	0.36	0.56
2a	Re-scaled repeat station errors, WMM	125	69	120	125	120	0.20	0.24	0.40
2b	Re-scaled repeat station errors, WMMHR–5yr	115	67	112	115	112	0.18	0.23	0.36
2c	Re-scaled repeat station errors, WMMHR–2.5yr	109	60	104	109	109	0.17	0.21	0.35

3.2.5 Disturbance field contribution

The disturbance field is the sum of the contributions of ionospheric and magnetospheric electric currents, as well as currents induced in the Earth and oceans by these time-varying external magnetic fields. The strength of the disturbance field is modulated by the 11-year solar cycle. Periods of strong magnetic activity, such as geomagnetic storms, occur primarily around solar maximum, although the most intense storms often occur one to two years after the peak. The epoch of WMM2025 (and WMMHR2025) begins near the peak of Solar Cycle 25 and extends into its descending phase (Figure 16).

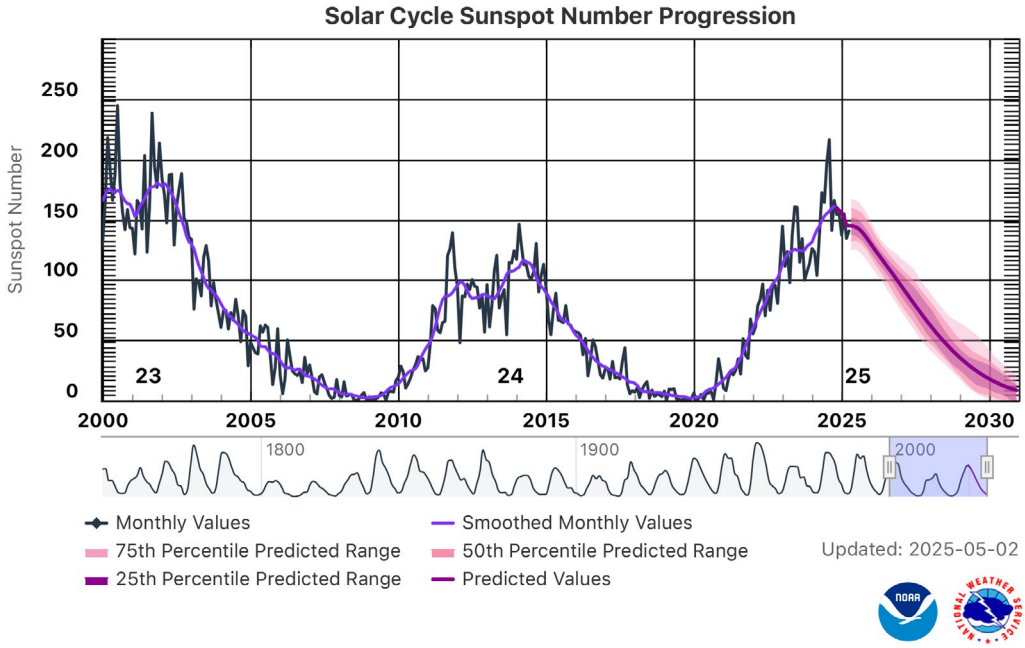

Figure 16: Observed and predicted solar cycle since 2000. The black line represents the monthly average sunspot number, and the purple line represents a 13-month weighted, smoothed version of the monthly averaged data. The forecast for the current solar cycle is represented by the magenta line. This forecast comes from the Solar Cycle Prediction Panel representing NOAA, NASA, and the International Space Environmental Services (ISES). (Image provided by the NOAA Space Weather Prediction Center based on the 2019 expert panel prediction updated in May 2025.)

Large storms have already occurred during the ascending phase of Solar Cycle 25, which coincided with the 2020–24 period of WMM2020. Notably, an extreme G5-class storm (as classified by NOAA's Space Weather Prediction Center) occurred on May 10–11, 2024. In addition, several severe (G4) storms have been recorded since 2020: one in 2021, two in 2023, four in 2024 and two already in 2025 as of May. These G4 caused significant but temporary impacts on WMM performance, primarily at high geomagnetic latitudes, with declination deviations exceeding 9 degrees in some regions (NCEI and BGS, 2022, 2023).

The contribution from the disturbance field to the WMM uncertainty was estimated in the WMM2020 Technical Report from hourly mean values recorded at 175 magnetic observatories over 2000–18 (see Section 3.2.2). RMS residuals between the data and the cubic spline fit over 2000–18 were calculated for each observatory and each component. The obtained variation with latitude (Figure 17) is in good agreement with the known properties of the external field. Near the geomagnetic equator, the northern external field is enhanced by the so-called equatorial electrojet, a strong electrical current flowing at 110 km altitude along the geomagnetic dip equator. At higher latitudes, near 65° geomagnetic latitude, intense auroral electrojets can lead to variations as large as several thousands of nT during geomagnetic storms. However, on average, the contribution of the external field to the total error is much smaller than that of the crustal field and for this reason its latitude dependency is neglected in what follows.

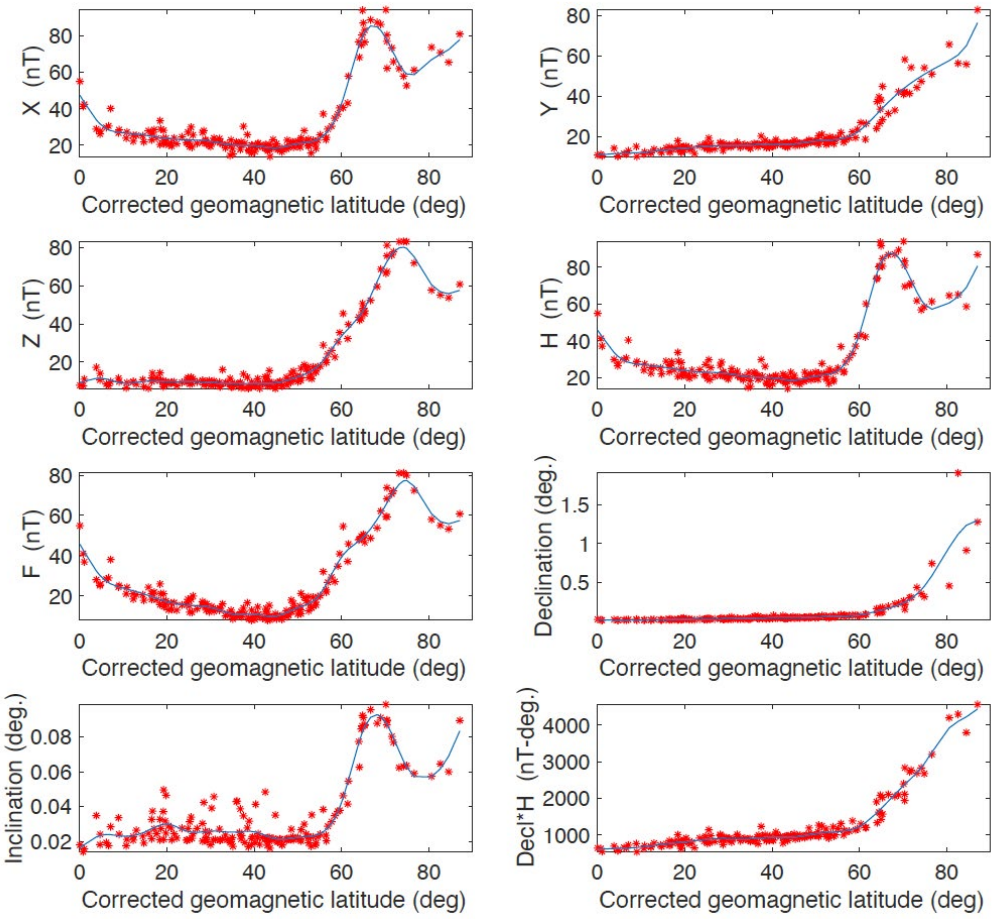

Figure 17: Variation with corrected geomagnetic latitude of the RMS residuals between observatory data and spline fits for the various field components and for the years 2000–18.

The global RMS error values for each component are provided in Table 15. These values also apply to WMMHR, as neither WMM nor WMMHR accounts for the external magnetic fields.

Table 15: RMS residuals, attributed to the external field, between observatory data and spline fits for each component and for the years 2000–18.

Row	Description	X (nT)	Y (nT)	Z (nT)	H (nT)	F (nT)	I (°)	D (°)	GV (°)
1	RMS external field contribution from 175 observatories at all latitudes	37	23	27	37	29	0.04	0.22	0.44

3.3 Total error budget

The results of the error analysis for WMM2025 and WMMHR2025 are summarized in Table 16:

- Estimates of the commission errors at 2025.0 (Table 16, rows 2a and 2b) are derived by calculating the RMS differences between the final NOAA and BGS WMM and WMMHR models for that epoch (Table 11, rows 4a and 4b, respectively).
- The commission error at 2025.0 (Table 16, row 3), dominated by the secular variation forecasting error over the next five years and assumed to be identical for WMM and WMMHR, is calculated by averaging the RMS differences between WMM2025 and WMM2020 at 2025.0 (Table 11, row 6a), and the RMS differences between WMM2020 and WMM2015v1 at 2020.0 (Table 11, row 6c). These values represent the true secular variation forecasting errors over the past two WMM cycles for each component.

- The three methods used to estimate the crustal field contribution have complementary merits and limitations. To obtain the final estimate of the crustal field omission error for WMM2025 (Table 16, row 4a), the results from method #1 (Table 12, row 3a) were averaged with the averages of the results from methods #2 (Table 13, row 4) and #3 (Table 14, row 2a). For WMMHR2025, the results from method #1 (Table 12, row 3b) were averaged with those from method #3 (Table 14, row 2b).
- The disturbance field omission error (Table 16, row 5) is the one reported in Table 15.

Since these errors are statistically independent, the expected total WMM2025 errors at 2025.0 (Table 16, row 6a) and 2030.0 (row 7a) are calculated as the root-sum-square (RSS) of the values in rows 2a, 4a, and 5, and rows 3, 4a, and 5, respectively. For WMMHR2025, the total errors at 2025.0 (row 6b) and 2030.0 (row 7b) are calculated in the same way, using rows 2b, 4b, and 5, and rows 3, 4b, and 5, respectively. For example, the total WMM2025 error at epoch 2025.0 for the modeled declination is estimated as:

$$\sqrt{0.01^2 + 0.29^2 + 0.22^2} = 0.36^\circ \tag{26}$$

Note that all error values increase between 2025 and 2030 due to the accumulation of secular variation forecasting error over the WMM validity period. The largest relative increase is observed for GV_N, which is associated with the rapid drift of the north magnetic dip pole, as discussed in Section 3.2.2.

Table 16: Estimated global RMS errors in WMM2025 and WMMHR2025. Higher values of GV (compared to D) reflect the larger uncertainties of the declination at high latitudes, the only regions where GV is defined. Higher values of GV_N compared to GV_S reflect the faster drift of the north dip pole compared to the south dip pole. Military specification values for H, F, I, D, GV_N, and GV_S are taken from the current version, MIL-PRF-89500B. Values for X, Y, and Z are taken from the previous version, MIL-PRF-89500A; these are marked with an asterisk and are not required under the current specification.

Row	Description	X (nT)	Y (nT)	Z (nT)	H (nT)	F (nT)	I (°)	D (°)	GV (°)	GV_N (°)	GV_S (°)
1	Military specification MIL-W-89500B	140*	140*	200*	200	280	1.00	1.00	N/A	1.00	1.00
2a	Commission error at 2025.0 – WMM2025	3	2	4	3	4	0.00	0.01	0.02	0.03	0.02
2b	Commission error at 2025.0 – WMMHR2025	3	2	4	3	4	0.00	0.01	0.02	0.03	0.02
3	Commission error at 2030.0 – all models	46	55	87	47	61	0.13	0.18	0.29	0.40	0.12
4a	Crustal field omission error – WMM2025	127	78	125	124	120	0.17	0.29	0.55	0.55	0.55
4b	Crustal field omission error – WMMHR2025	126	73	117	126	112	0.18	0.29	0.50	0.50	0.50
5	Disturbance field omission error – all models	37	23	27	37	29	0.04	0.22	0.44	0.44	0.44
6a	Combined error at 2025.0 – WMM2025	133	81	128	130	124	0.18	0.36	0.70	0.70	0.70
6b	Combined error at 2025.0 – WMMHR2025	131	77	120	131	116	0.18	0.36	0.67	0.67	0.67
7a	Combined error at 2030.0 – WMM2025	140	98	154	138	138	0.22	0.40	0.76	0.81	0.71
7b	Combined error at 2030.0 – WMMHR2025	139	94	148	139	131	0.22	0.40	0.73	0.77	0.68

The accuracy requirements for the WMM are detailed in the military specification MIL-PRF-89500B (Department of Defense, 2019) and are provided in row 1 of Table 16. In summary, the requirement is that the global RMS difference between the WMM and the observed magnetic field on the WGS 84 ellipsoid surface should be within 1° for D, I, GV_N and GV_S, within 200 nT for H and within 280 nT for F for the entire 5-year lifetime of the model. [Table 16 also includes specification values from the previous version, MIL-PRF-80500A (Department

of Defense, 2015), for X, Y, Z. These are provided for reference only and are not required under the current specification]. We find that the combined error values for WMM2025 (rows 6a and 7a) are all lower than the required values. During the WMM cycle, NCEI and BGS regularly update the combined error estimates using the most recent available data to ensure that the model remains within specification. The results of this performance assessment are published annually (e.g., NCEI and BGS, 2023).

For most components, the combined errors at epochs 2025.0 and 2030.0 are lower for WMMHR2025 than for WMM2025, as expected due to the higher spatial resolution of WMMHR2025. However, for three components, the combined errors are either slightly larger (H) in WMMHR2025 or identical (I and D) in both models. The 1 nT difference observed for H is likely insignificant and can reasonably be disregarded. This observation underscores a limitation of the uncertainty analysis, which treats errors as global averages. Much larger differences between WMM2025 and WMMHR2025 errors are expected in regions with strong crustal magnetic field anomalies, as such anomalies are better captured in the crustal field portion of WMMHR2025, as shown in Figure 12. For this reason, the use of WMMHR2025 over WMM2025 is recommended whenever possible.

3.4 Error models

The WMM2025 and WMMHR2025 each come with an error model that provides uncertainty estimates for every geomagnetic element (X, Y, Z, H, F, I and D) at every location on the WGS 84 ellipsoid surface. These models are based on the results of the error analysis (see Section 3.3) and incorporate the geometrical relationships between the various components [formulas (19) in Section 1.2].

The first part of each error model was constructed by averaging rows 6a and 7a (for WMM2025) or rows 6b and 7b (for WMMHR2025) in Table 16, treating the results as the variances of the X, Y and Z components, and assuming that the off-diagonal terms of the variance-covariance matrix for (X, Y, Z) are zero. The resulting error values are:

$$\delta X_{\mathrm{WMM2025}} = 137 \text{ nT} \tag{27}$$

$$\delta Y_{\mathrm{WMM2025}} = 89 \text{ nT} \tag{28}$$

$$\delta X_{\mathrm{WMM2025}} = 141 \text{ nT} \tag{29}$$

and

$$\delta X_{\mathrm{WMMHR2025}} = 135 \text{ nT} \tag{30}$$

$$\delta Y_{\mathrm{WMMHR2025}} = 85 \text{ nT} \tag{31}$$

$$\delta Z_{\mathrm{WMMHR2025}} = 134 \text{ nT} \tag{32}$$

The errors in (X, Y, Z) were then propagated to (F, I, D, H) by linearizing the relationships between these components, as given by equations (19), and by neglecting the off-diagonal terms of the variance-covariance matrix:

$$\delta H = \sqrt{\left[(\delta X)^2(\cos D)^2 + (\delta Y)^2(\sin D)^2\right]} \tag{33}$$

$$H\,\delta D = \sqrt{\left[(\delta X)^2(\sin D)^2 + (\delta Y)^2(\cos D)^2\right]} \tag{34}$$

$$\delta F = \sqrt{\left[(\delta H)^2(\cos I)^2 + (\delta Z)^2(\sin I)^2\right]} \tag{35}$$

$$F\,\delta I = \sqrt{\left[(\delta H)^2(\sin I)^2 + (\delta Z)^2(\cos I)^2\right]} \tag{36}$$

To remove non-physical variations in δH, δF and δI, these quantities were averaged over the WGS 84 ellipsoid, yielding the following results:

$$\delta H_{\mathrm{WMM2025}} = 133\ \mathrm{nT} \tag{37}$$

$$\delta F_{\mathrm{WMM2025}} = 138\ \mathrm{nT} \tag{38}$$

$$\delta I_{\mathrm{WMM2025}} = 0.20^{\circ} \tag{39}$$

and

$$\delta H_{\mathrm{WMMHR2025}} = 130\ \mathrm{nT} \tag{40}$$

$$\delta F_{\mathrm{WMMHR2025}} = 134\ \mathrm{nT} \tag{41}$$

$$\delta I_{\mathrm{WMMHR2025}} = 0.19^{\circ} \tag{42}$$

As expected, these values closely match those in the error budget (Table 16), indicating that the error analysis is internally consistent.

The case of δD is different, as the horizontal intensity H approaches zero near the North and South magnetic poles, causing δD to approach infinity in those regions. As a result, using a global average for δD would seriously underestimate the declination error near the poles. (In Sections 3.2 and 3.3, the effect of the geometrical divergence of δD on error calculations was mitigated by excluding data from the northern and southern BoZs.) To address this issue, the following formulas were developed:

$$\delta D_{\mathrm{WMM2025}} = \sqrt{(0.26)^2 + (5417/H)^2} \tag{43}$$

and

$$\delta D_{\mathrm{WMMHR2025}} = \sqrt{(0.25)^2 + (5205/H)^2} \tag{44}$$

where δD is expressed in degrees and H in nanoteslas (nT). These formulas are constructed such that:

(1) At low latitudes (i.e., where the horizontal intensity H is large), δD is close to the propagated δD averaged over all locations where $H \geq 5000$ nT (i.e., excluding regions where δD becomes very large due to the geometrical effect). This average is approximately 0.29° for WMM2025 and 0.28° for WMMHR2025. Specifically, the constant 0.26° in the WMM2025 formula is derived from $\sqrt{(0.29)^2 - (5417/41875)^2}$, so that δD = 0.29° where H = 41875 nT, the maximum value of H at the Earth's surface in WMM2025. Similarly, the constant 0.25° in the WMMHR2025 formula is derived from $\sqrt{(0.28)^2 - (5205/41896)^2}$, so that δD = 0.28° where H = 41896 nT, the maximum value of H at the Earth's surface in WMMHR2025.

(2) Near the poles (i.e., where H is small), δD behaves like the global average of the propagated $H\,\delta D$, which is approximately 5417 nT for WMM2025 and 5205 nT for WMMHR2025, divided by H.

Global maps of the corresponding declination errors are shown in Figure 18. At mid- to low-latitudes, the errors remain close to (or slightly below) the averages of the 2025.0 and 2030.0 error budget values (for both models; see Table 16, rows 6a–6b and 7a–7b). The errors increase near the magnetic dip poles and in a region near South Africa where the horizontal field is weak. The globally averaged declination errors computed from equations (43) and (44) are 0.41° for WMM2025 and 0.39° for WMMHR2025, both of which are consistent with the error budget values.

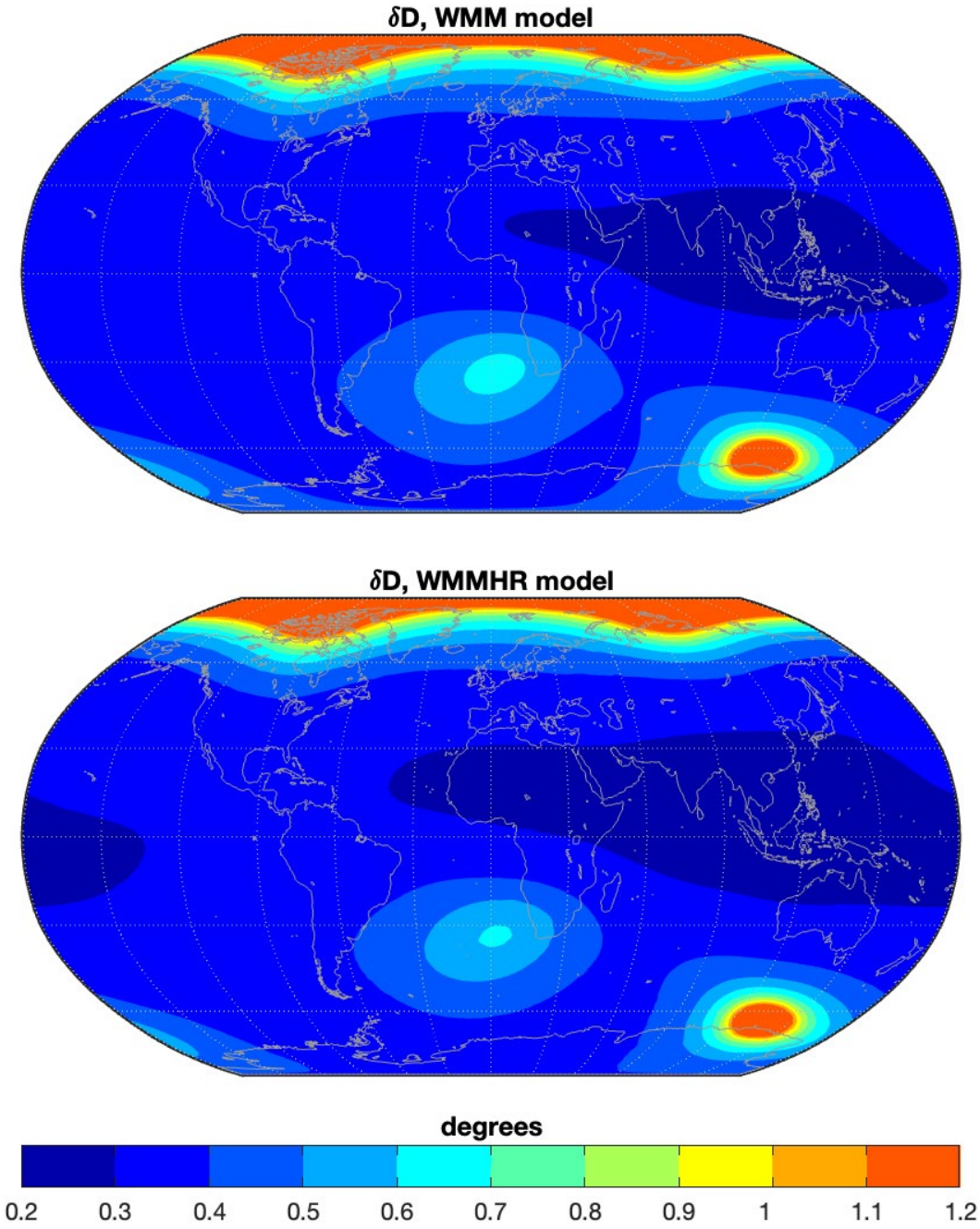

Figure 18: Global distribution of the declination error provided by the WMM2025 (top) and WMMHR2025 (bottom) error models. The color scale is limited to a maximum value of 1.2°; the error becomes larger than this near magnetic poles.

The final error models are thus made of equations (27)-(29), (37)-(39) and (43) for WMM2025, and of equations (30)–(32), (40)–(42) and (44) for WMMHR2025. The uncertainties in X, Y, Z, H, F and I are assumed to be constant over the globe, while the uncertainty in D is assumed to vary with location.

3.5 Vertical validity range

While the WMM specification requires the model to be valid up to 850 km above the ellipsoid, the WMM and similar main field models are generally believed to remain valid at much higher altitudes, potentially extending far into space. However, WMM errors relative to the total magnetic field magnitude are expected to increase with altitude. This is because the Earth's core field weakens with distance, while external magnetic fields (which

are not modeled by WMM) become stronger near electric currents in the ionosphere and magnetosphere. The intensity of these currents varies rapidly with geomagnetic activity, which is driven by the solar wind, making error estimation at high altitudes particularly challenging.

In a recent study, Nair et al. (in preparation) investigated WMM errors at various altitudes using a combination of geomagnetic and magnetospheric models, as well as satellite magnetic field measurements. Table 17 summarizes the findings of this study regarding the vertical validity range of the WMM. These results are also applicable to the WMMHR, as both the crustal field portion of the WMMHR and the additional three spherical harmonic degrees in its core field component (compared to the WMM) decay rapidly with altitude and therefore do not affect the model's vertical validity. In Table 17, the geomagnetic activity is quantified using NOAA's Space Weather Prediction Center Geomagnetic Storms Scale. WMM errors are evaluated relative to the military specification values, taken from the current version, MIL-PRF-89500B (Department of Defense, 2019), for H, F, I, D, GV_N, and GV_S, and from the previous version, MIL-PRF-89500A (Department of Defense, 2015), for X, Y and Z, using the main field magnitude as the reference. Specifically, the model is considered to breach the military specification for a given component if the ratio of the error to the main field magnitude at a given altitude exceeds the ratio of the military specification value to the main field magnitude at the Earth's surface for that component. In some cases, particularly during strong and severe magnetic storms, the model is not valid at any altitude for certain components. During extreme (G5-class) storms, use of the model is not advised at any altitude for any component.

This study doesn't address the related question of the model's validity below the Earth's surface. However, over the oceans, the WMM is expected to meet the military specification down to 1 km below the sea surface. Over the continents, the validity is region-specific, depending on the strength and depth of local crustal magnetic field anomalies. For such applications, it is recommended to use a higher-resolution model that incorporates information about these anomalies rather than relying on the WMM.

Table 17: Vertical validity ranges (expressed in km, Height Above the Ellipsoid) of WMM and WMMHR for various components and levels of geomagnetic activity. The military specification (Milspec) values are taken from the current version, MIL-PRF-89500B (for H, F, I, D, GV_N, and GV_S), and from the previous version, MIL-PRF-89500A (for X, Y, and Z). "*Exceeds*" indicates that the models are not valid at any altitude for that component and activity level. An asterisk ("*") denotes that the models may be valid above this height, but this could not be confirmed through testing. "*Not advised*" indicates that use of the models is not advised at any altitude due to extreme geomagnetic activity.

Component (Milspec)	Altitude Ranges for G0 Activity	Altitude Ranges for G1 Activity	Altitude Ranges for G2 Activity	Altitude Ranges for G3 Activity	Altitude Ranges for G4 Activity	Altitude Ranges for G5 Activity
X (140 nT)	0 to 2,200	0 to 1,000	Exceeds	Exceeds	Exceeds	Not advised
Y (140 nT)	0 to 2,200	0 to 2,000	0 to 1,800	0 to 1,600	0 to 1,100	Not advised
Z (200 nT)	0 to 1,900	0 to 1,500	0 to 1,200	0 to 1,200	0 to 1,200	Not advised
H (200 nT)	0 to 3,200	0 to 1,900	0 to 1,200	0 to 1,100	0 to 800	Not advised
F (280 nT)	0 to 3,500	0 to 2,500	0 to 1,900	0 to 1,900	0 to 1,900	Not advised
I (1°)	0 to 10,000*	0 to 9,500	0 to 7,800	0 to 7,700	0 to 7,300	Not advised
D (1°)	0 to 6,000*	0 to 6,000*	0 to 6,000*	0 to 6,000*	0 to 6,000*	Not advised
GV_N (1°)	0 to 5,000*	0 to 5,000*	0 to 3,800	Exceeds	Exceeds	Not advised
GV_S (1°)	0 to 4,000*	0 to 4,000*	0 to 3,800	0 to 2,200	0 to 300	Not advised

4. Charts

This section provides the WMM2025 charts in the following order:

- Main field maps for 2025.0 in Miller projection for X, Y, Z, H, F, I and D (see pgs. 66–69).
- Main field maps in North Polar stereographic projection (see pgs. 70–76).
- Main field maps in South Polar stereographic projection (see pgs. 77–83).
- Secular variation maps for 2025.0 – 2030.0 in Miller Projection for X, Y, Z, H, F, I, and D (see pgs. 84–87).
- Secular variation maps in North Polar stereographic projection (see pgs. 88–94).
- Secular variation maps in South Polar stereographic projection (see pgs. 95–101).
- Grid variation maps in polar stereographic projection (see pgs. 102–105).
- Geomagnetic dipole longitude and latitude in Miller projection (see pg. 106).

The white stars on the maps indicate the 2025.0 positions of the dip poles. The 2025.0 blackout (resp. caution) zones are shown as dark (resp. light) shaded areas.

Main field maps: Miller projection

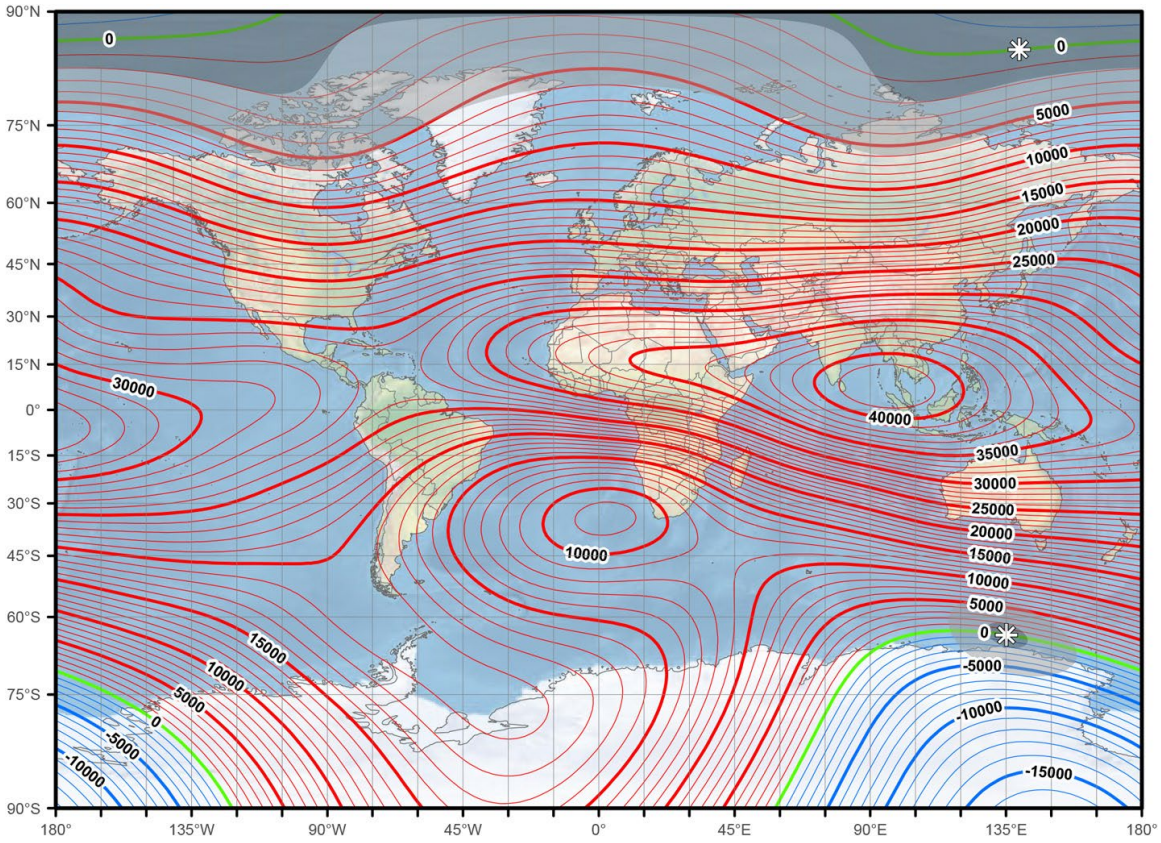

Main field north component (X). The contour interval is 1000 nT. Miller projection.

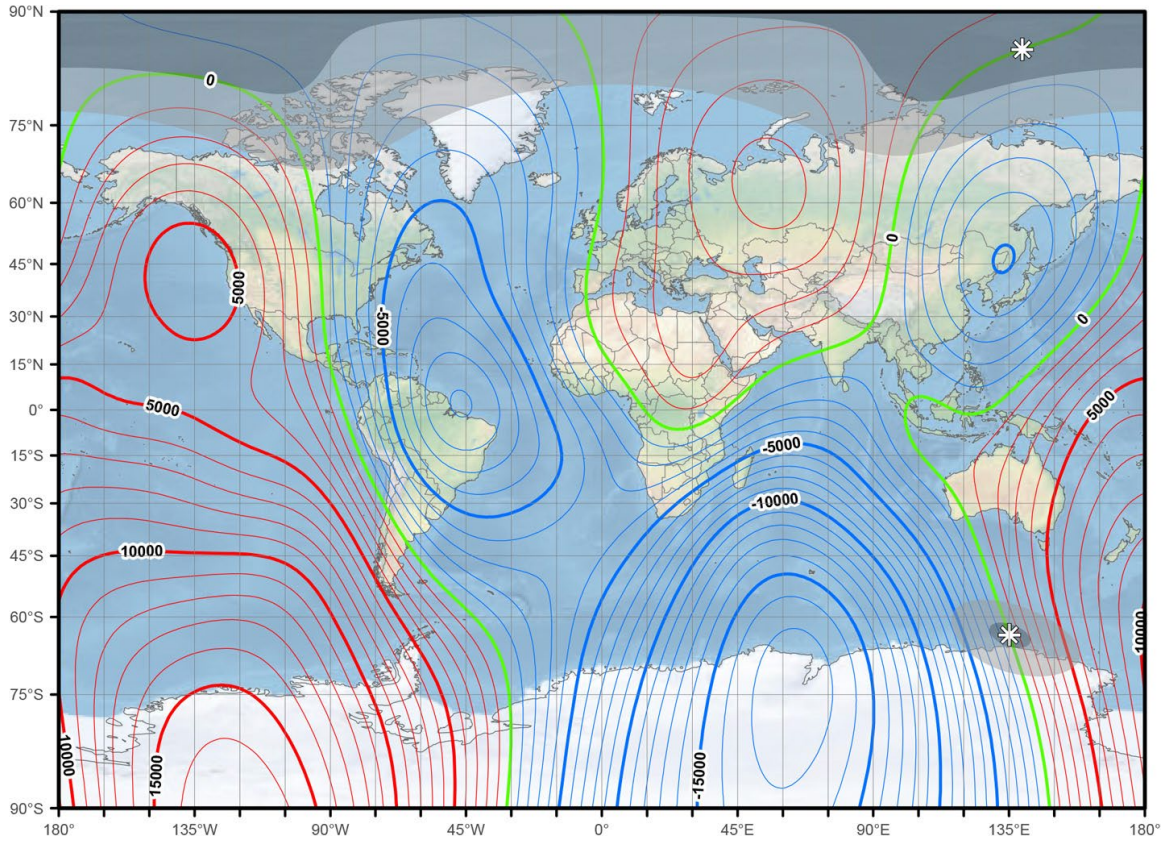

Main field east component (Y). The contour interval is 1000 nT, red contours positive (east); blue negative (west); green zero line. Miller projection.

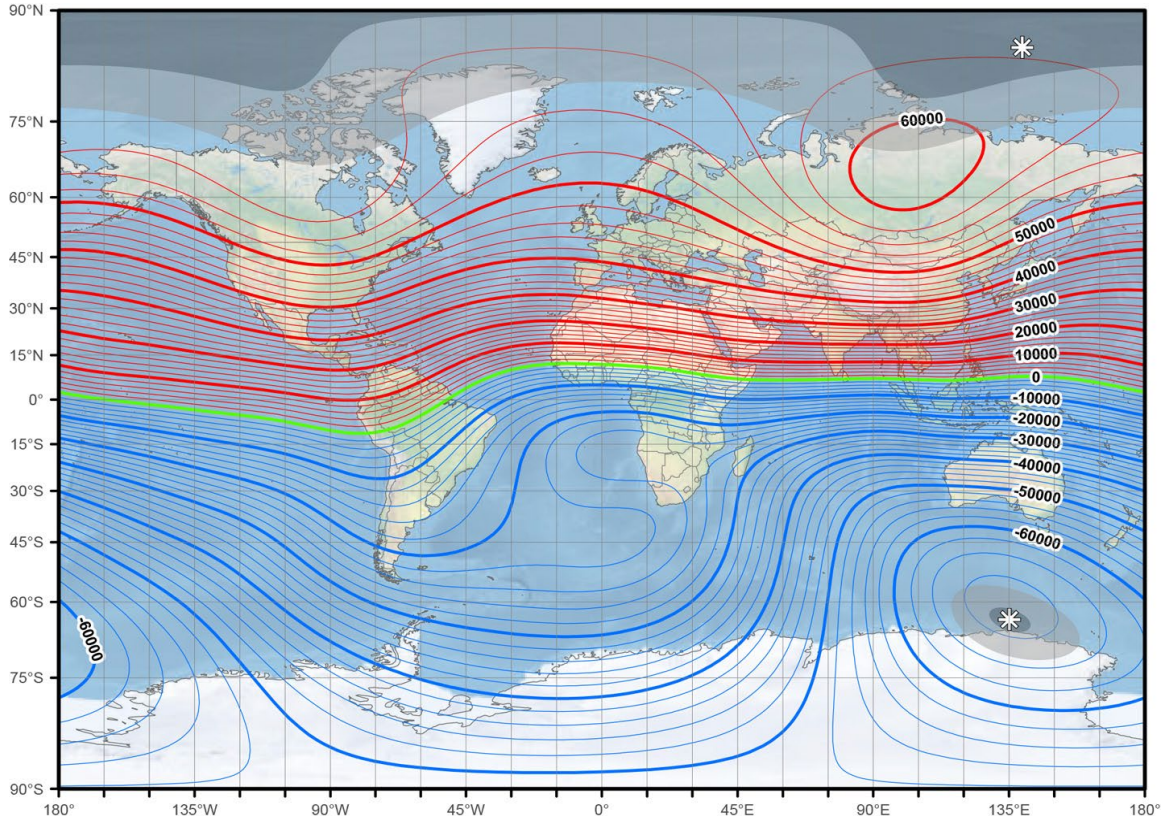

Main field down component (Z). The contour interval is 1000 nT, red contours positive (down); blue negative (up); green zero line. Miller projection.

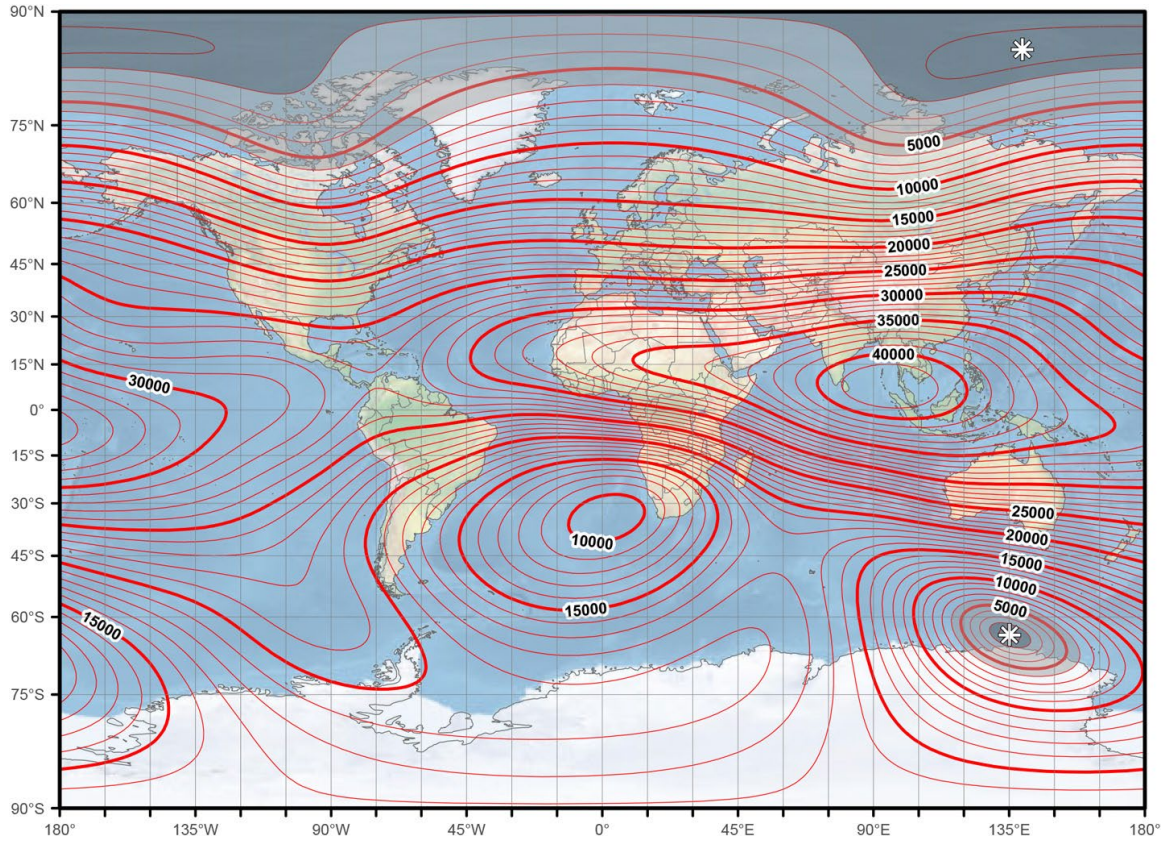

Main field horizontal intensity (H). The contour interval is 1000 nT. Miller projection.

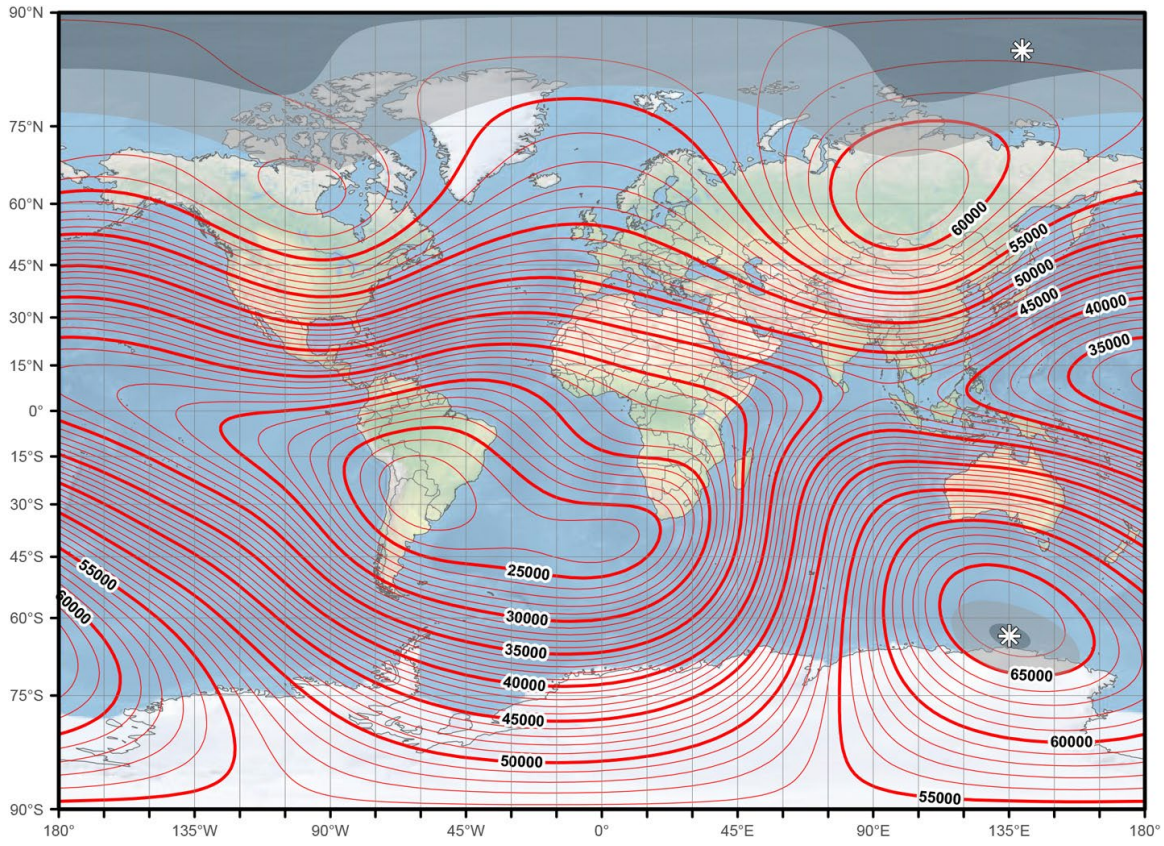

Main field total intensity (F). The contour interval is 1000 nT. Miller projection.

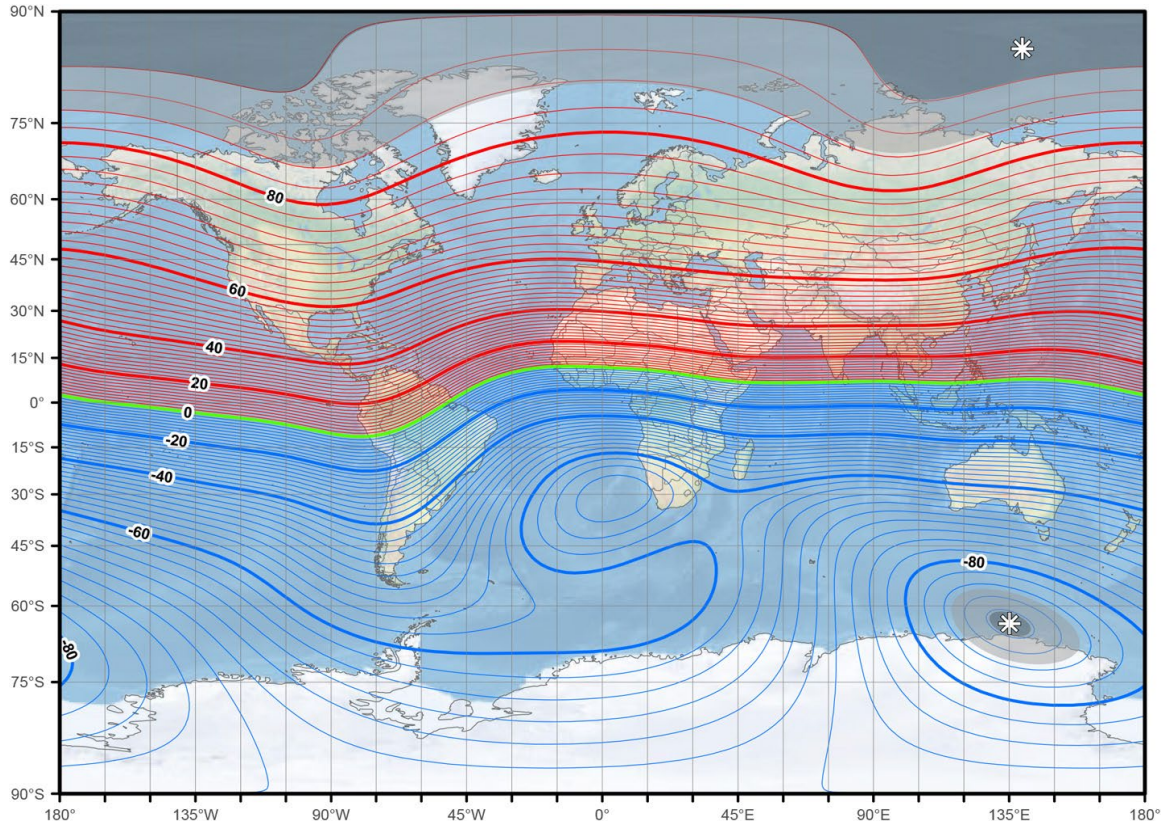

Main field inclination (I). The contour interval is 2 degrees, red contours positive (down); blue negative (up); green zero line. Miller projection.

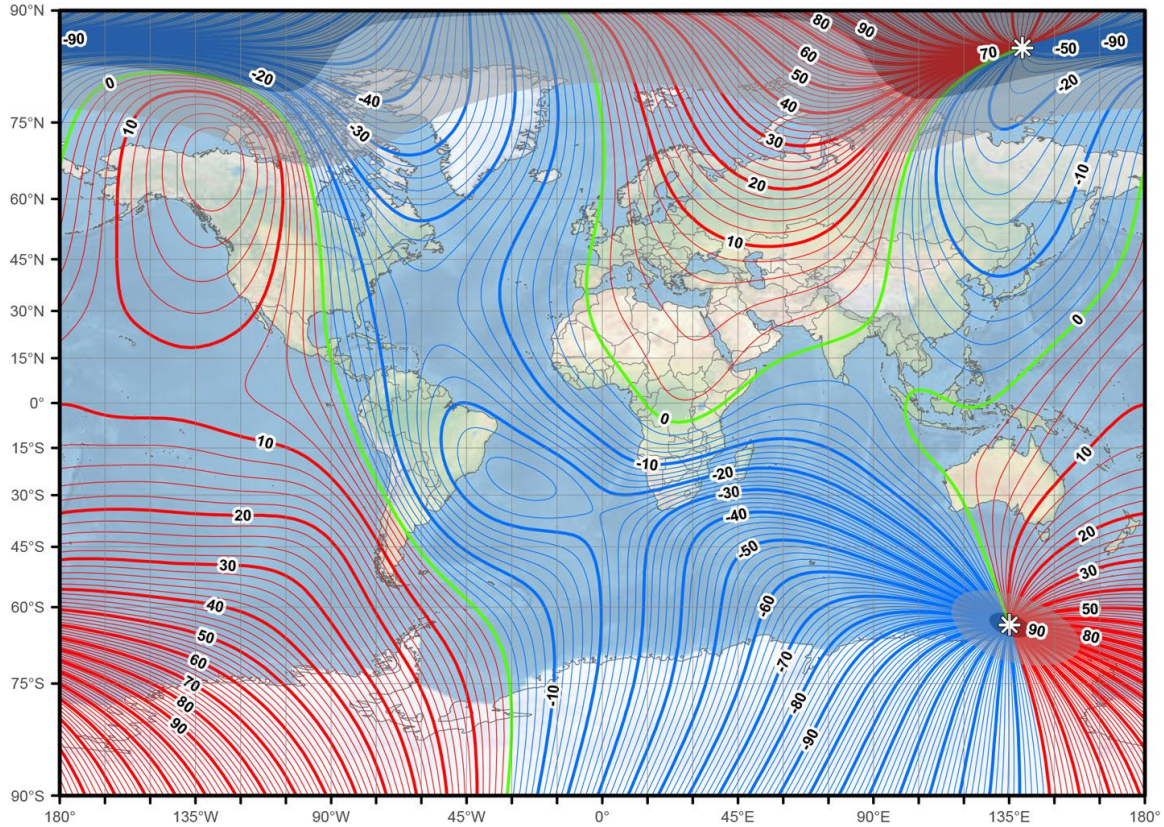

Main field declination (D). The contour interval is two degrees, red contours positive (east); blue negative (west); green zero (agonic) line. Miller projection.

Main field maps: North Polar stereographic projection

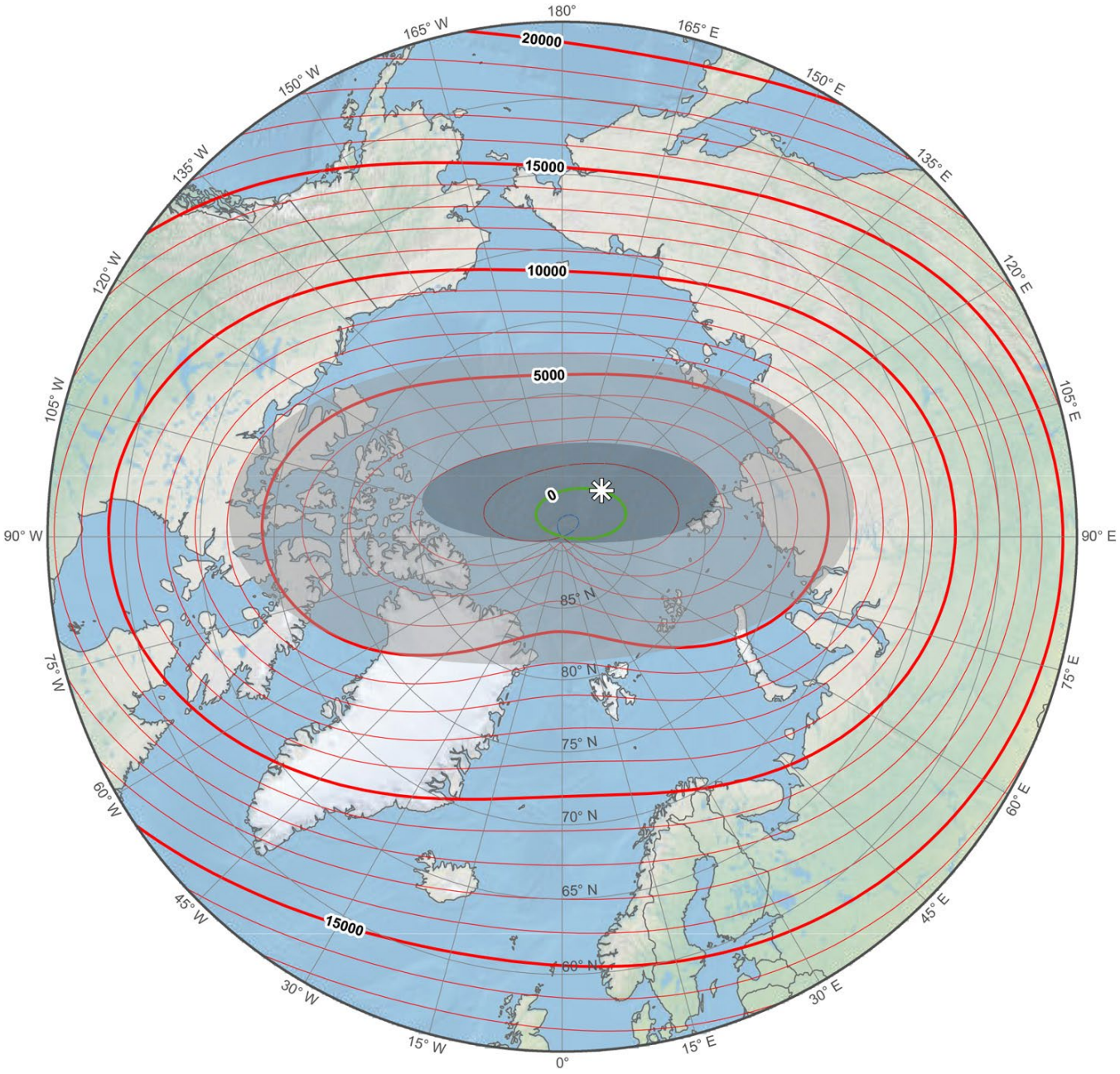

Main field north component (X). The contour interval is 1000 nT. North Polar Region. Polar stereographic projection.

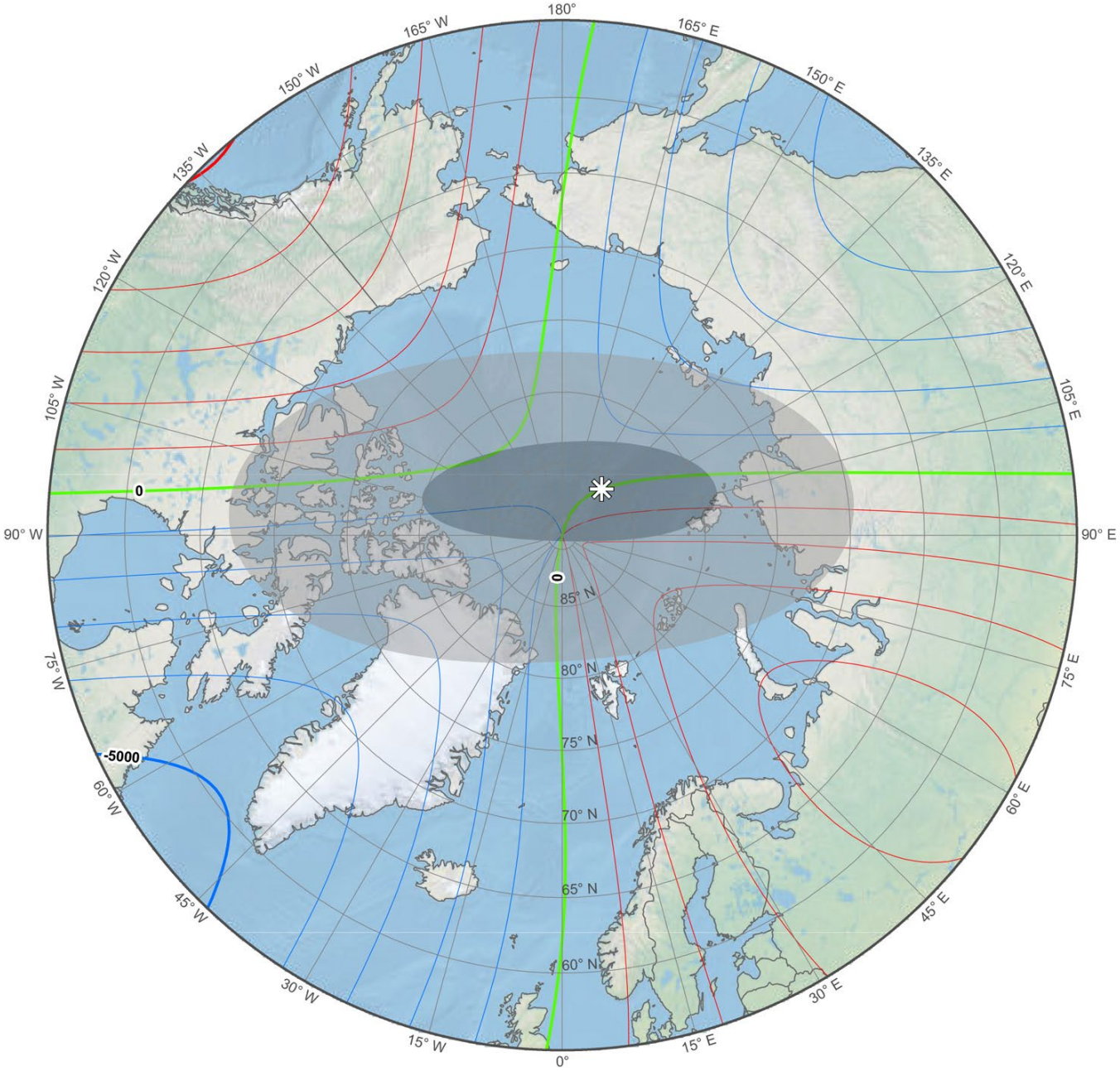

Main field east component (Y). The contour interval is 1000 nT, red contours positive (east); blue negative (west); green zero line. North Polar Region. Polar stereographic projection.

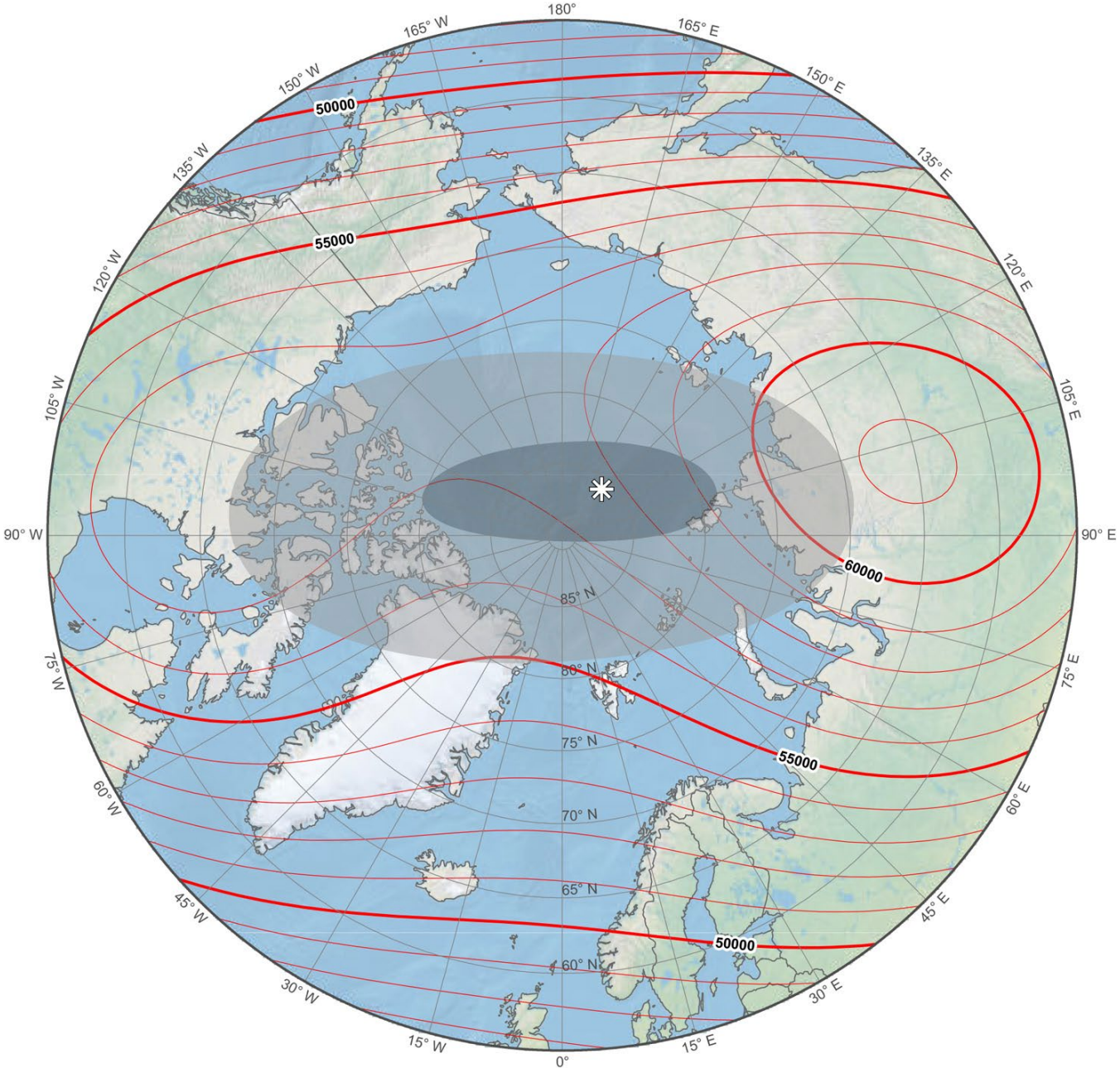

Main field down component (Z). The contour interval is 1000 nT. North Polar Region. Polar stereographic projection.

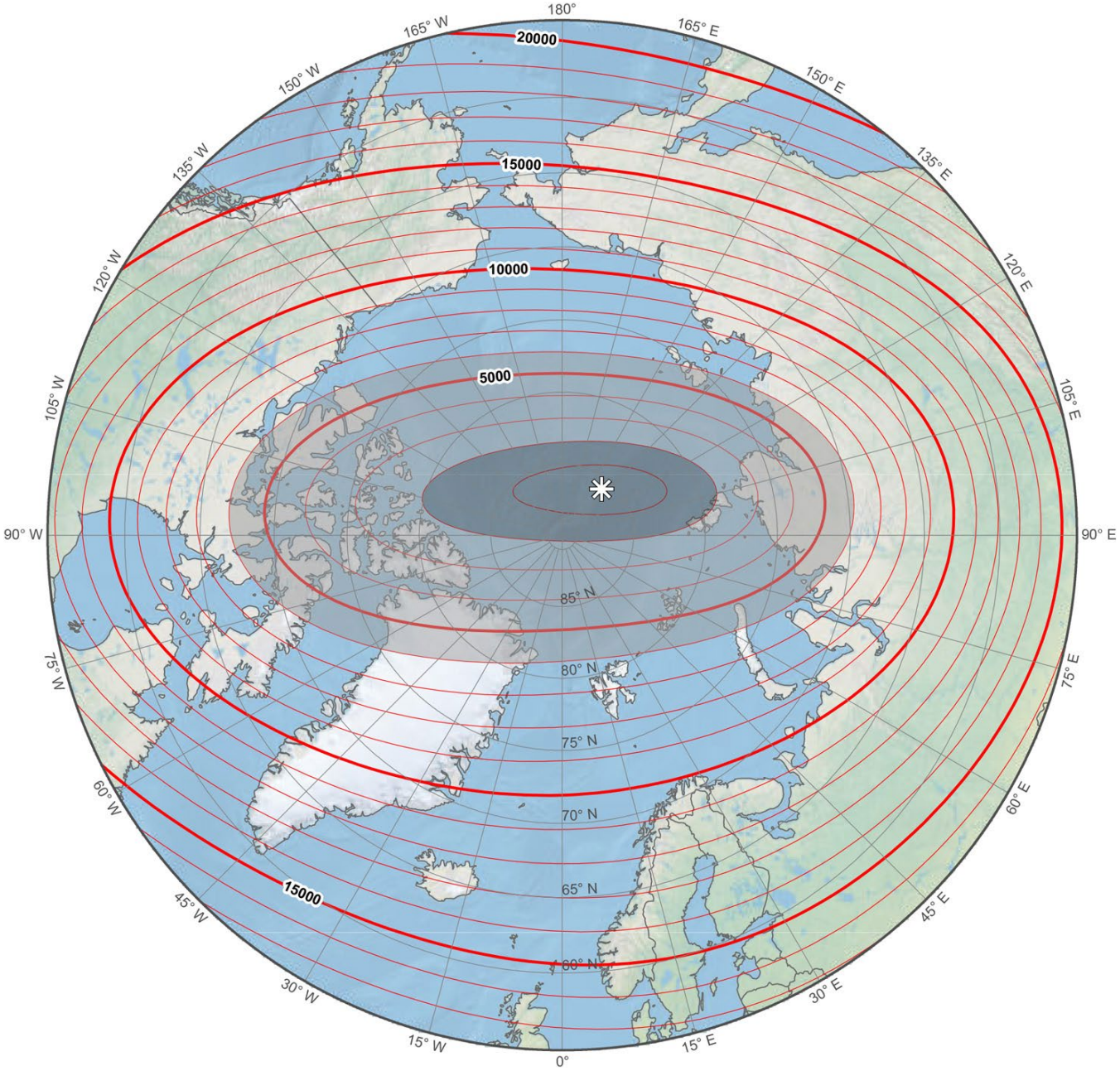

Main field horizontal intensity (H). The contour interval is 1000 nT. North Polar Region. Polar stereographic projection.

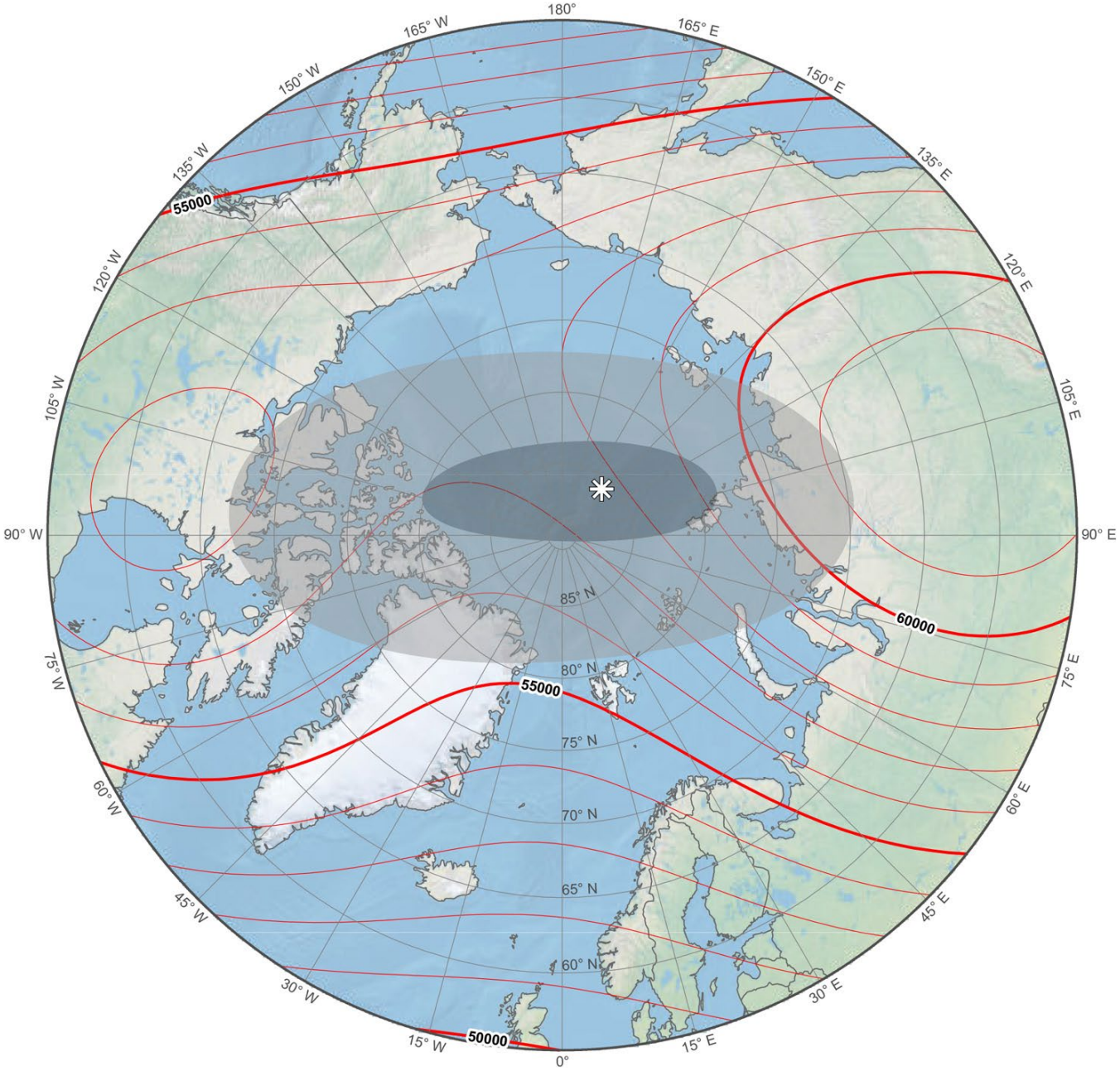

Main field total intensity (F). The contour interval is 1000 nT. North Polar Region. Polar stereographic projection.

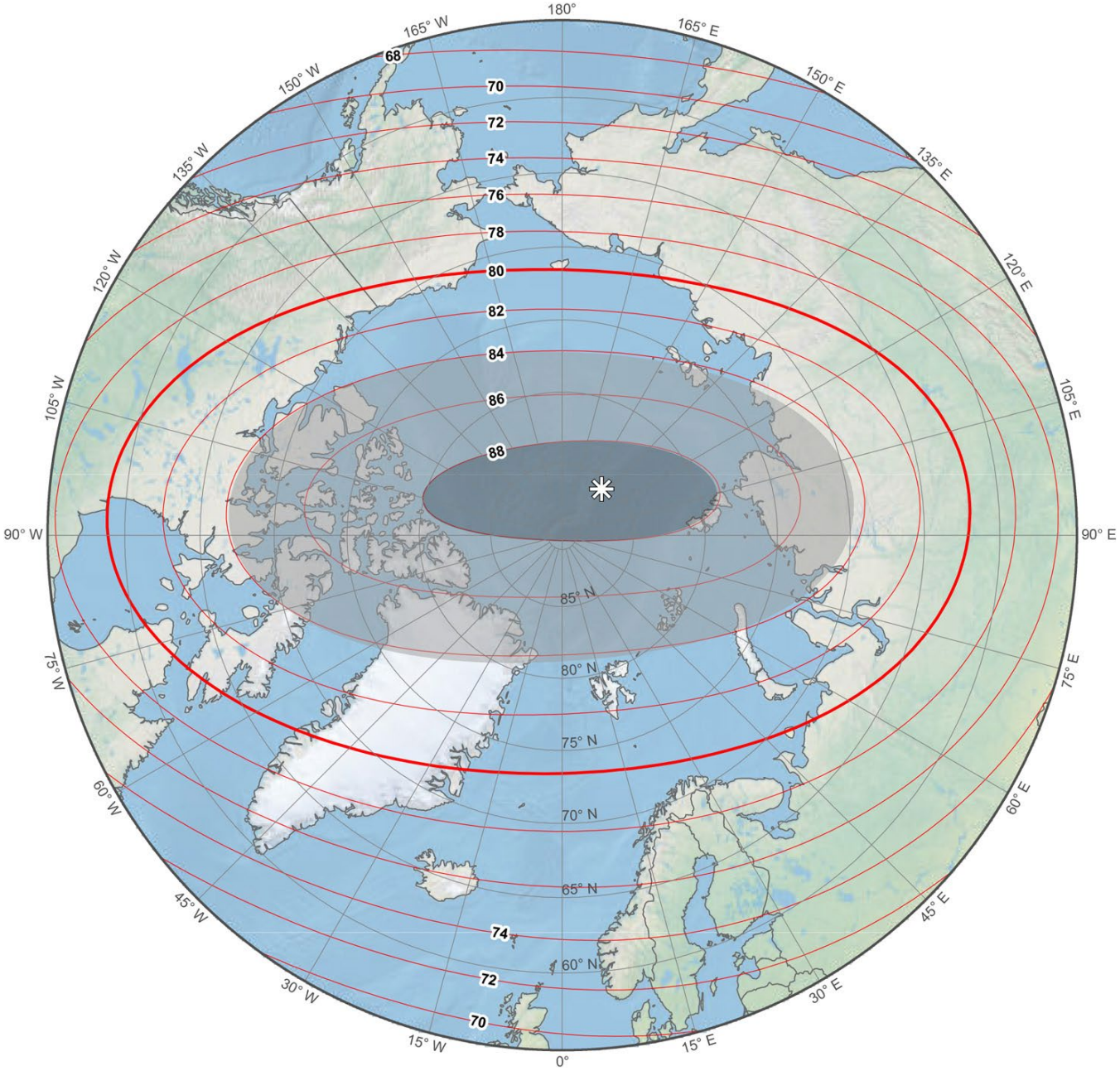

Main field inclination (I). The contour interval is 2 degrees. North Polar Region. Polar stereographic projection.

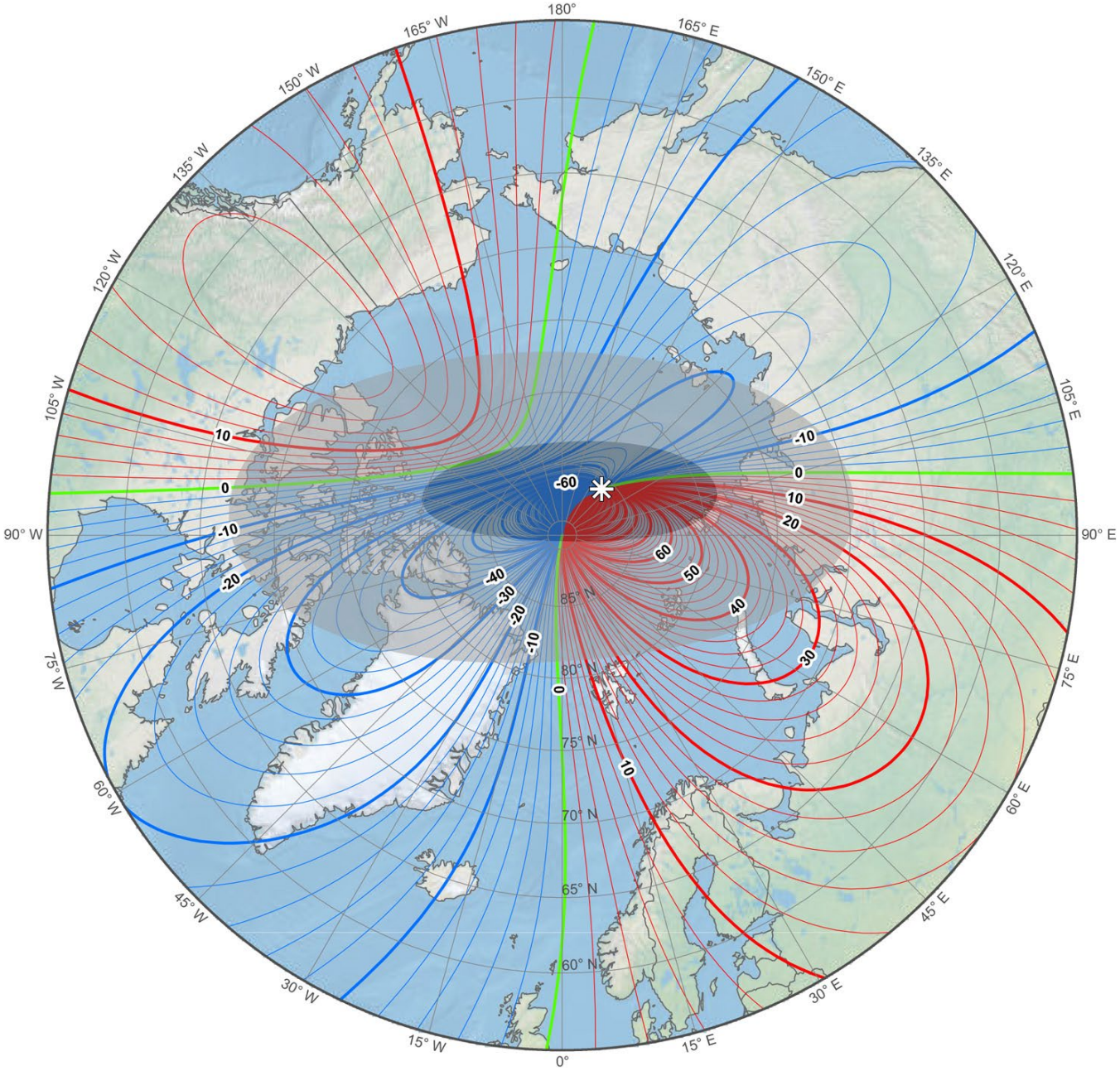

Main field declination (D). The contour interval is 2 degrees, red contours positive (east); blue negative (west); green zero (agonic) line. North Polar Region. Polar stereographic projection.

Main field maps: South Polar stereographic projection

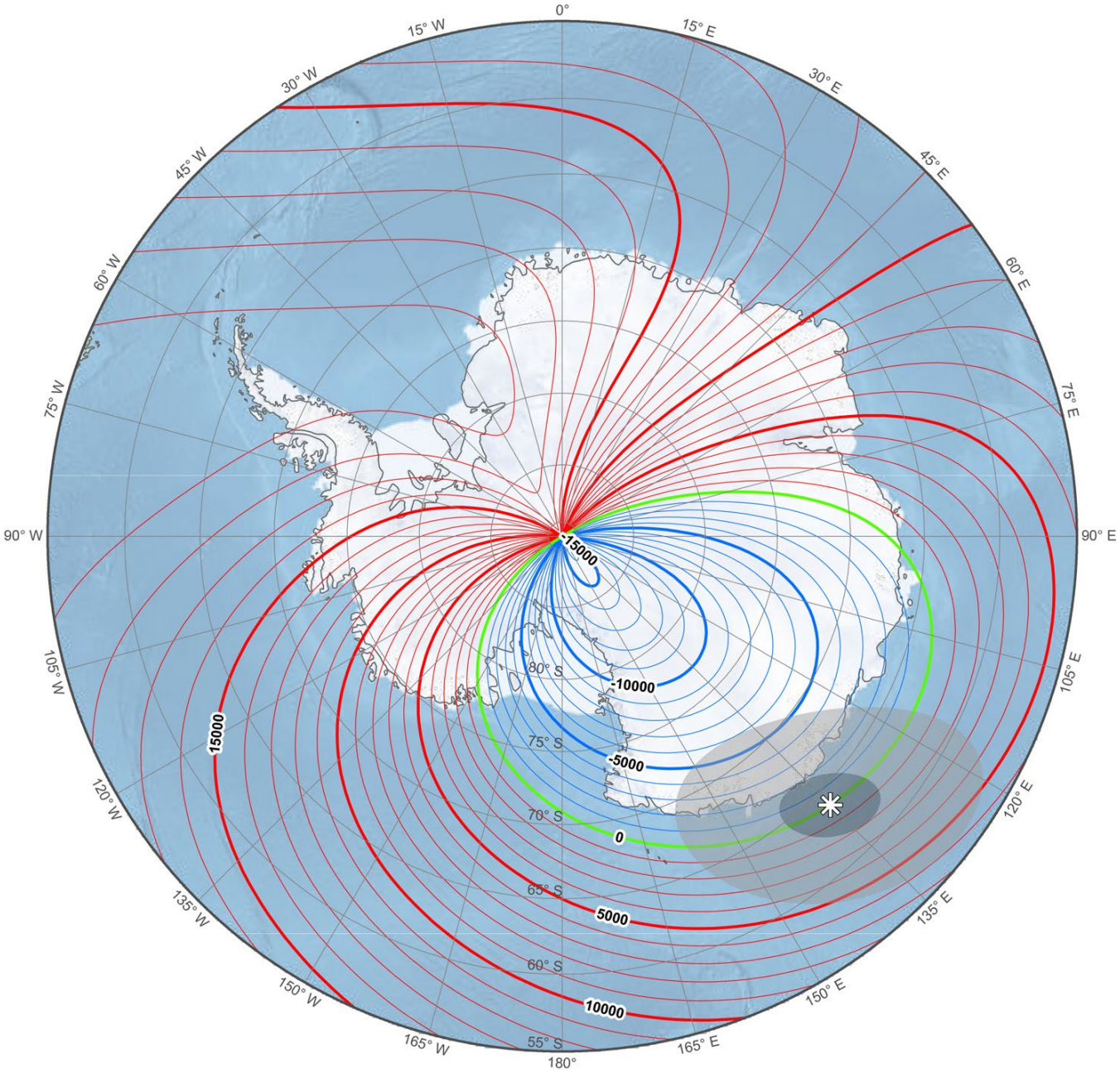

Main field north component (X). The contour interval is 1000 nT, red contours positive (north); blue negative (south); green zero line. South Polar Region. Polar stereographic projection.

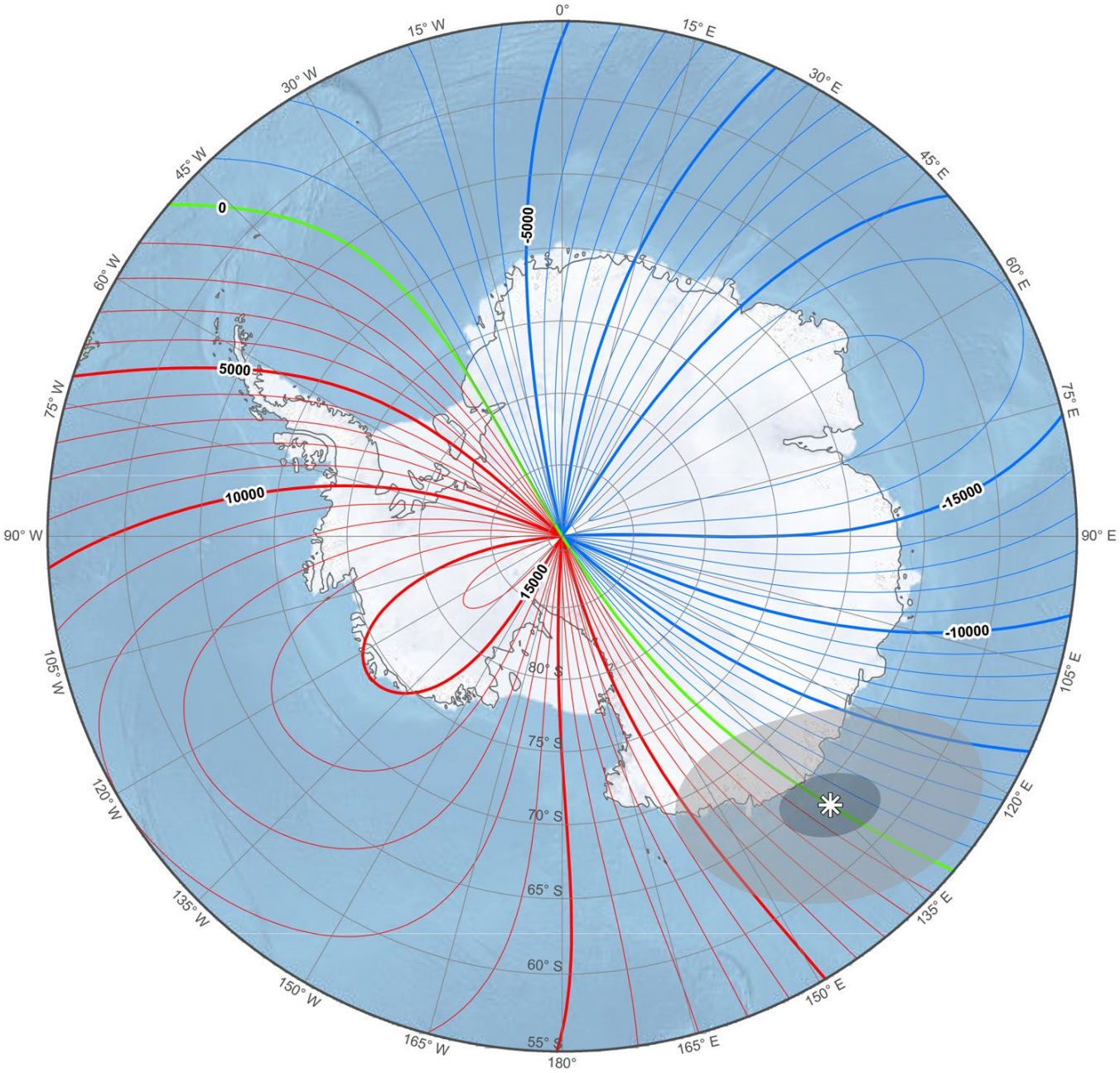

Main field east component (Y). The contour interval is 1000 nT, red contours positive (east); blue negative (west); green zero line. South Polar Region. Polar stereographic projection.

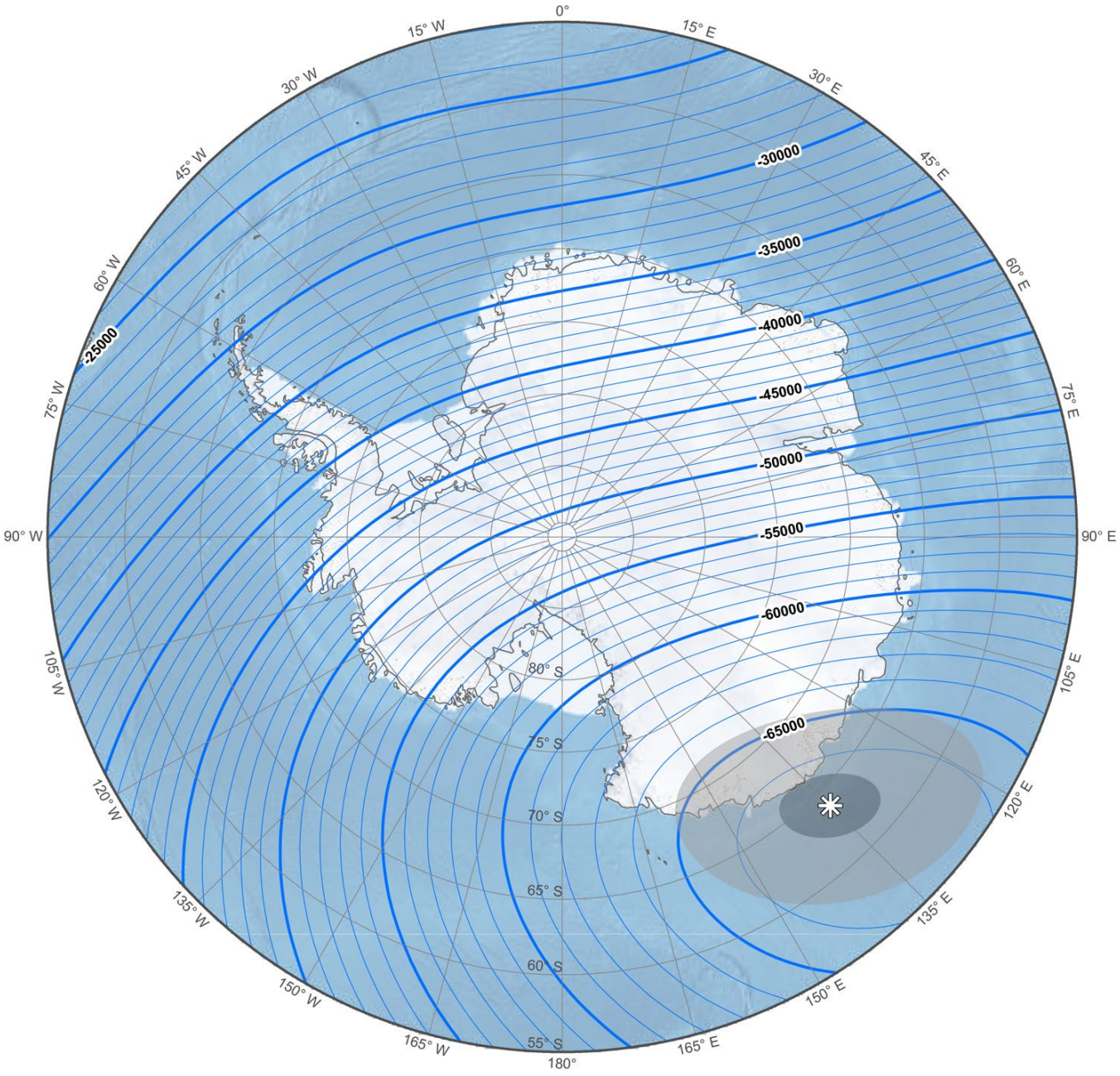

Main field down component (Z). The contour interval is 1000 nT. South Polar Region. Polar stereographic projection.

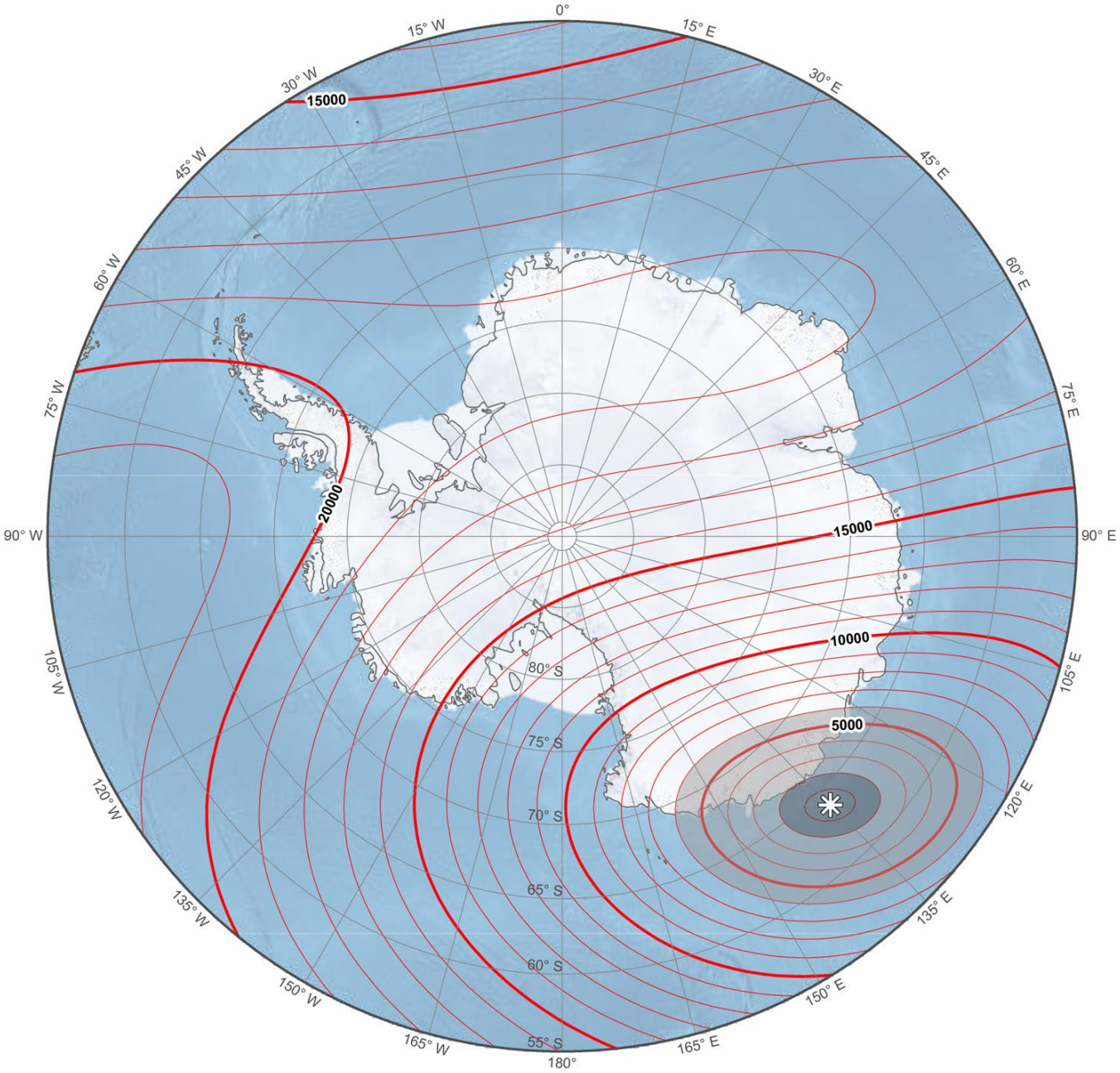

Main field horizontal intensity (H). The contour interval is 1000 nT. South Polar Region. Polar stereographic projection.

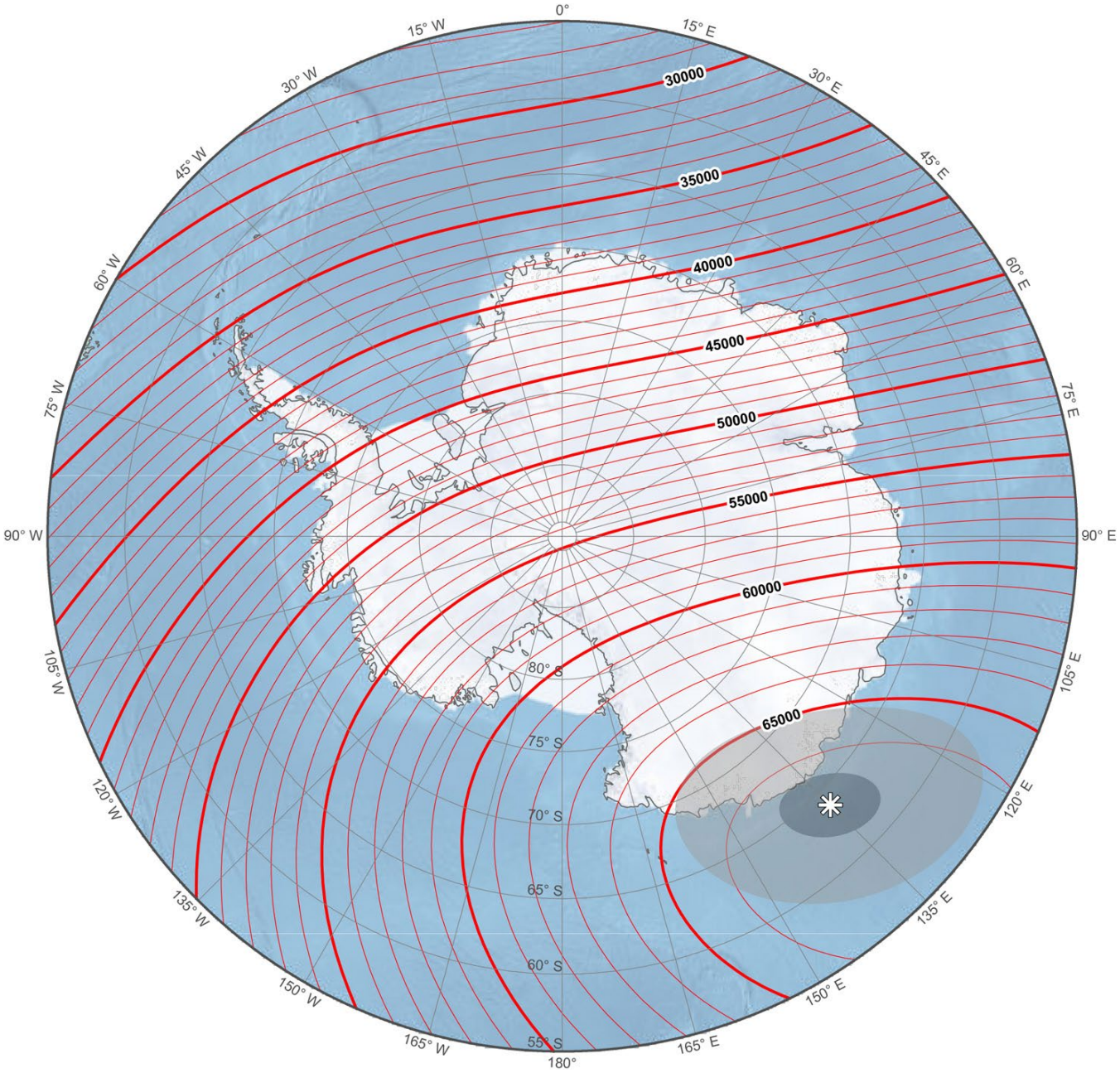

Main field total intensity (F). The contour interval is 1000 nT. South Polar Region. Polar stereographic projection.

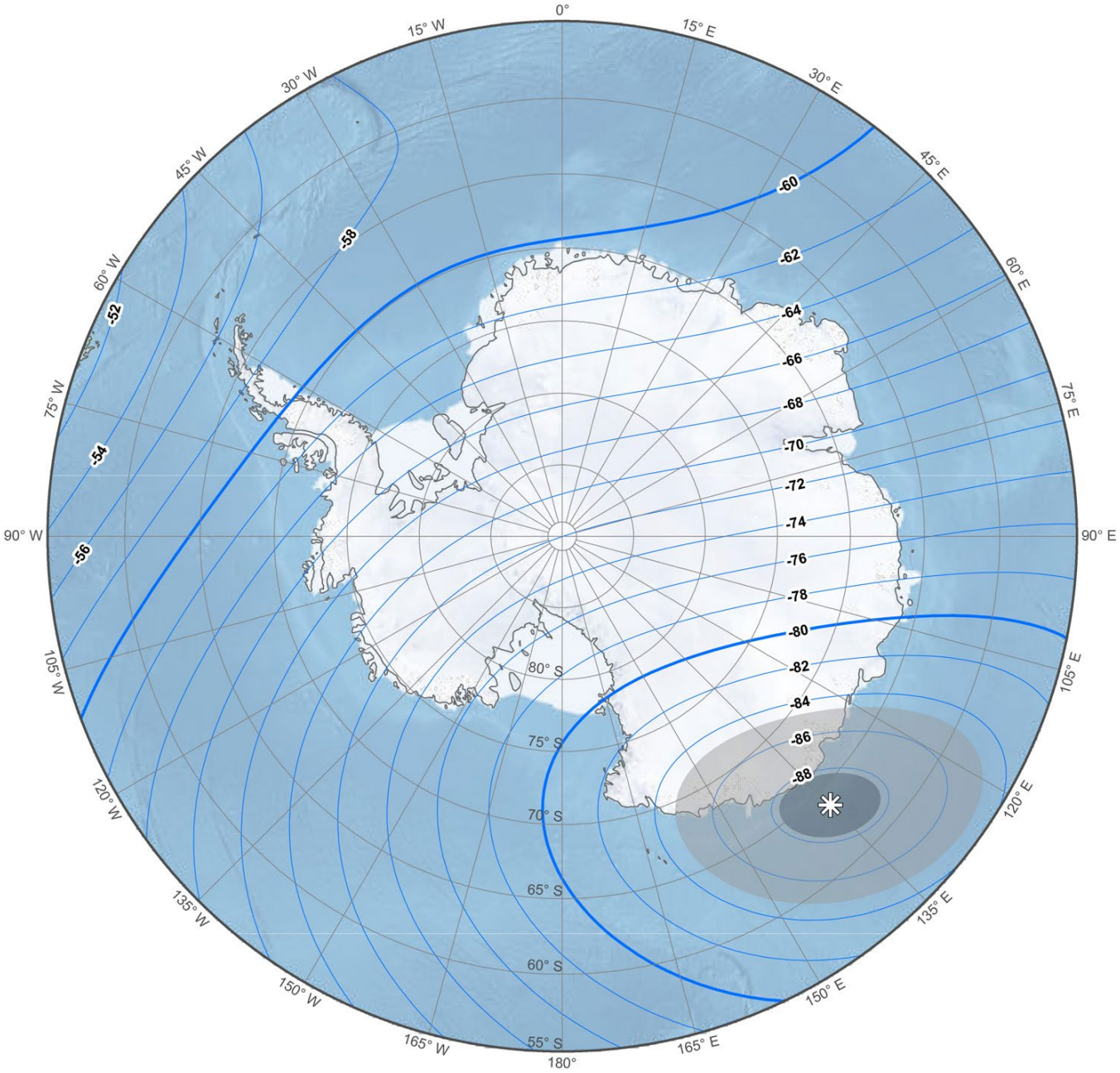

Main field inclination (I). The contour interval is two degrees. South Polar Region. Polar stereographic projection.

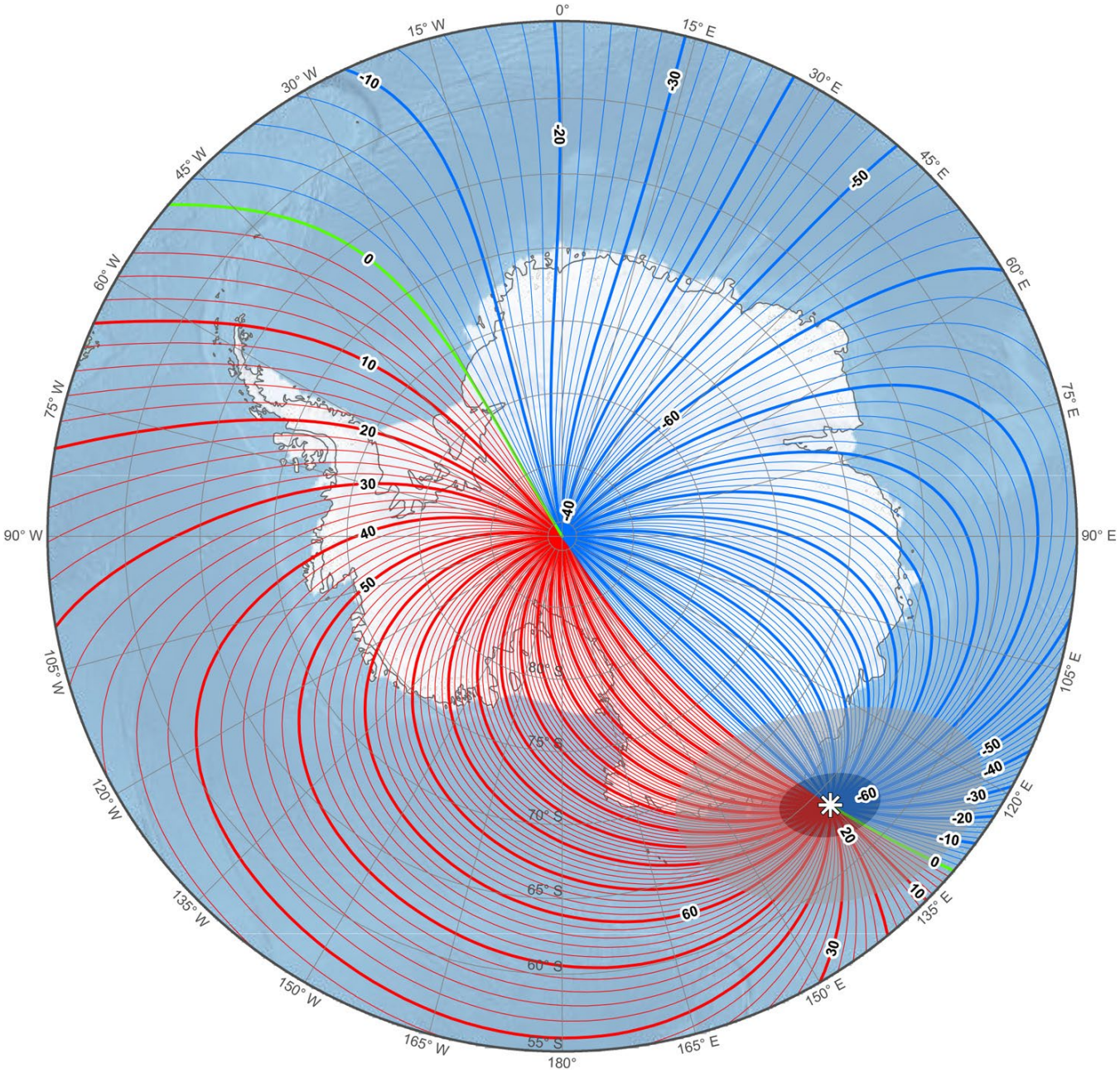

Main field declination (D). The contour interval is two degrees, red contours positive (east); blue negative (west); green zero (agonic) line. South Polar Region. Polar stereographic projection.

Secular variation maps: Miller projection

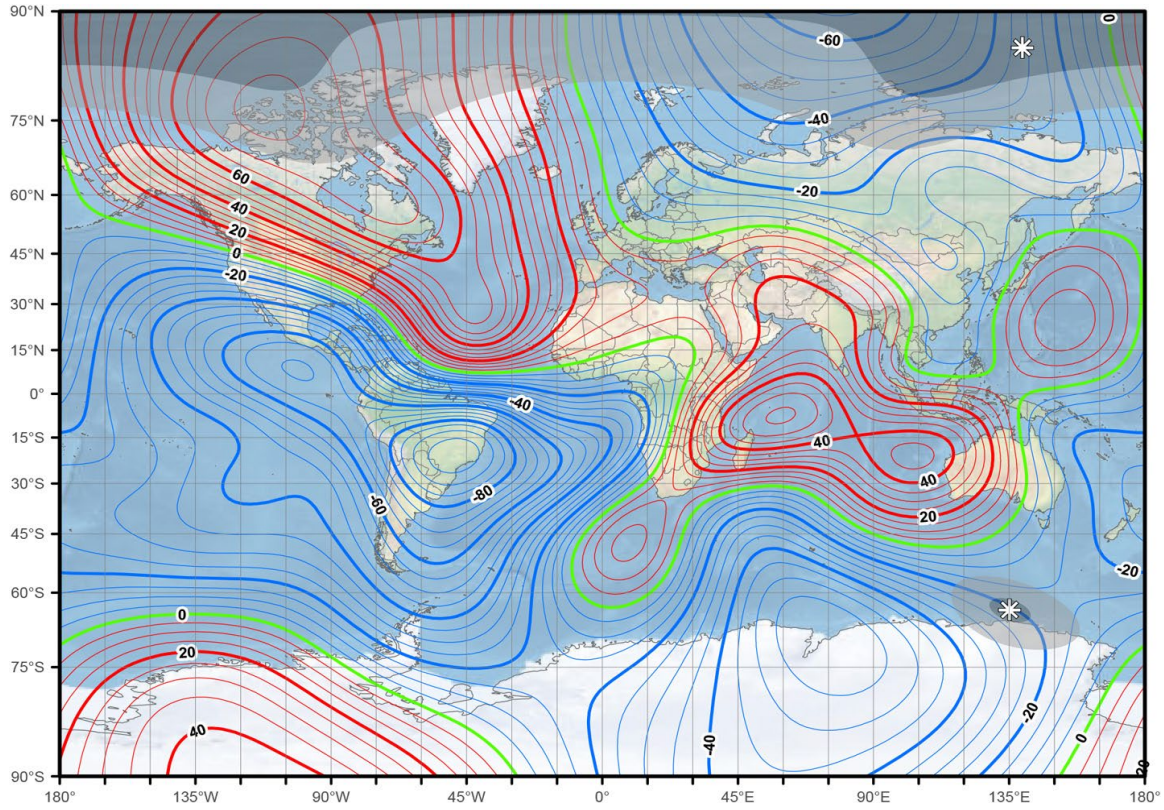

Annual change north component (X). The contour interval is 5 nT / year, red contours positive (north) change; blue negative (south) change; green zero change. Miller projection.

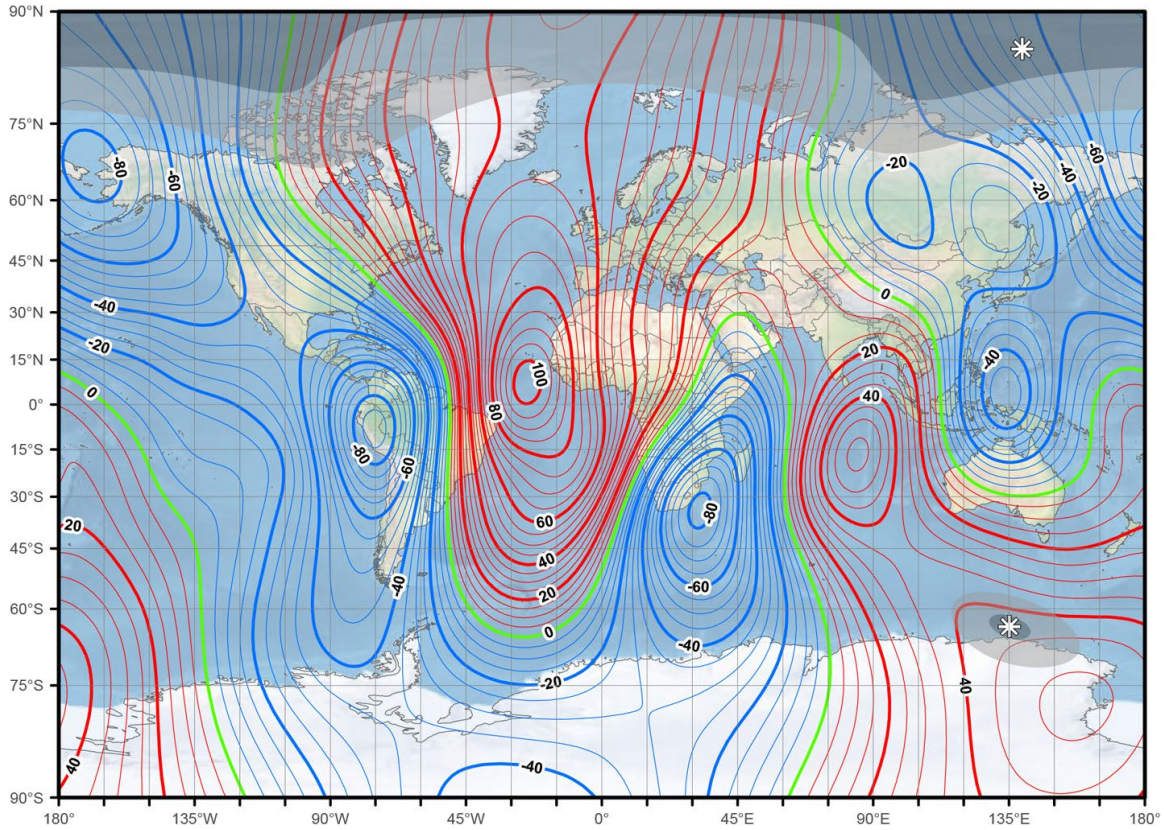

Annual change east component (Y). The contour interval is 5 nT / year, red contours positive (east) change; blue negative (west) change; green zero change. Miller projection.

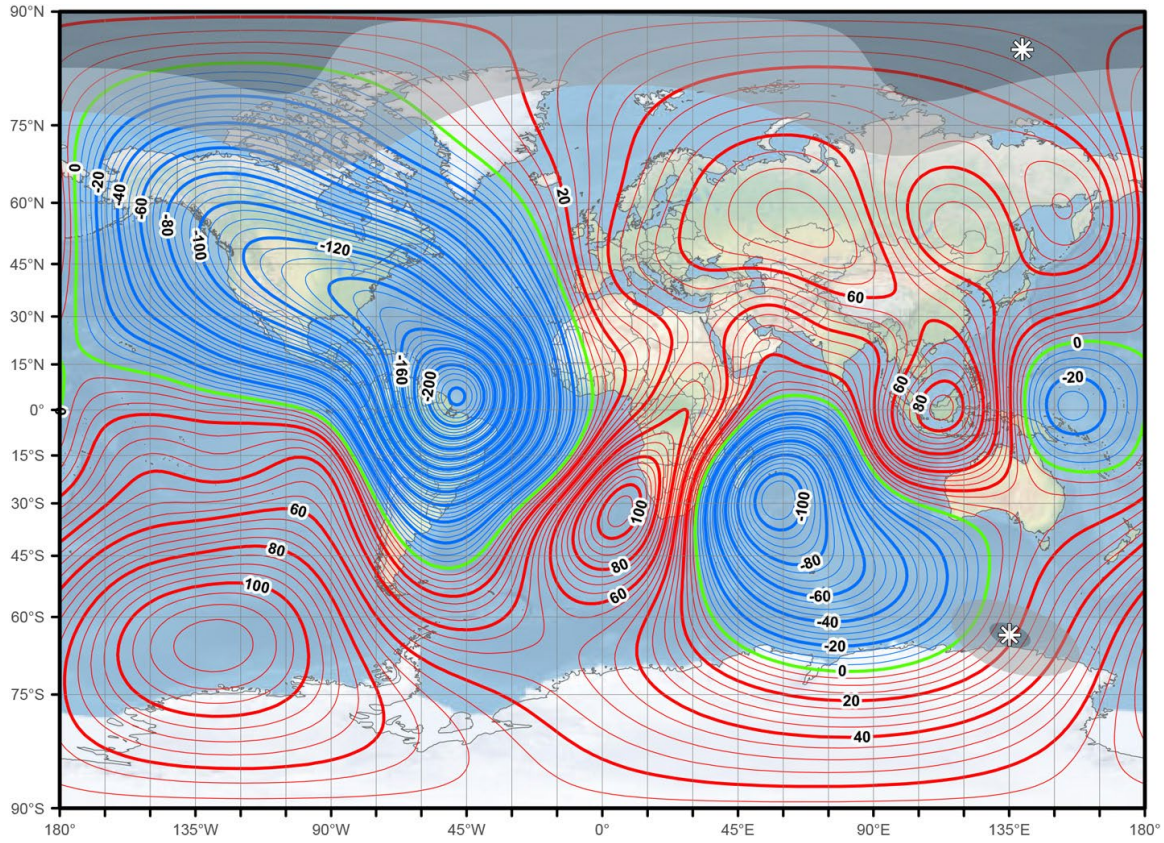

Annual change down component (Z). The contour interval is 5 nT / year, red contours positive (down) change; blue negative (up) change; green zero change. Miller projection.

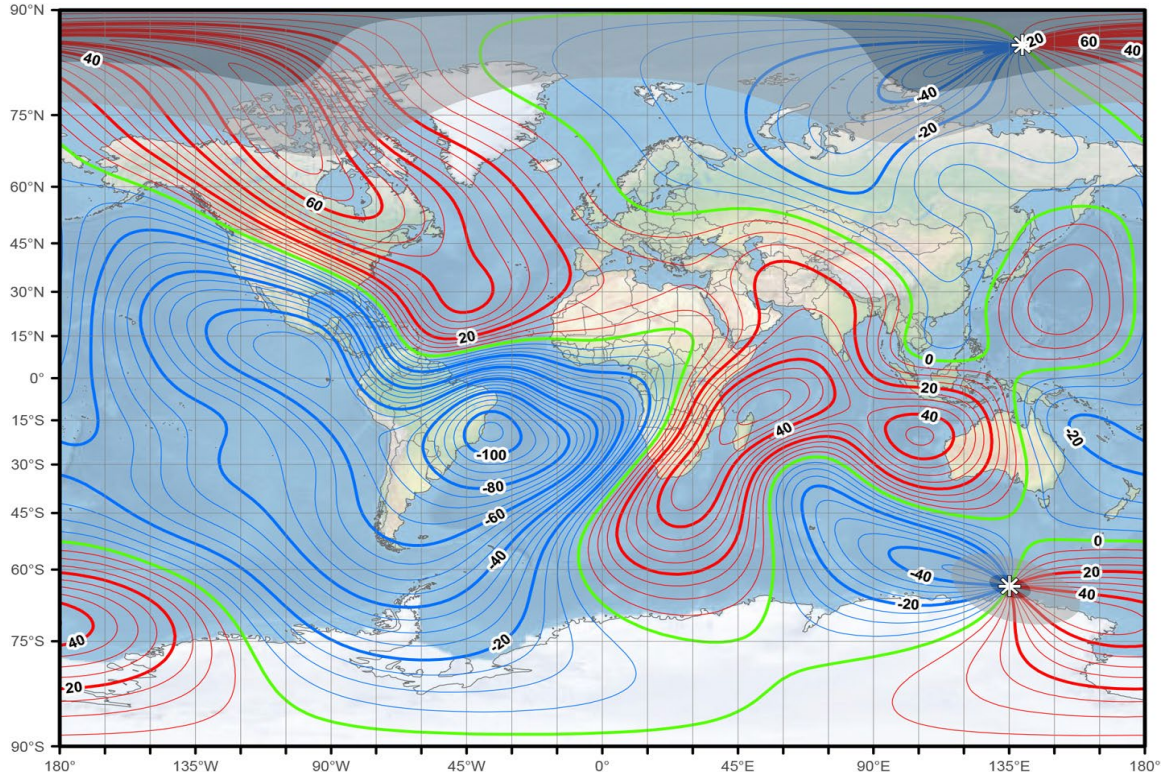

Annual change horizontal intensity (H). The contour interval is 5 nT / year, red contours positive change; blue negative change; green zero change. Miller projection.

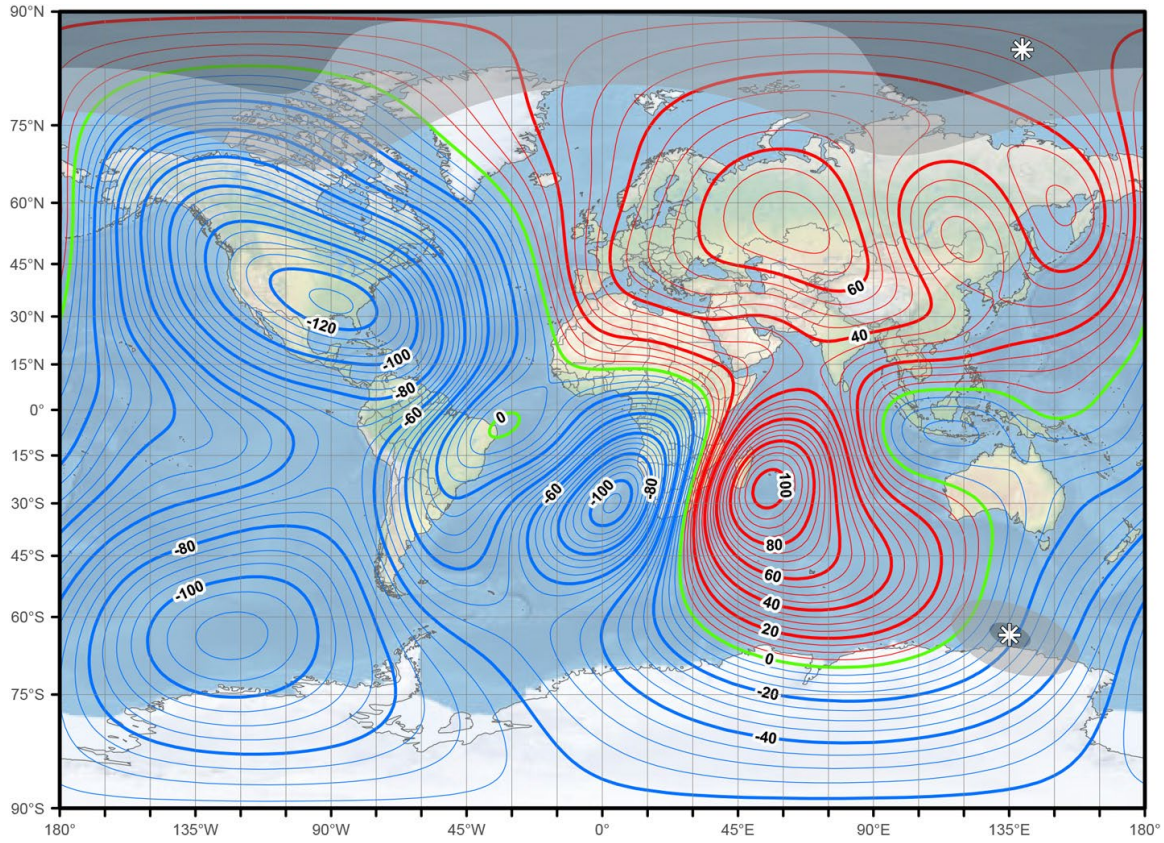

Annual change total intensity (F). The contour interval is 5 nT / year, red contours positive change; blue negative change; green zero change. Miller projection.

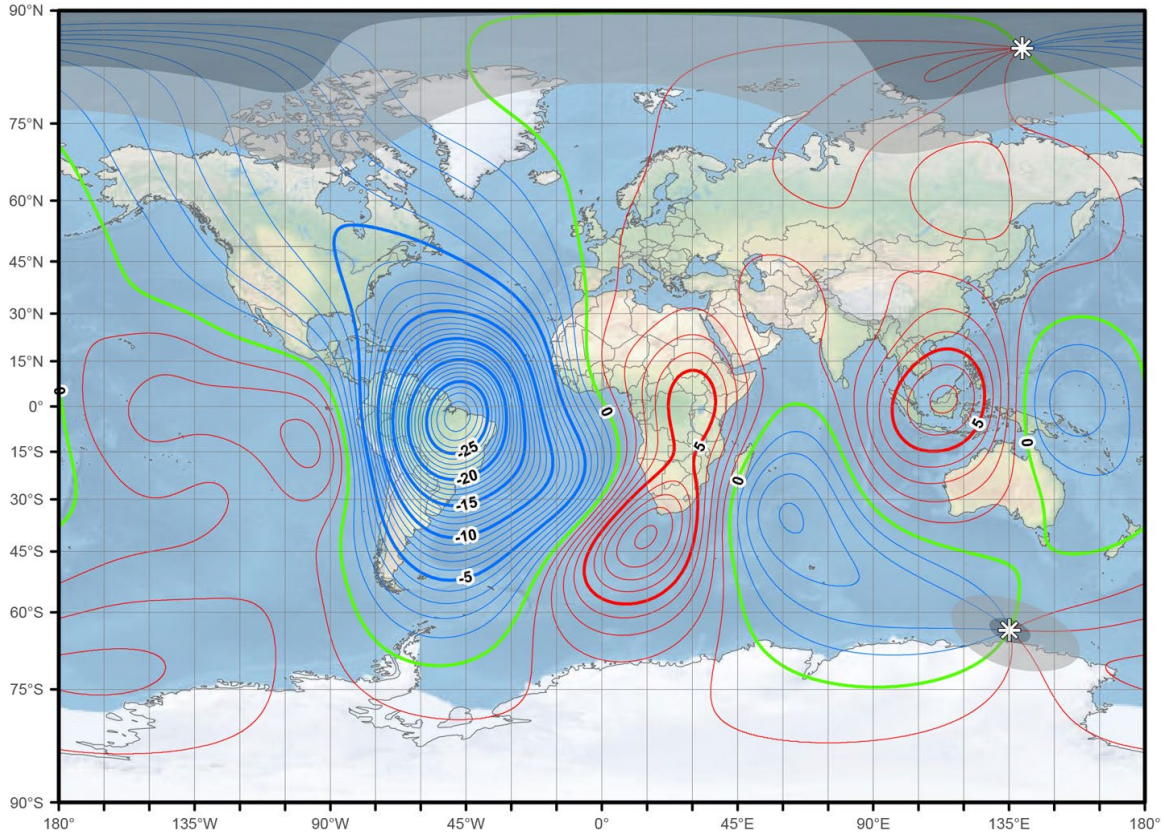

Annual change inclination (I). The contour interval is one arc-minute / year, red contours positive (downward) change; blue negative (upward) change; green zero change. Miller projection.

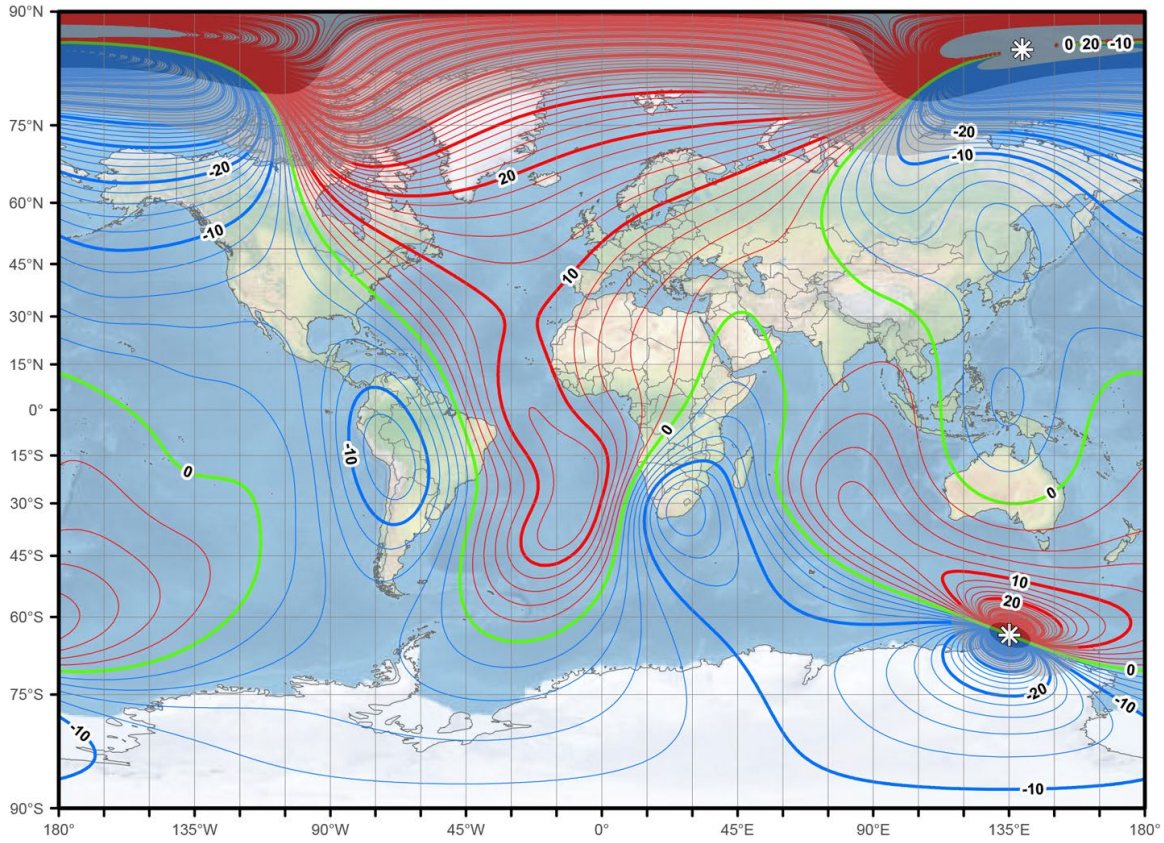

Annual change declination (D). The contour interval is two arc-minutes / year, red contours positive (clockwise) change; blue negative (counter-clockwise) change; green zero change. Miller projection. (The darkest grey masked contours near the magnetic poles do not represent the blackout or caution zones.)

Secular variation maps: North Polar stereographic projection

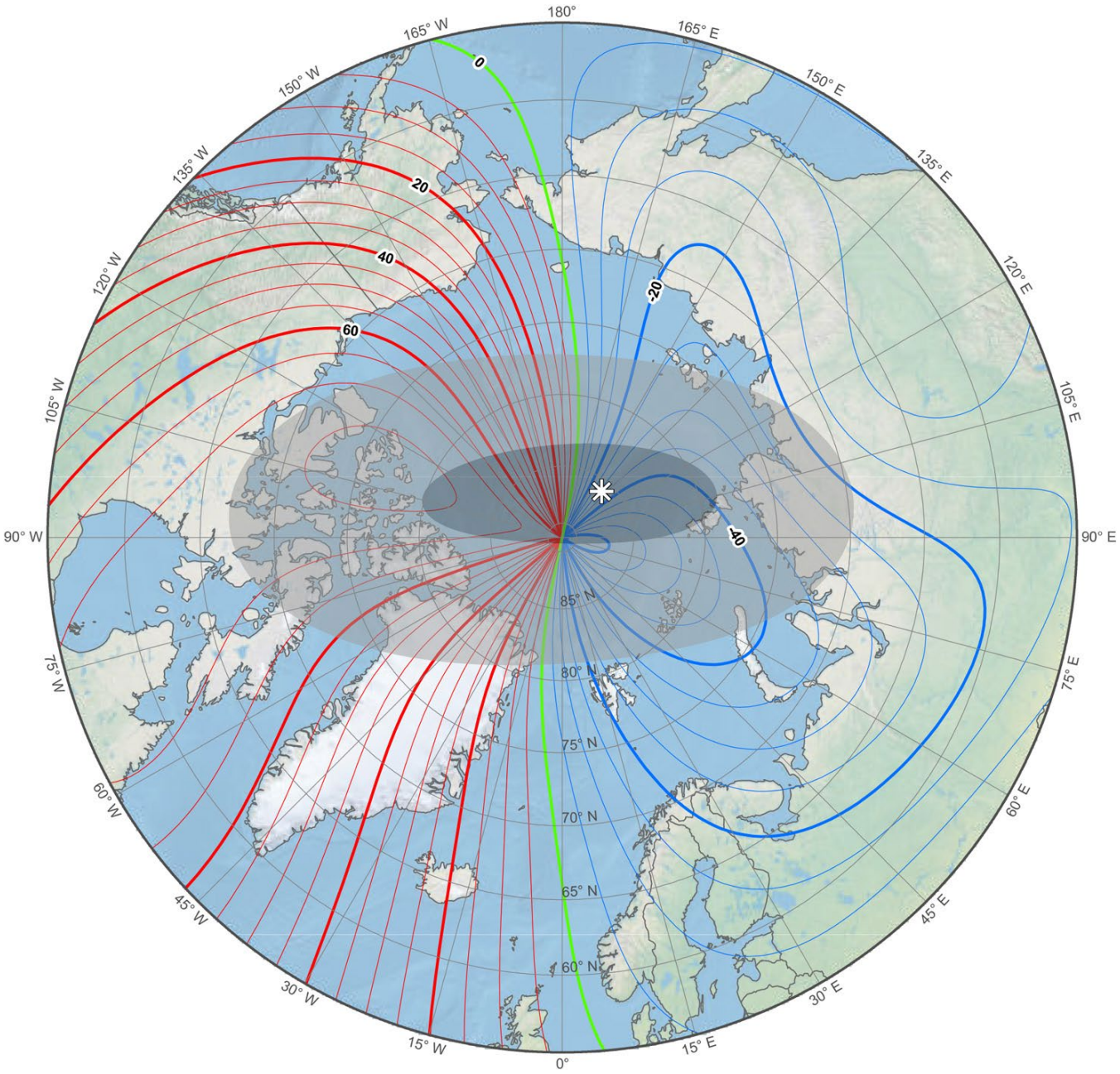

Annual change north component ($\dot{X}$). The contour interval is 5 nT / year, red contours positive (north) change; blue negative (south) change; green zero change. North Polar Region. Polar stereographic projection.

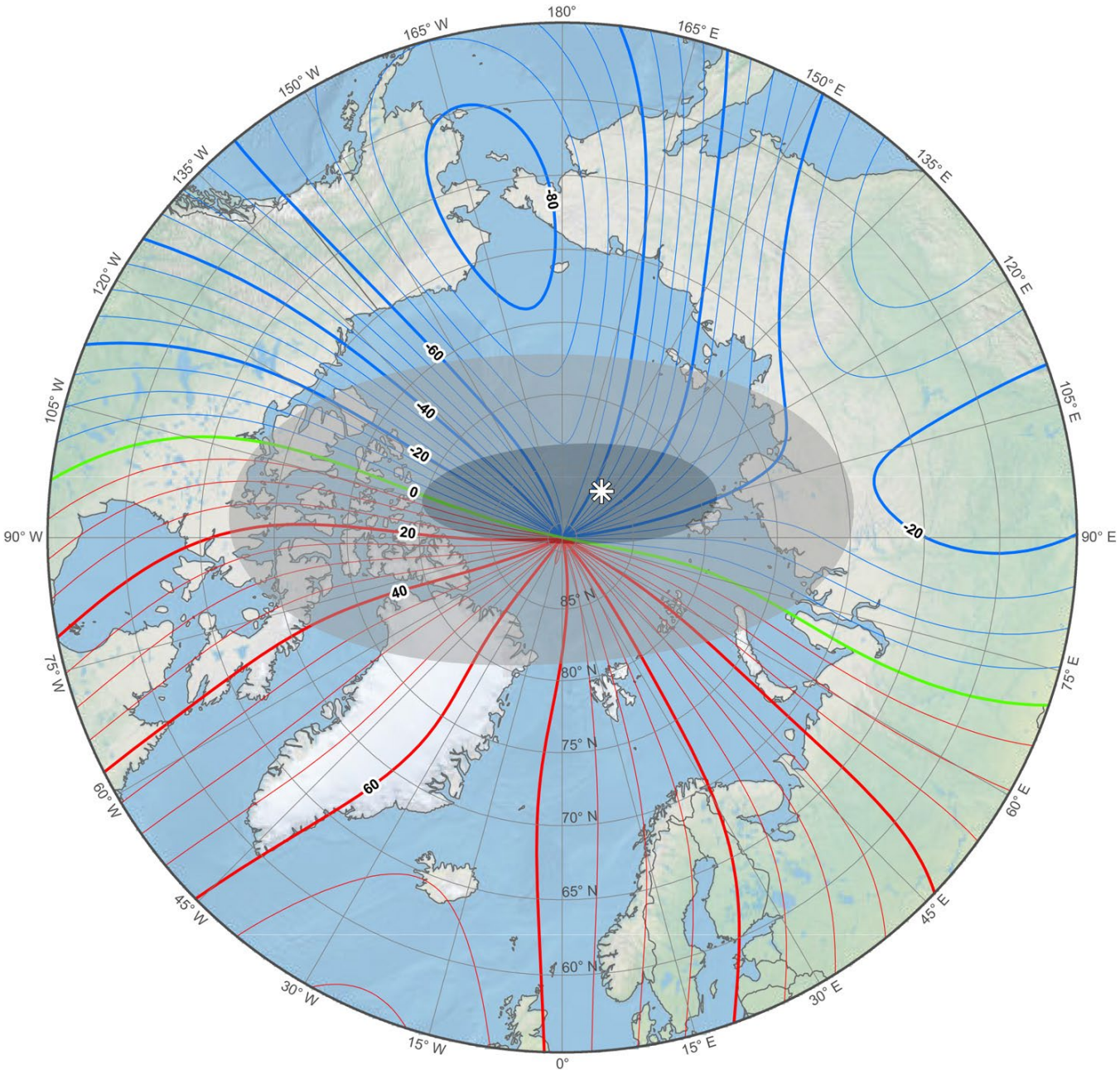

Annual change east component (Y). The contour interval is 5 nT / year, red contours positive (east) change; blue negative (west) change; green zero change. North Polar Region. Polar stereographic projection.

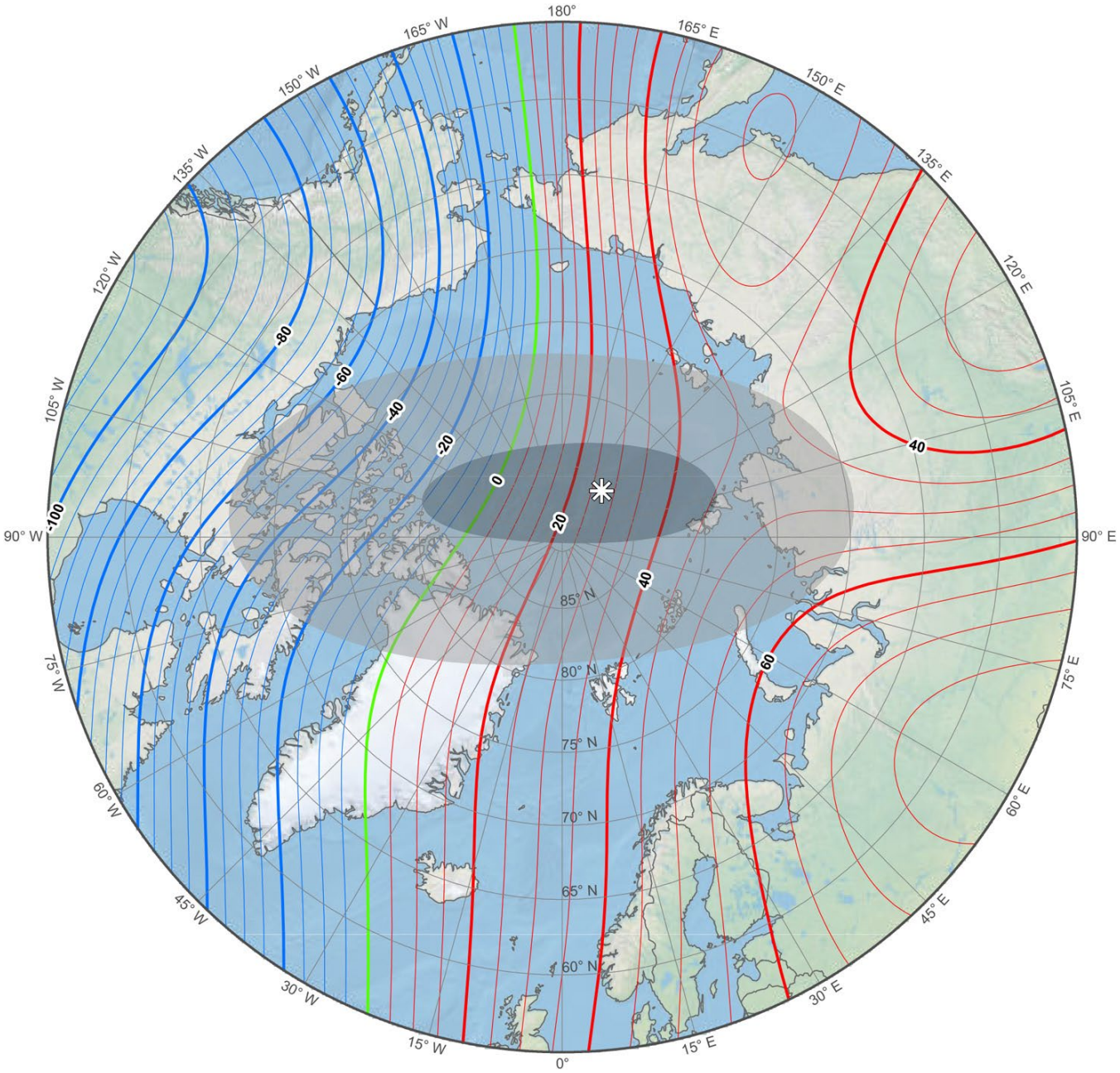

Annual change down component (Z). The contour interval is 5 nT / year, red contours positive (down) change; blue negative (up) change; green zero change. Polar stereographic projection.

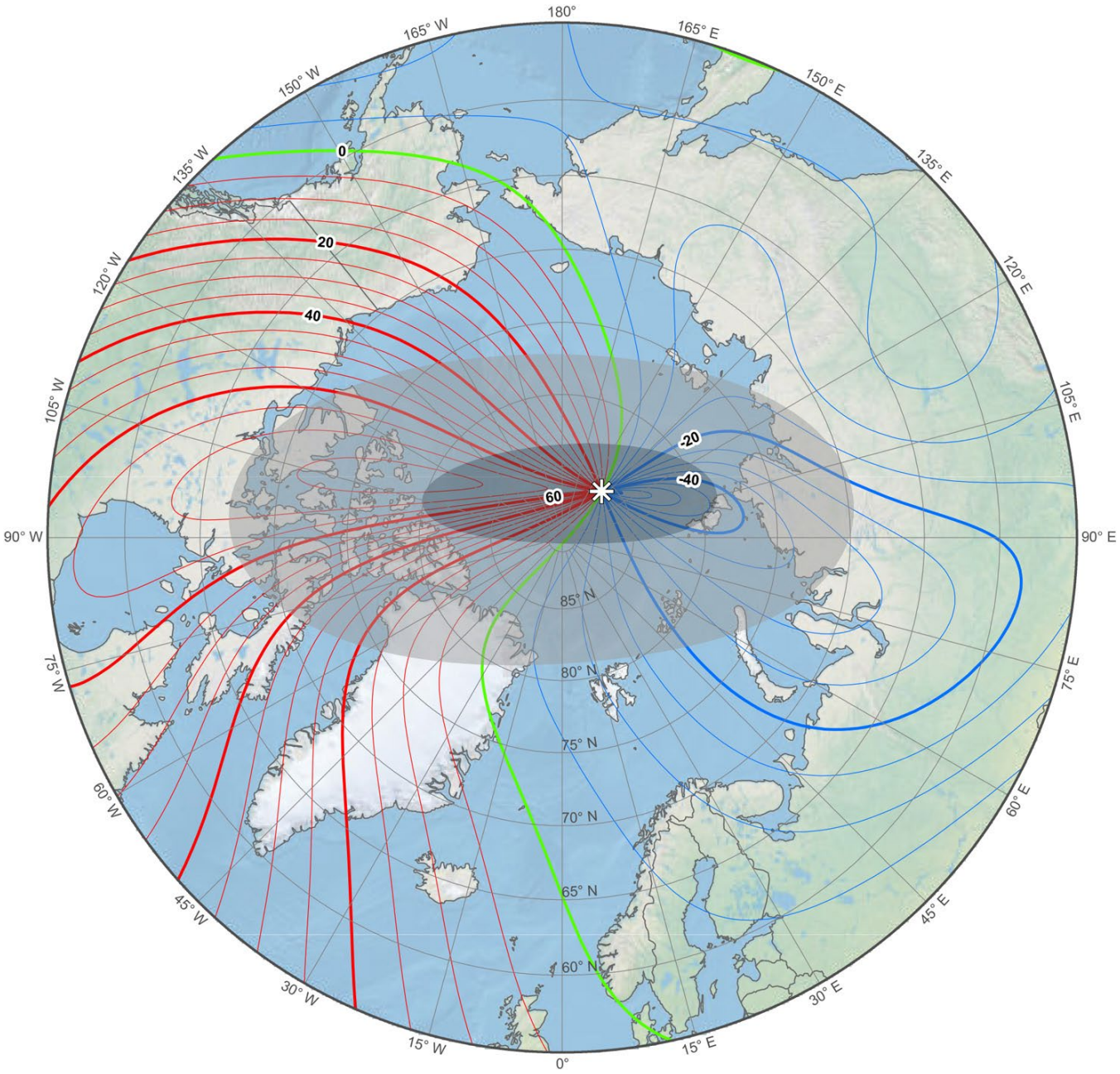

Annual change horizontal intensity (H). The contour interval is 5 nT / year, red contours positive change; blue negative change; green zero change. North Polar Region. Polar stereographic projection.

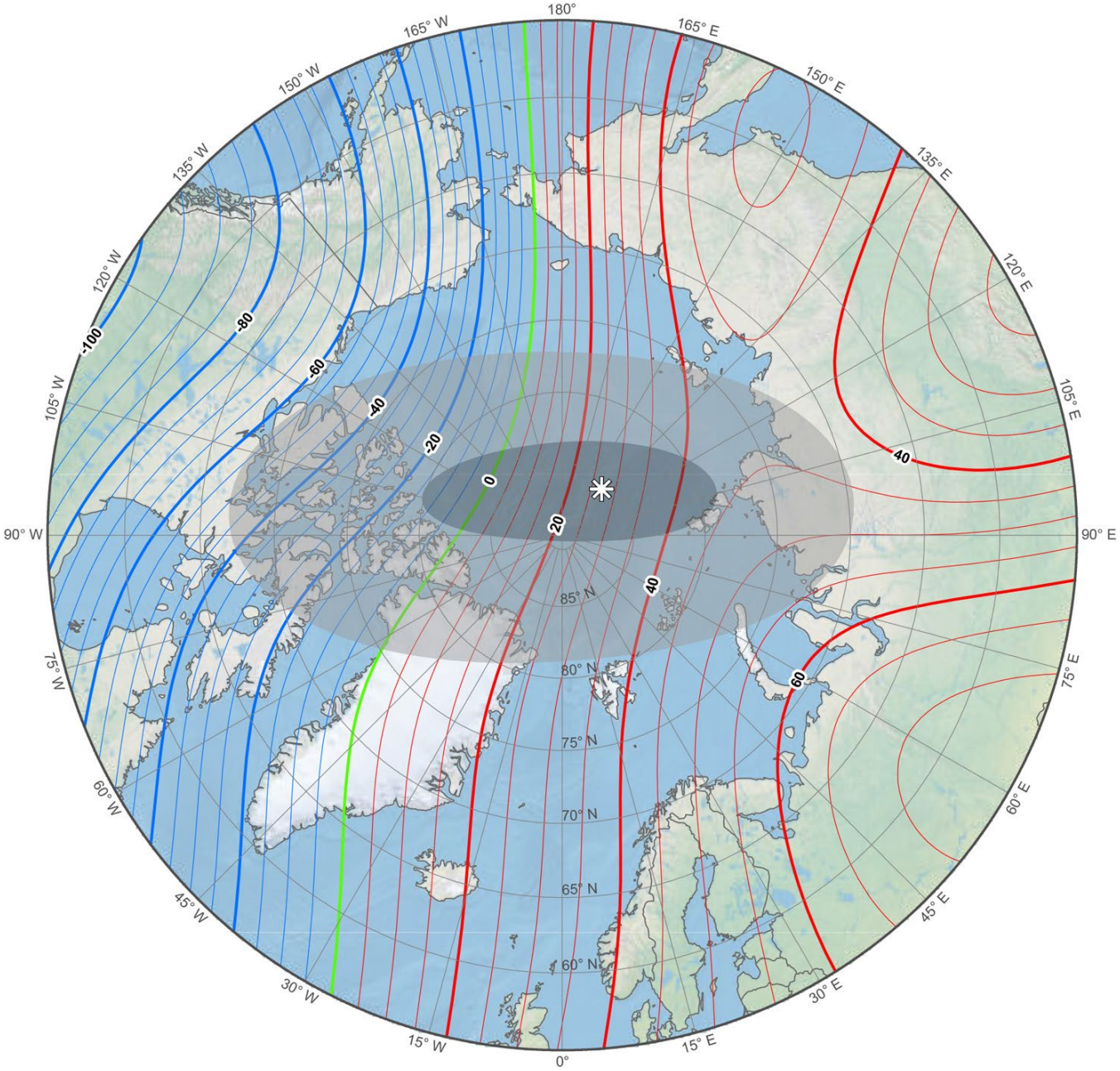

Annual change total intensity (F). The contour interval is 5 nT / year, red contours positive change; blue negative change; green zero change. North Polar Region. Polar stereographic projection.

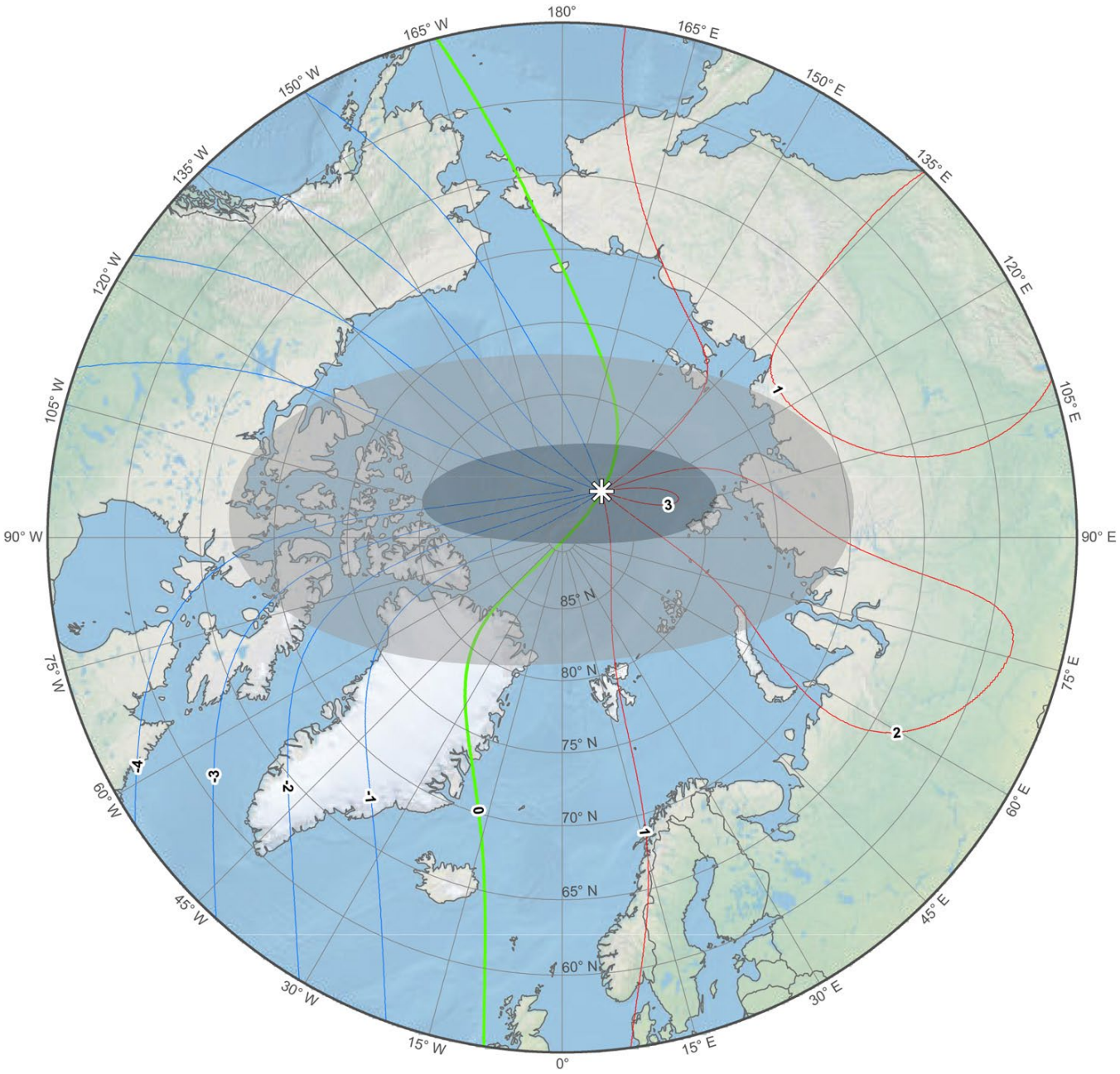

Annual change inclination (I). The contour interval is one arc-minute / year, red contours positive (downward) change; blue negative (upward) change; green zero change. North Polar Region. Polar stereographic projection.

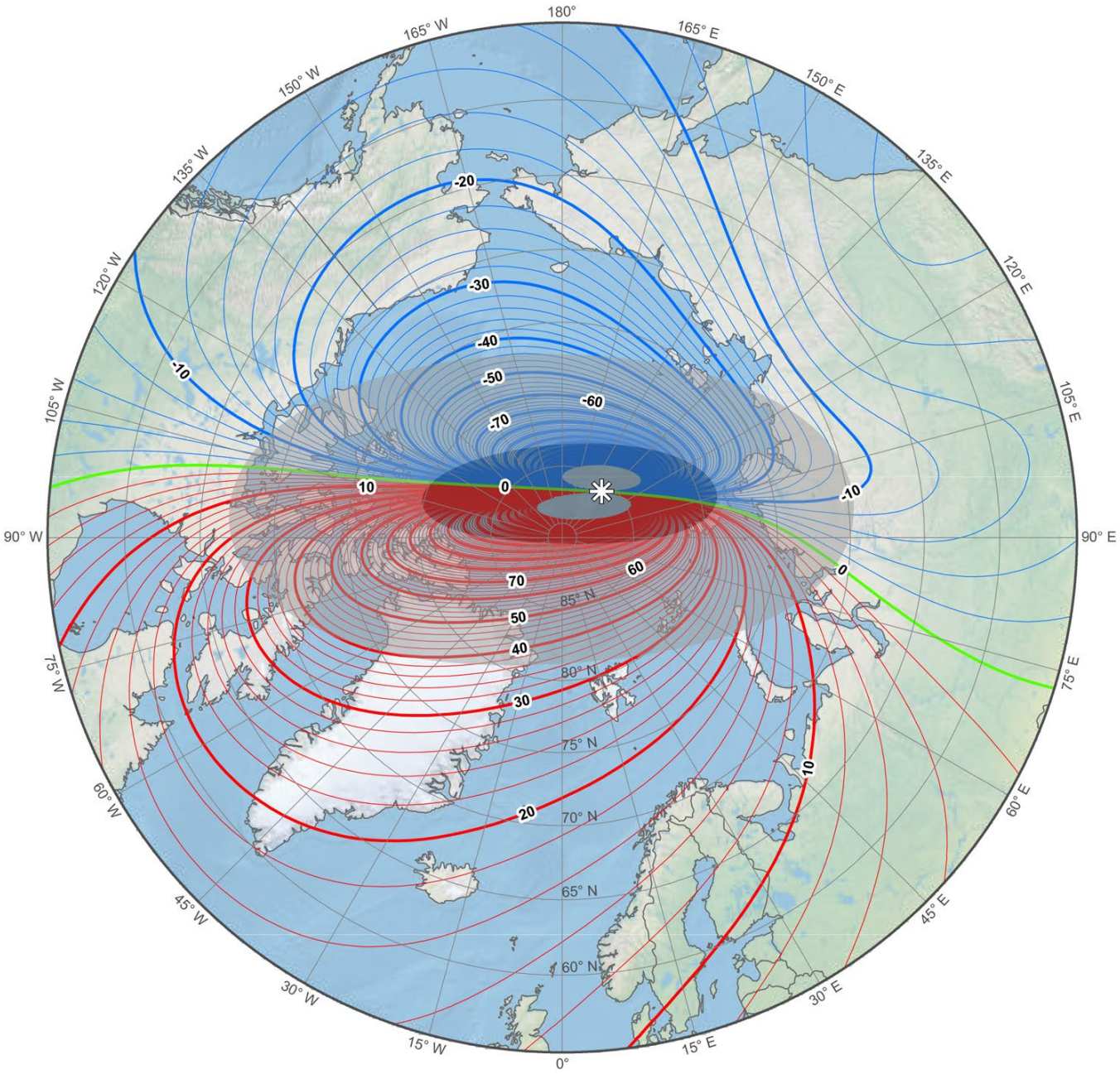

Annual change declination (D). The contour interval is two arc-minutes / year, red contours positive (clockwise) change; blue negative (counter-clockwise) change; green zero change. North Polar Region. Polar stereographic projection. (The darkest grey masked contours near the magnetic pole do not represent the blackout or caution zones.)

Secular variation maps: South Polar stereographic projection

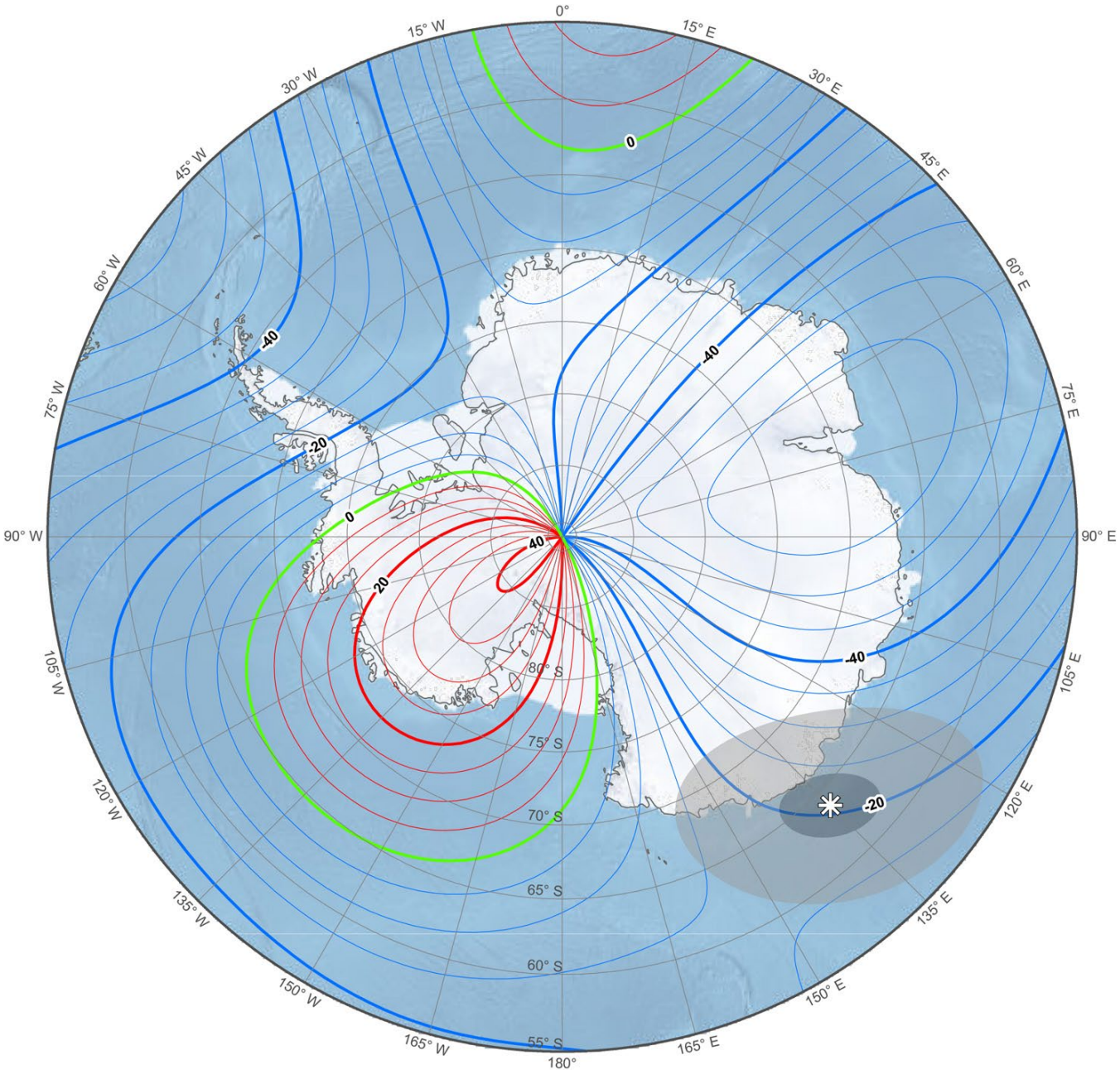

Annual change north component (X). The contour interval is 5 nT / year, red contours positive (north) change; blue negative (south) change; green zero change. South Polar Region. Polar stereographic projection.

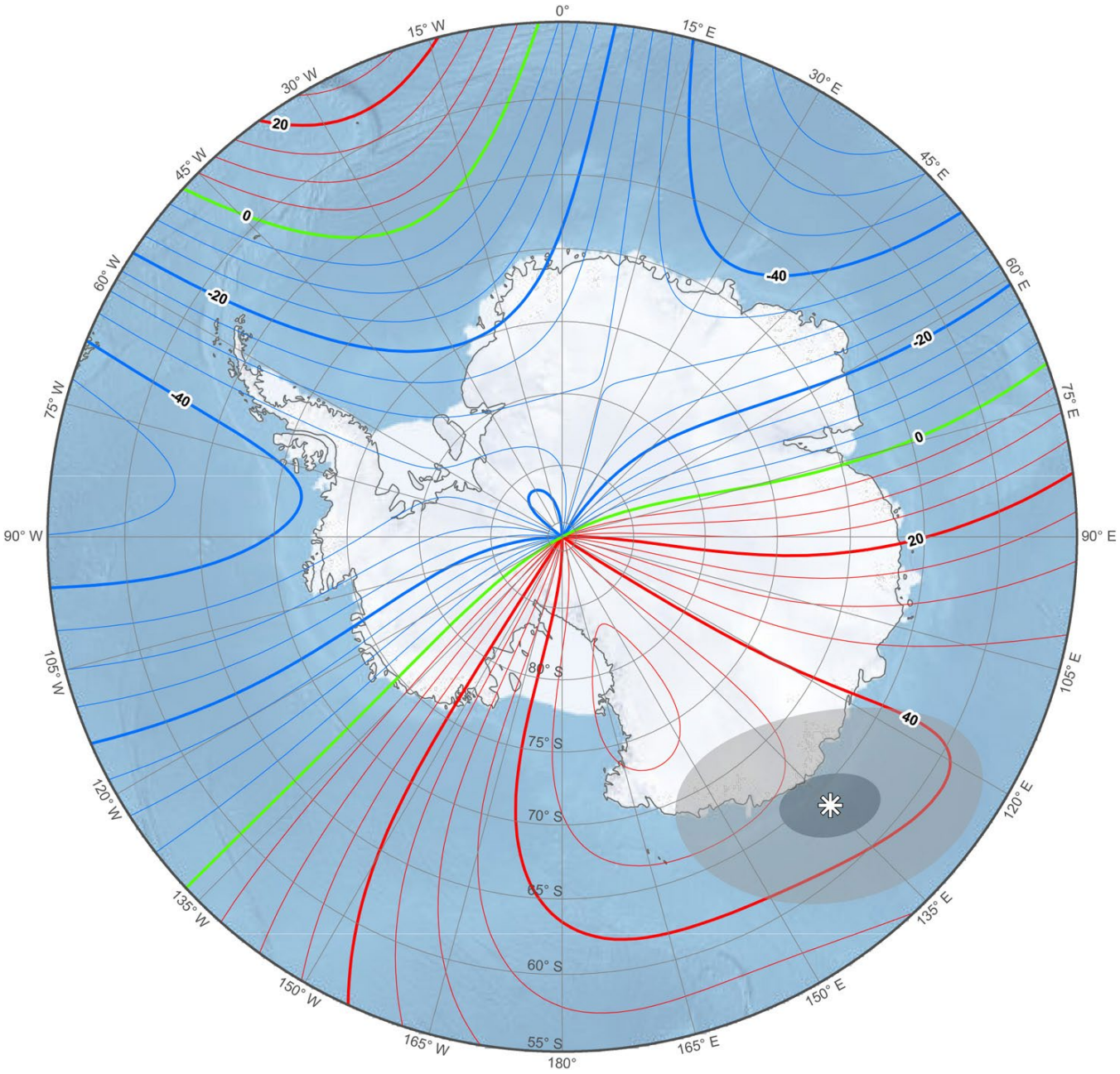

Annual change east component (Y). The contour interval is 5 nT / year, red contours positive (east) change; blue negative (west) change; green zero change. South Polar Region. Polar stereographic projection.

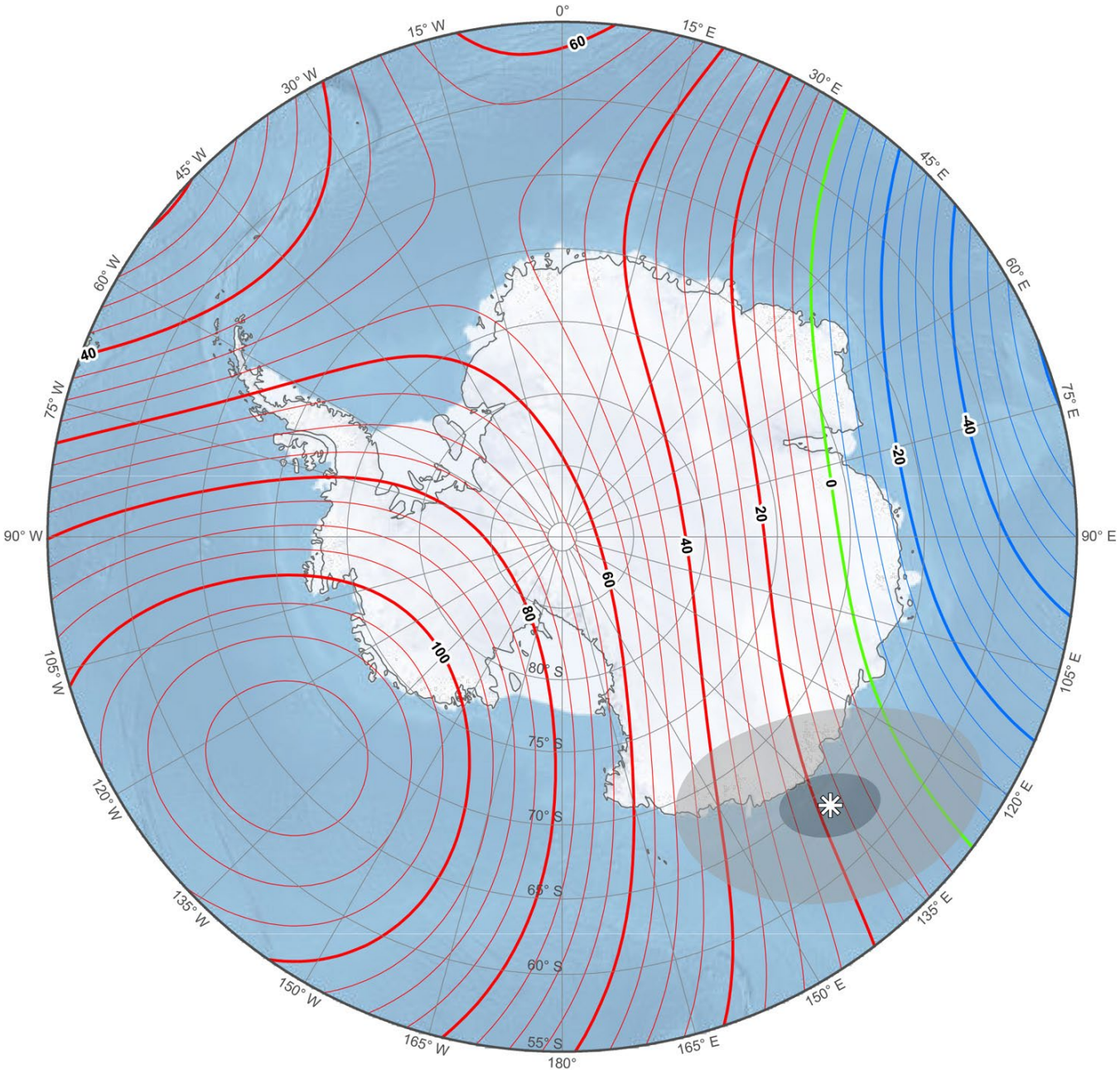

Annual change down component ($\dot{Z}$). The contour interval is 5 nT / year, red contours positive (down) change; blue negative (up) change; green zero change. South Polar Region. Polar stereographic projection.

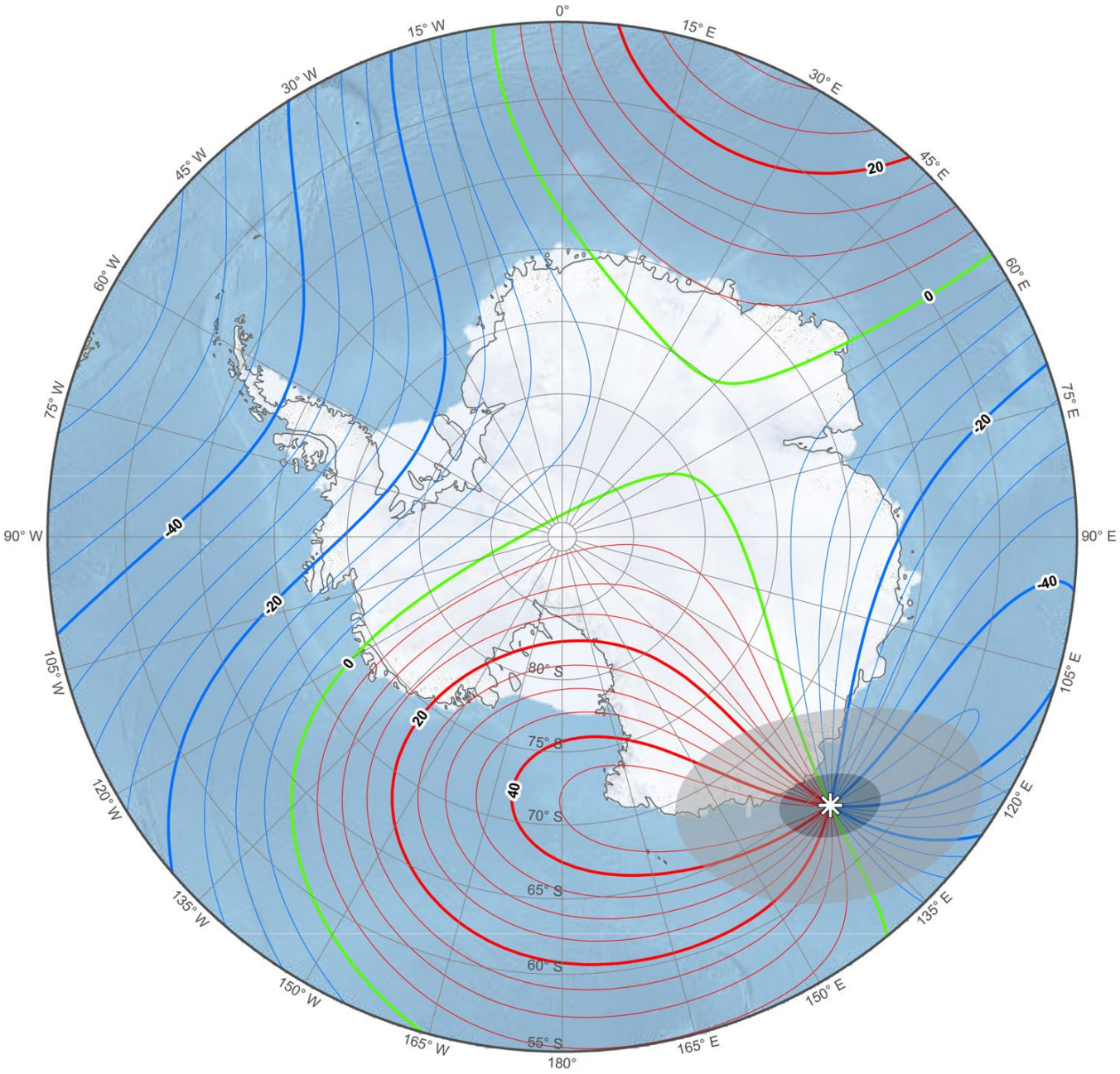

Annual change horizontal intensity (H). The contour interval is 5 nT / year, red contours positive change; blue negative change; green zero change. South Polar Region. Polar stereographic projection.

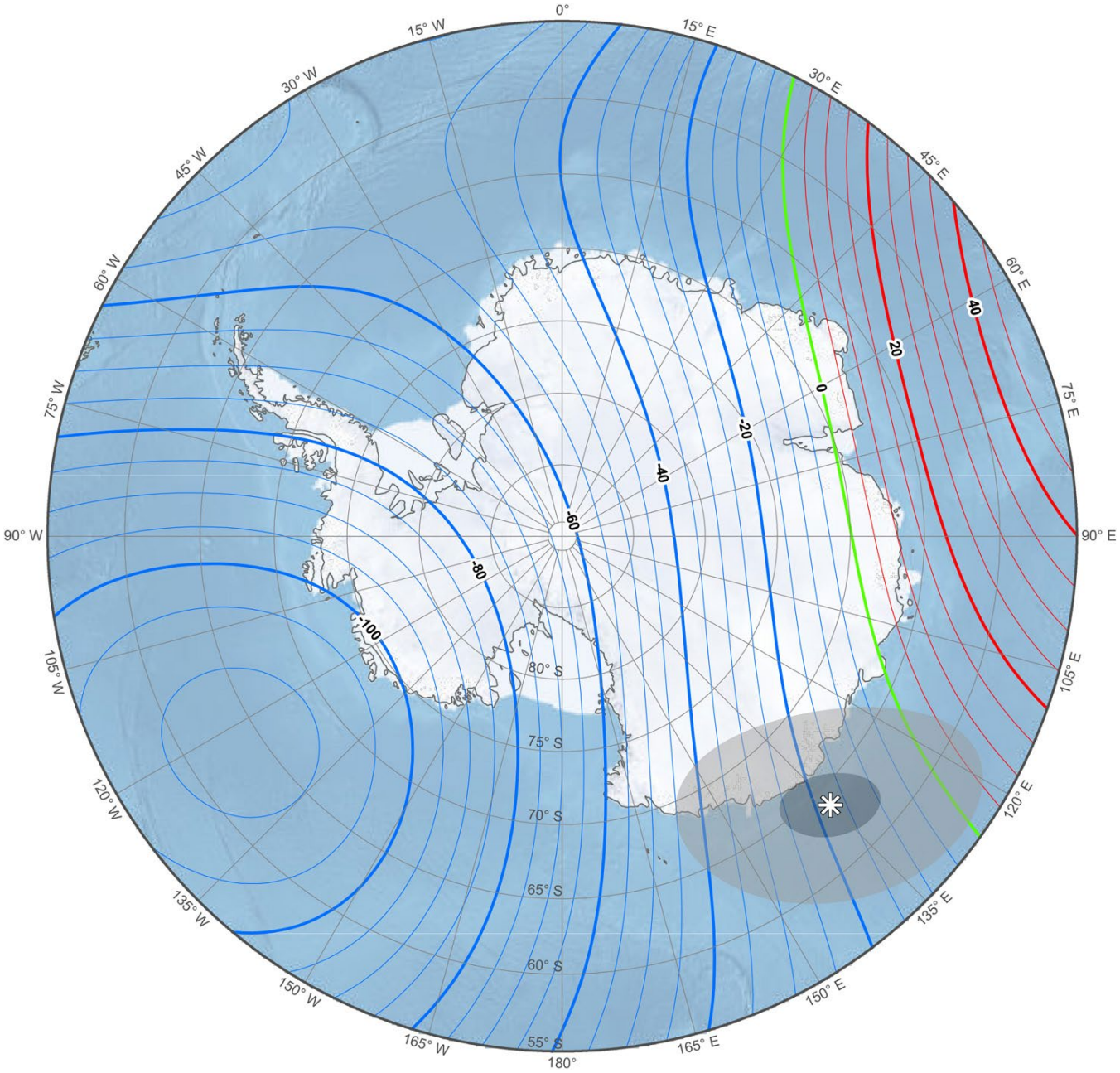

Annual change total intensity (F). The contour interval is 5 nT / year, red contours positive change; blue negative change; green zero change. South Polar Region. Polar stereographic projection.

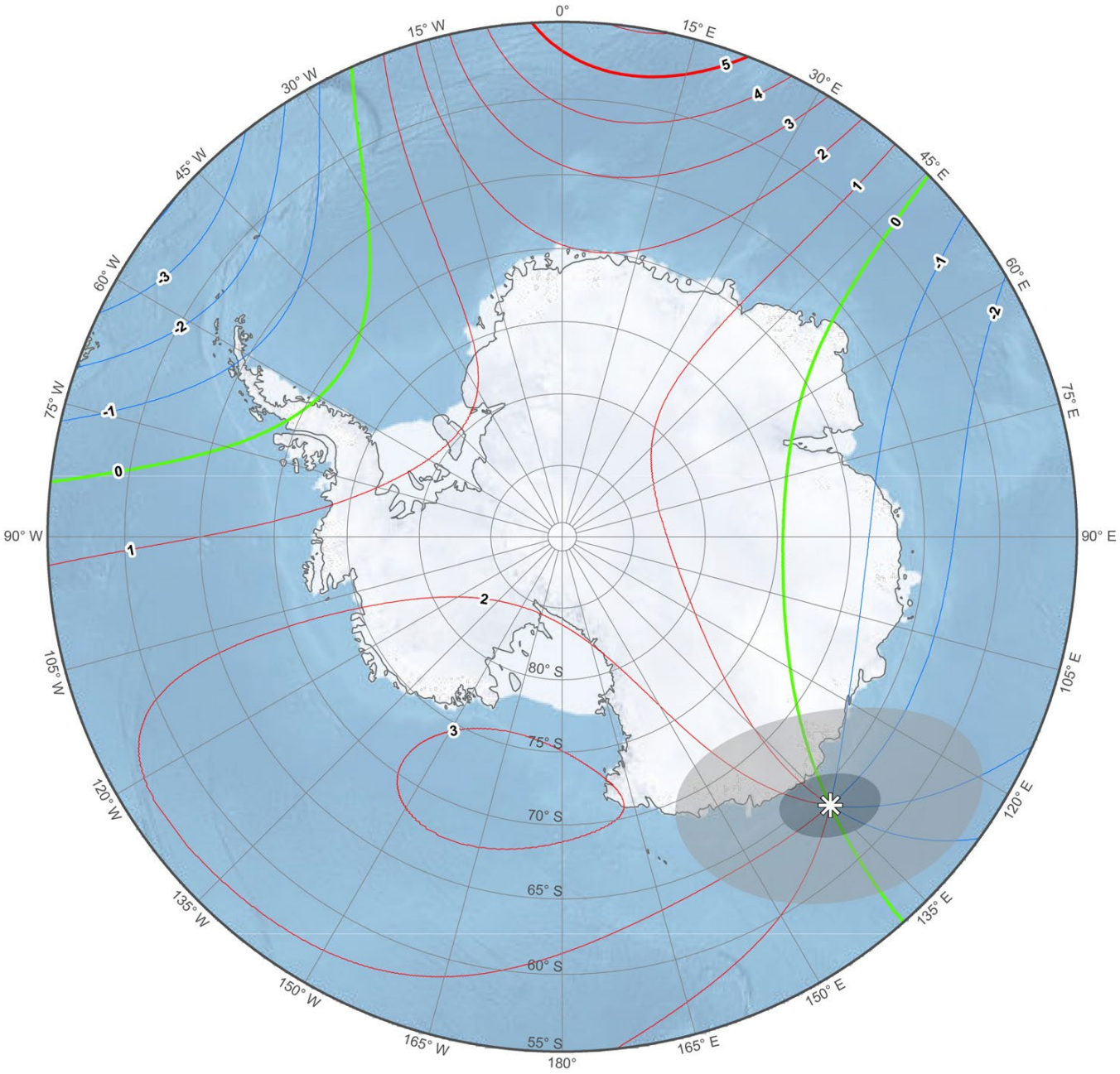

Annual change inclination (I). The contour interval is one arc-minute / year, red contours positive (downward) change; blue negative (upward) change; green zero change. South Polar Region. Polar stereographic projection.

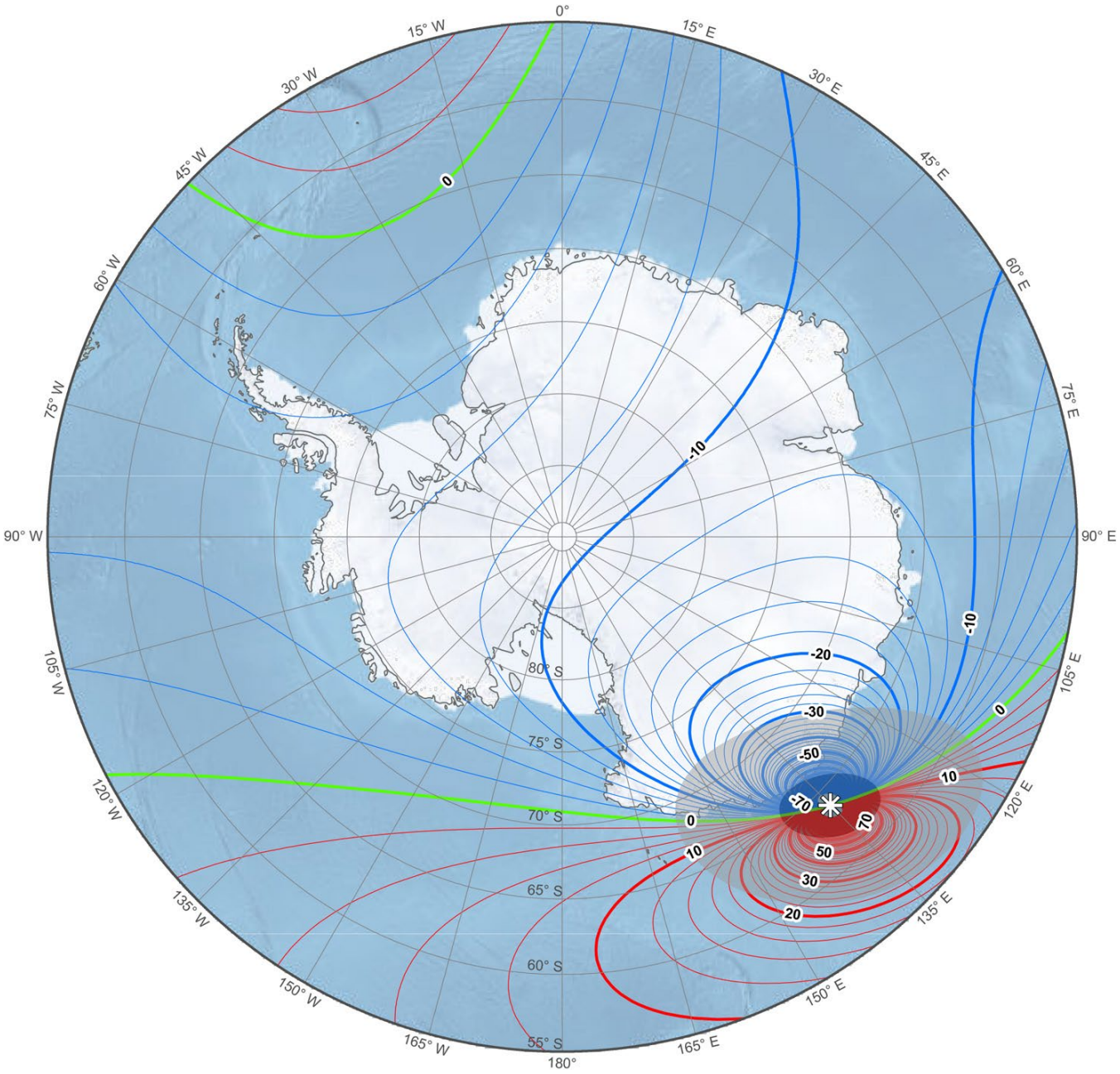

Annual change declination (D). The contour interval is two arc-minutes / year, red contours positive (clockwise) change; blue negative (counter-clockwise) change; green zero change. South Polar Region. Polar stereographic projection.

Grid variation maps: Polar stereographic projection

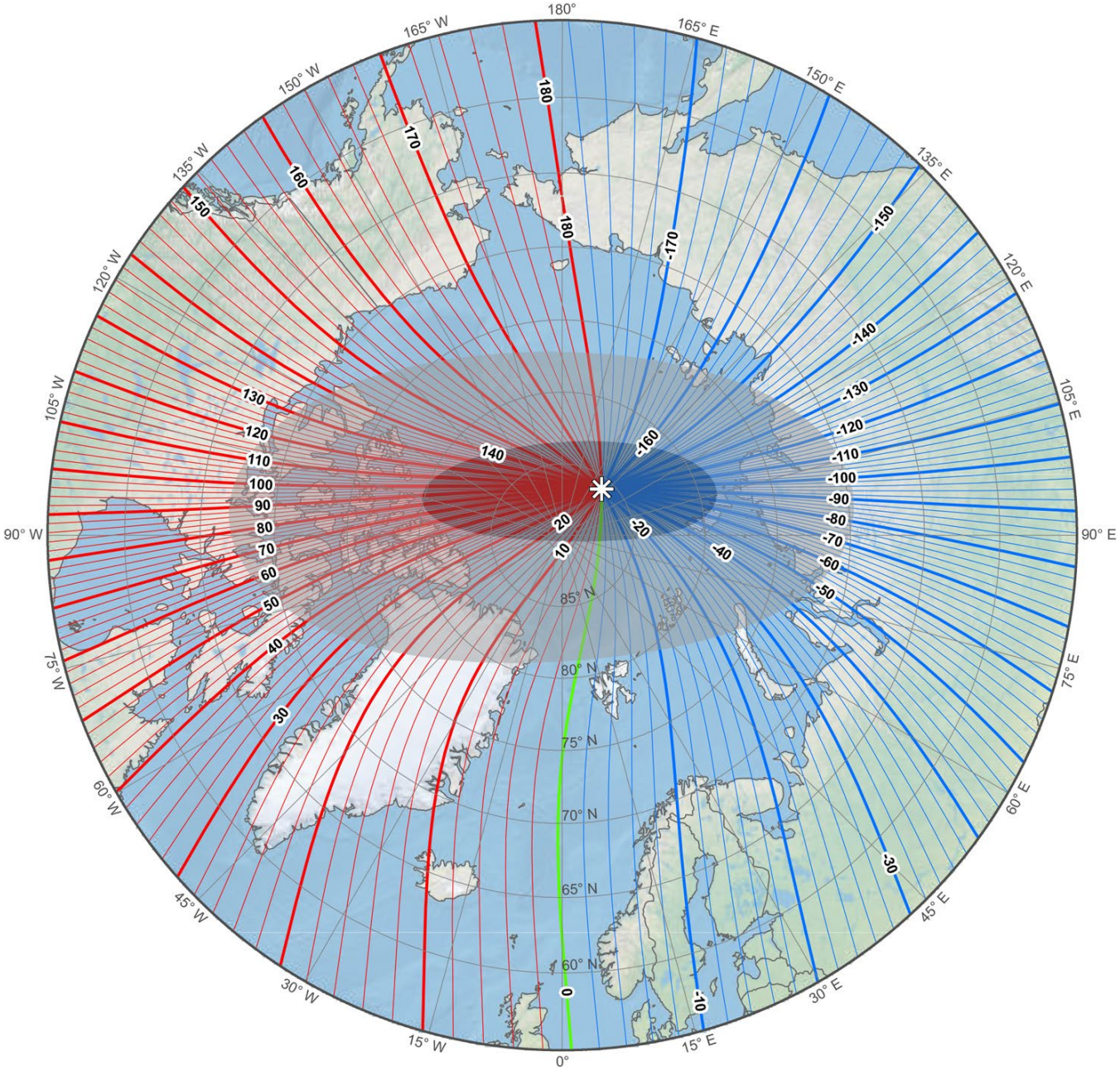

Main field grid variation (GV). The contour interval is two degrees, red contours positive; blue negative; green zero line. North Polar Region. Polar stereographic projection.

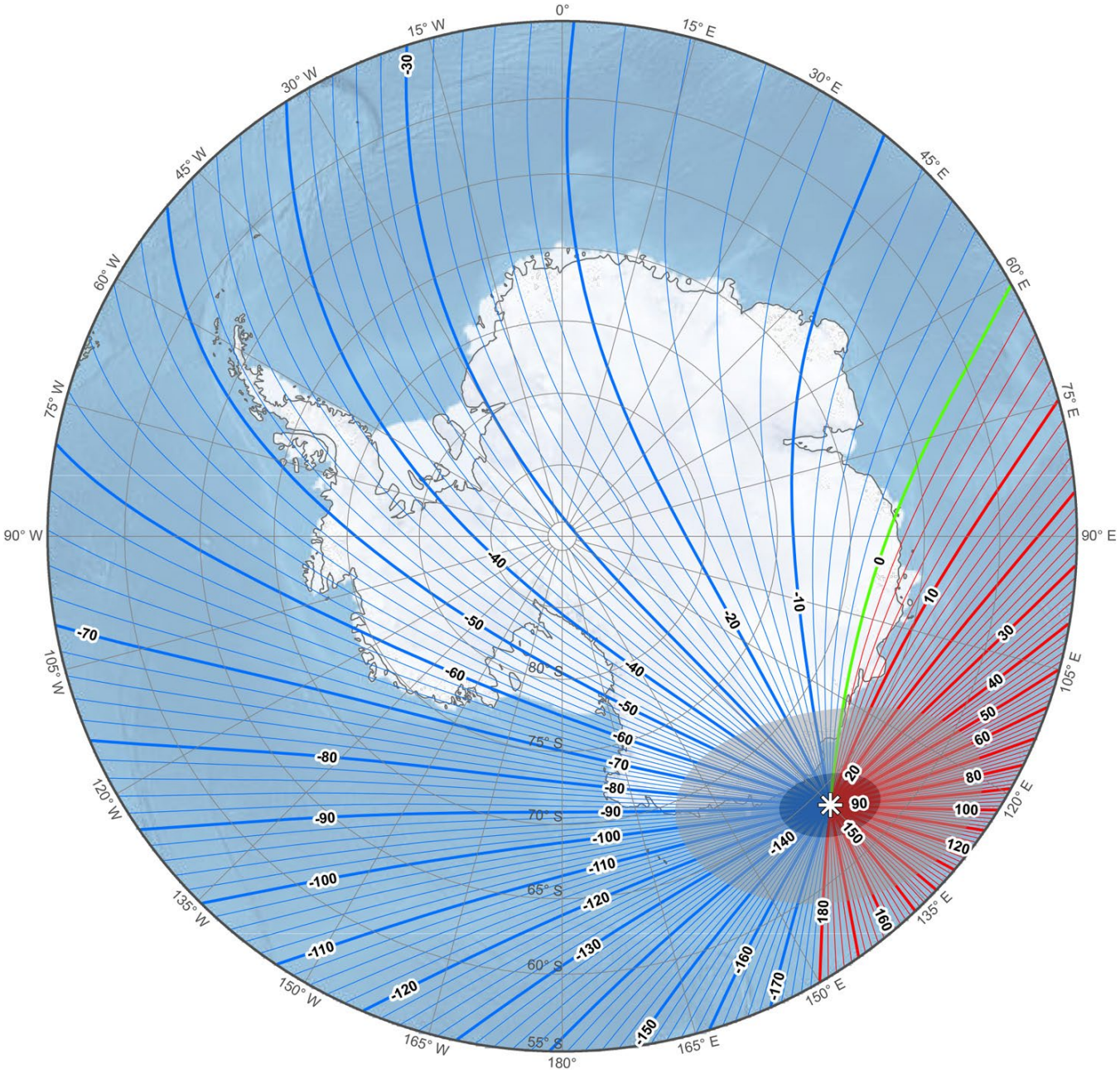

Main field grid variation (GV). The contour interval is two degrees, red contours positive; blue negative; green zero line. South Polar Region. Polar stereographic projection.

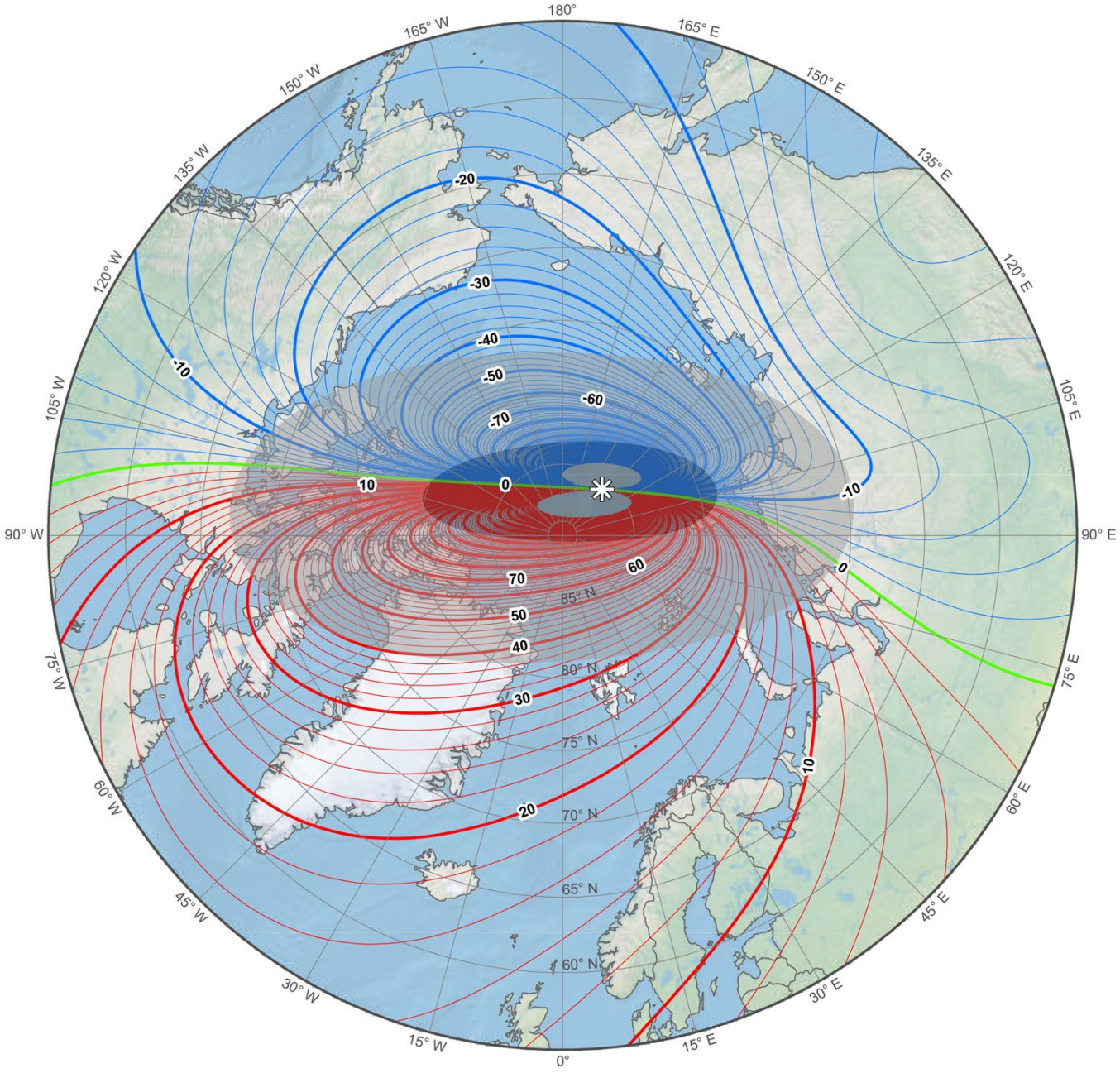

Annual change grid variation (GV). The contour interval is two arc-minutes / year, red contours positive (clockwise); blue negative (counter-clockwise); green zero line. North Polar Region. Polar stereographic projection. (The darkest grey masked contours near the magnetic pole do not represent the blackout or caution zones.)

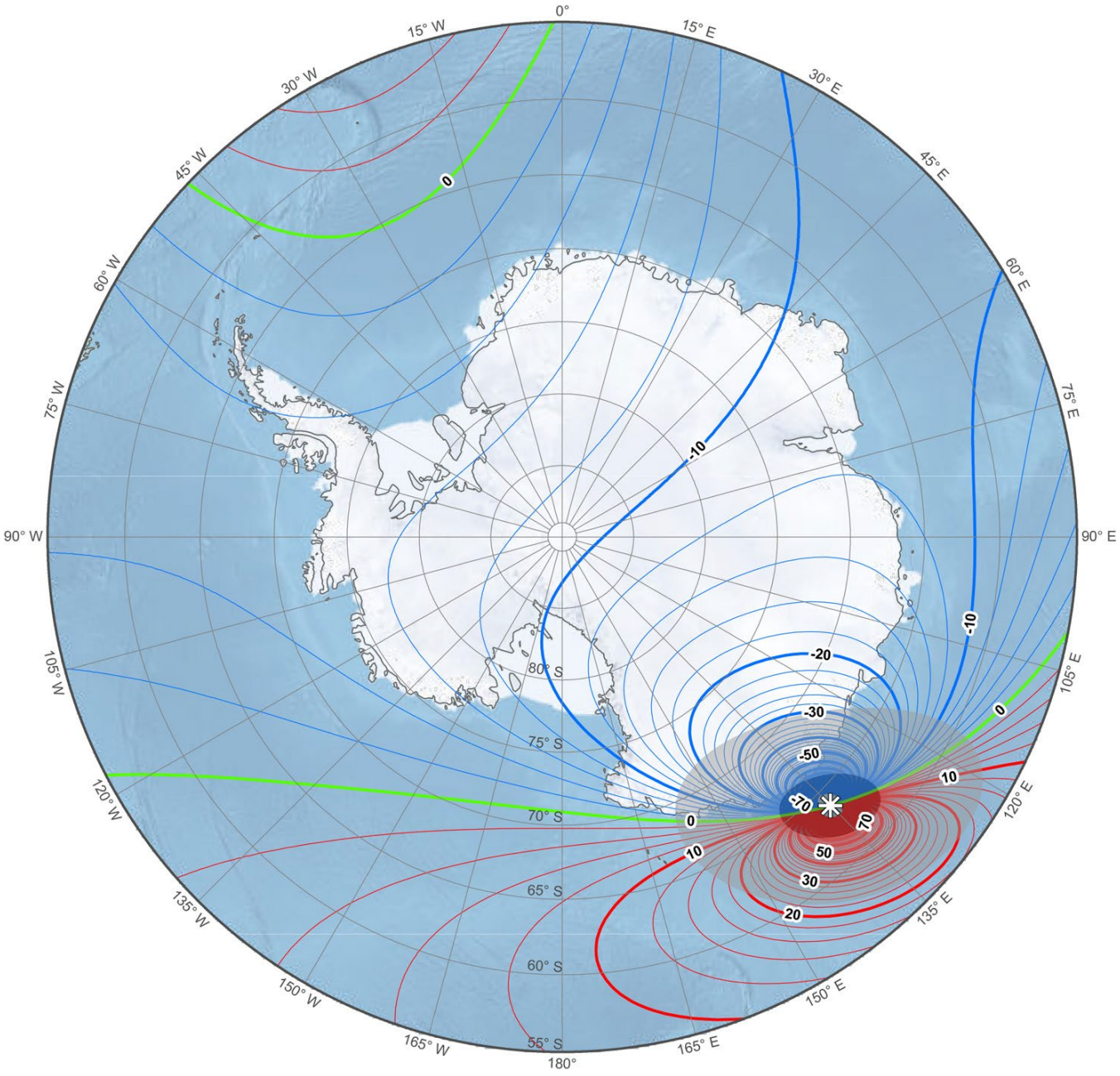

Annual change grid variation (GV). The contour interval is two arc-minutes/year, red contours positive (clockwise); blue negative (counter-clockwise); green zero line. South Polar Region. Polar stereographic projection.

Geomagnetic dipole longitude and latitude. Miller projection.

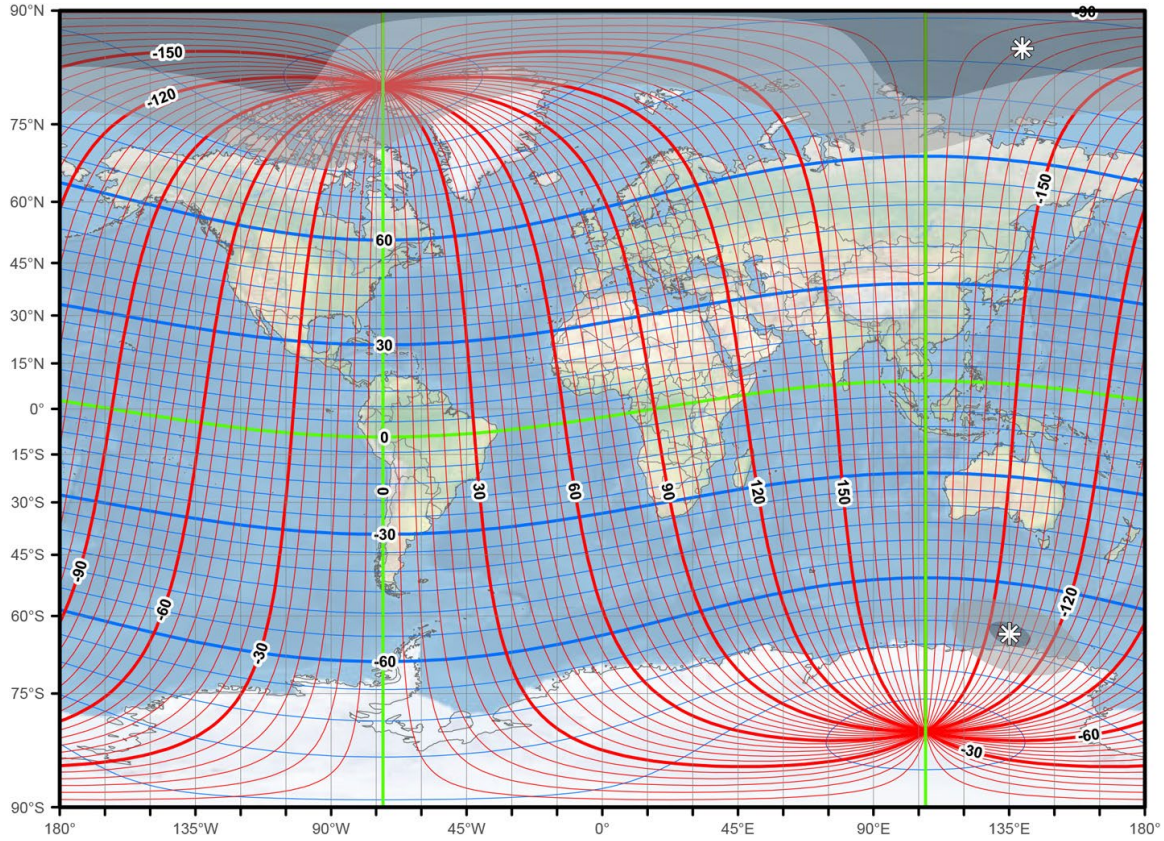

Geomagnetic longitude and latitude. Miller projection.

5. References and Bibliography

Abramowitz, M. and I.A. Stegun, 1972. ***Handbook of Mathematical Functions with Formulas, Graphs, and Mathematical Tables***. Washington, D.C.: U.S. Dept. of Commerce, National Bureau of Standards.

Alken, P., S. Maus, A. Chulliat and C. Manoj, 2015. NOAA/NGDC Candidate Models for the 12th generation International Geomagnetic Reference Field. ***Earth Planets Space,*** 67:68. https://doi.org/10.1186/s40623-015-0215-1

Alken, P., E. Thébault, C.D. Beggan et al., 2021. International Geomagnetic Reference Field: the thirteenth generation. ***Earth Planets Space*** 73, 49. https://doi.org/10.1186/s40623-020-01288-x

Aubert, J. and C.C. Finlay, 2019. Geomagnetic jerks and rapid hydromagnetic waves focusing at Earth's core surface. ***Nat. Geosci***., 12, 393-398. https://doi.org/10.1038/s41561-019-0355-1

Backus, G., R.L. Parker and C. Constable, 1996. ***Foundations of Geomagnetism***. Cambridge (U.K.): Cambridge University Press.

Bai, C., G. Gao, L. Wen and G. Kang, 2024. Dynamic evolution of amplitude and position of geomagnetic secular acceleration pulses since 2000. ***Front. Earth Sci.,*** 12:1383149. https://doi.org/10.3389/feart.2024.1383149

Bartels, J., 1949. The standardized index, Ks, and the planetary index, Kp. ***IATME Bull***., 12b, 97-120.

Brauer, P., J.M.G. Merayo, O.V. Nielsen, F. Primdahl, J.R. Petersen, 1997. Transverse field effect in fluxgate sensors. ***Sensors and Actuators A***, 59, 70-74. https://doi.org/10.1016/S0924-4247(97)01416-7

Brown, W.J., J.E. Mound and P.W. Livermore, 2013. Jerks abound: An analysis of geomagnetic observatory data from 1957 to 2008. ***Phys. Earth Planet. Inter***., 22, 62-76. https://doi.org/10.1016/j.pepi.2013.06.001

Chulliat, A. and S. Maus, 2014. Geomagnetic secular acceleration, jerks, and a localized standing wave at the core surface from 2000 to 2010. ***J. Geophys. Res.***, 119, 1531-1543. https://doi.org/10.1002/2013JB010604

Chulliat, A., S. Macmillan, P. Alken, C. Beggan, M. Nair, B. Hamilton, A. Woods, V. Ridley, S. Maus and A. Thomson, 2015. ***The U.S./U.K. World Magnetic Model for 2015-2020: Technical Report***. National Geophysical Data Center, NOAA. https://doi.org/10.7289/V5TB14V7

Chulliat, A., J. Matzka, A. Masson and S.E. Milan, 2017. Key Ground-Based and Space-Based Assets to Disentangle Magnetic Field Sources in the Earth's Environment. ***Space Sci. Rev.***, 206, 123-156. https://doi.org/10.1007/s11214-016-0291-y

Chulliat, A., W. Brown, P. Alken, S. Macmillan, M. Nair, C. Beggan, A. Woods, B. Hamilton, B. Meyer and R. Redmon, 2019. ***Out-of-Cycle Update of the U.S./U.K. World Magnetic Model for 2015-2020: Technical Note***. National Centers for Environmental Information, NOAA. https://doi.org/10.25921/xhr3-0t19

Chulliat, A., W. Brown, P. Alken, C. Beggan, M. Nair, G. Cox, A. Woods, S. Macmillan, B. Meyer and M. Paniccia, 2020. ***The U.S./U.K. World Magnetic Model for 2020-2025: Technical Report***. National Centers for Environmental Information, NOAA. https://dx.doi.org/10.25923/ytk1-yx35

Chulliat, A., W. Brown, P. Alken, S. Macmillan and M. Paniccia, 2021. Modeling Earth's ever-shifting magnetism. ***Eos***, 102. Published on 14 January 2021. https://doi.org/10.1029/2021EO153457

Chulliat, A., W. Brown, P. Alken, S. Macmillan, M. Nair and B. Meyer, 2021. ***State of the geomagnetic field 2021***. National Centers for Environmental Information (U.S.); British Geological Survey. https://doi.org/10.25923/yetz-e011

Clarke, E., O. Baillie, S.J. Reay and C.W. Turbitt, 2013. A method for the near real-time production of quasi-definitive magnetic observatory data. ***Earth Planets Space,*** 65, 1363-1374. http://doi.org/10.5047/eps.2013.10.001

Defense Mapping Agency, 1981. ***Product Specifications for Global Navigation and Planning Charts***. Document PS/IAD/200.

Department of Defense, 2015. ***Performance Specification – World Magnetic Model (WMM).*** Document MIL-PRF-89500A. Retrieved from https://assist.dla.mil/

Department of Defense, 2019. ***Performance Specification – World Magnetic Model (WMM).*** Document MIL-PRF-89500B. Retrieved from https://assist.dla.mil/

Finlay, C.C., N. Olsen, S. Kotsiaros, N. Gillet and L. Tøffner-Clausen, 2016. Recent geomagnetic secular variation from Swarm and ground observatories as estimated in the CHAOS-6 geomagnetic field model. ***Earth Planets Space***, 68, 112. https://doi.org/10.1186/s40623-016-0486-1

Finlay, C.C., C. Kloss, N. Olsen, M. Hammer, L. Toeffner-Clausen, A. Grayver and A. Kuvshinov, 2020. The CHAOS-7 geomagnetic field model and observed changes in the South Atlantic Anomaly. ***Earth Planets and Space***, 72, 156. https://doi.org/10.1186/s40623-020-01252-9

Friis-Christensen, E., H. Lühr and G. Hulot, 2006. Swarm: A constellation to study the Earth's magnetic field. ***Earth Planets Space***, 58, 351-358. https://doi.org/10.1186/BF03351933

Gillet, N., F. Gerick, D. Jault, T. Schwaiger, J. Aubert and M. Istas, 2022. Satellite magnetic data reveal interannual waves in Earth's core. ***Proc. Natl. Acad. Sci. U.S.A.***, 119(13), e2115258119. https://doi.org/10.1073/pnas.2115258119

Gradshteyn, I.S. and I.M. Ryzhik, 1994. ***Table of Integrals, Series and Products*** (5th ed.). San Diego: Academic Press.

Gubbins, D., 1983. Geomagnetic field analysis - I. Stochastic inversion. ***Geophys. J. Int.***, 73(3), 641-652. https://doi.org/10.1111/j.1365-246X.1983.tb03336.x

Hammer, M.D., G.A. Cox, W.J. Brown, C.D. Beggan, C.C. Finlay, 2021**.** Geomagnetic Virtual Observatories: monitoring geomagnetic secular variation with the Swarm satellites. ***Earth Planets Space***, 73, 54. https://doi.org/10.1186/s40623-021-01357-9

Heiskanen, W. and H. Moritz, 1967. ***Physical Geodesy***. San Francisco: W.H. Freeman and Company.

Huber, P.J., 1996. ***Robust Statistical Procedures***. Philadelphia: Society for Industrial and Applied Mathematics.

Jankowski, J. and C. Sucksdorff, 1996. ***Guide for Magnetic Measurements and Observatory Practice.*** Boulder: International Association of Geomagnetism and Aeronomy. Retrieved from http://www.iaga-aiga.org/data/uploads/pdf/guides/iaga-guide-observatories.pdf

Kan, J.R. and L.C. Lee, 1979. Energy coupling function and solar wind magnetosphere dynamo. ***Geophys. Res. Lett.***, 6, 577–580. https://doi.org/10.1029/GL006i007p00577

Langel, R.A., 1987. The main field. In ***Geomagnetism***, edited by J.A. Jacobs, Academic Press, 249-512.

Laundal, K.M. and A.D. Richmond, 2017. Magnetic Coordinate Systems. ***Space Sci. Rev***., 206:27–59. https://doi.org/10.1007/s11214-016-0275-y

Lemoine, F.G., S.C. Kenyon, J.K. Factor, R.G. Trimmer, N.K. Pavlis, D.S. Chinn, C.M. Cox, S.M. Klosko, S.B. Luthcke, M.H. Torrence, Y.M. Wang, R.G. Williamson, E.C. Pavlis, R.H. Rapp and T.R. Olson, 1998. ***The development of the joint NASA GSFC and NIMA Geopotential Model EGM96***. Technical Report NASA/TP-1998-206861, NASA Goddard Space Flight Center, Greenbelt, Maryland.

Lesur, V., M. Hamoudi, Y. Choi, J. Dyment and E. Thebault, 2016. Building the second version of the World Digital Magnetic Anomaly Map (WDMAM). ***Earth Planets Space***, 68, 27. https://doi.org/10.1186/s40623-016-0404-6

Lühr, H. and S. Maus, 2010. Solar cycle dependence of quiet-time magnetospheric currents and a model of their near-Earth magnetic fields. ***Earth Planets Space***, 62, 843-848. https://doi.org/10.5047/eps.2010.07.012

Macmillan, S., 2007. Observatories, Overview. In ***Encyclopedia of Geomagnetism and Paleomagnetism,*** edited by D. Gubbins and E. Herrero-Bervera, Springer, 708-711.

Macmillan, S. and N. Olsen, 2013. Observatory data and the Swarm mission. ***Earth Planets Space,*** 65, 1355-1362. https://doi.org/10.5047/eps.2013.07.011

Matzka, J., C. Stolle, Y. Yamazaki, O. Bronkalla and A. Morschhauser, 2021. The geomagnetic Kp index and derived indices of geomagnetic activity. ***Space Weather***, 19, e2020SW002641. https://doi.org/10.1029/2020SW002641

Maus, S. and P. Weidelt, 2004. Separating magnetospheric disturbance magnetic field into external and transient internal contributions using 1D conductivity model of the Earth. ***Geophys. Res. Lett.,*** 31, L12614. https://doi.org/10.1029/2004GL020232

Maus, S. and H. Lühr, 2005. Signature of the quiet-time magnetospheric magnetic field and its electromagnetic induction in the rotating Earth. ***Geophys. J. Int.,***162, 755-763. https://doi.org/10.1111/j.1365-246X.2005.02691.x

Maus, S., F. Yin, H. Lühr, C. Manoj, M. Rother, J. Rauberg, I. Michaelis, C. Stolle and R. D. Müller, 2008. Resolution of direction of oceanic magnetic lineations by the sixth-generation lithospheric magnetic field model from CHAMP satellite magnetic measurements. ***Geochem. Geophys. Geosyst***., 9, Q07021. https://doi.org/doi:10.1029/2008GC001949

Maus, S. et al., 2009. EMAG2: A 2–arc min resolution Earth Magnetic Anomaly Grid compiled from satellite, airborne, and marine magnetic measurements. ***Geochem. Geophys. Geosyst.***, 10, Q08005. https://doi.org/10.1029/2009GC002471

Meyer, B., A. Chulliat and R.W. Saltus, 2017. Derivation and Error Analysis of the Earth Magnetic Anomaly Grid at 2 Arc-Minute Resolution Version 3 (EMAG2v3), ***Geochem. Geophys. Geosys.***, 18, 4522-4537. https://doi.org/10.1002/2017GC007280

Merrill, R.T., M.W. McElhinny and P.L. McFadden, 1996. ***The Magnetic Field of the Earth: Paleomagnetism, the Core and the Deep Mantle***. San Diego: Academic Press.

Nair, M., A. Chulliat, A. Woods, P. Alken, B. Meyer, B. Poedjono, N. Zachman and J. Hernandez, 2021. Next Generation High-Definition Geomagnetic Model for Wellbore Positioning, Incorporating New Crustal Magnetic Data. Paper presented at the Offshore Technology Conference, Virtual and Houston, Texas, August 2021. https://doi.org/10.4043/31044-MS

National Centers for Environmental Information (U.S.) and British Geological Survey, 2022. ***State of the Geomagnetic Field 2022***. https://doi.org/10.25923/8r5d-fj70

National Centers for Environmental Information (U.S.) and British Geological Survey, 2023. ***State of the Geomagnetic Field 2023.*** https://doi.org/10.25923/cww1-sc35

NATO Standardization Agency, 2011. ***STANAG 7172 Use of Geomagnetic Models*** (2nd ed).

Newell, P.T., T. Sotirelis, K. Liou, C.-I. Meng and F.J. Rich, 2007. A nearly universal solar wind-magnetosphere coupling function inferred from 10 magnetospheric state variables, ***J. Geophys. Res***., 112(A1). https://dx.doi.org/10.1029/2006JA012015

Newitt, L., A. Chulliat and J.-J. Orgeval, 2009. Location of the North Magnetic Pole in April 2007. ***Earth Planets Space,*** 61, 703-710. https://doi.org/10.1186/BF03353178

Olsen, N., L. Tøffner-Clausen, T.J. Sabaka, P. Brauer, J.M.G. Merayo, J.L. Jörgensen, J.-M. Léger, O.V. Nielsen, F. Primdahl and T. Risbo, 2003. Calibration of the Ørsted vector magnetometer. ***Earth Planets and Space***, 55, 11-18. https://doi.org/10.1186/BF03352458

Olsen, N., H. Lühr, C.C. Finlay, T.J. Sabaka, I. Michaelis, J. Rauberg and L. Tøffner-Clausen, 2014. The CHAOS-4 geomagnetic field model. ***Geophys. J. Int***., 197, 815-827. https://doi.org/10.1093/gji/ggu033

Parkinson, W.D., 1983. ***Introduction to Geomagnetism.*** Edinburgh: Scottish Academic Press.

Pavón-Carrasco, F. J., S. Marsal, S.A. Campuzano, and J.M. Torta, 2021. Signs of a new geomagnetic jerk between 2019 and 2020 from Swarm and observatory data. ***Earth Planets Space*** 73, 175, https://doi.org/10.1186/s40623-021-01504-2

Peltier, A. and A. Chulliat, 2010. On the feasibility of promptly producing quasi-definitive magnetic observatory data. ***Earth Planets Space***, 62, e5-e8. https://doi.org/10.5047/eps.2010.02.002

Rother, M., M. Korte, A. Morschhauser, F. Vervelidou, J. Matzka and C. Stolle, 2021**.** The Mag.num core field model as a parent for IGRF-13, and the recent evolution of the South Atlantic Anomaly. ***Earth Planets Space*** 73, 50. https://doi.org/10.1186/s40623-020-01277-0

Sugiura, M., 1964. Hourly values of the equatorial Dst for the IGY. ***Ann. Int. Geophys. Yr.***, 35, 9-45.

Thomson, A.W.P. and V. Lesur, 2007. An improved geomagnetic data selection algorithm for global geomagnetic field modelling. ***Geophys. J. Int.,*** 169, 951-963. https://doi.org/10.1111/j.1365-246X.2007.03354.x

Thomson, A.W.P., B. Hamilton, S. Macmillan and S.J. Reay, 2010. A novel weighting method for satellite magnetic data and a new global magnetic field model. ***Geophys. J. Int***., 181, 250-260. https://doi.org/10.1111/j.1365-246X.2010.04510.x

Tøffner-Clausen, L., V. Lesur, N. Olsen and C. C. Finlay, 2016. In-flight scalar calibration and characterisation of the Swarm magnetometry package. ***Earth Planets Space***, 68:129. https://doi.org/10.1186/s40623-016-0501-6